

THE ROLE OF THE ATMOSPHERE ON NORTHERN HEMISPHERE
ICE SHEET EVOLUTION DURING THE LATE PLEISTOCENE

LU NIU



DISSERTATION
zur Erlangung des akademischen Grades einer
Doktorin der Naturwissenschaften
– Dr. rer. nat. –

Fachbereich für Physik und Elektrotechnik,
Universität Bremen 
Alfred-Wegener-Institut 

September 2019, Bremerhaven

– BETREUER & GUTACHTER 1 –

Prof. Dr. Gerrit Lohmann

– GUTACHTER 2 –

Prof. Dr. Michael Schulz

Lu Niu: *The role of the atmosphere on Northern Hemisphere ice sheet evolution during the late Pleistocene*, Dissertation zur Erlangung des akademischen Grades einer Doktorin der Naturwissenschaften (Dr. rer. nat.), © September 2019

Was mich nicht umbringt, macht mich stärker.

— Friedrich Nietzsche

Dedicated to all the people that I love.

ERKLÄRUNG

Hiermit versichere ich, dass ich

1. die Arbeit ohne fremde Hilfe angefertigt habe,
2. keine anderen als die von mir angegebenen Quellen und Hilfsmittel benutzt habe und
3. die den benutzten Werken wörtlich oder inhaltlich entnommenen Stellen als solche kenntlich gemacht habe.

Bremerhaven, September 2019

Lu Niu

ABSTRACT

During the late Pleistocene, the Northern Hemisphere ice sheets waxed and waned with a periodicity of around 100 kyr. They are among the largest topographic features that can amplify, pace or drive global climate change on different time scales. Studying ice sheet-climate feedback through numerical modelling is necessary for understanding the physical mechanisms of the Earth system. As mainly land-based ice sheets, the role of the atmosphere on Northern Hemisphere ice sheet evolution during the late Pleistocene is investigated.

The evolution of Northern Hemisphere ice sheets through the last glacial cycle is simulated with the glacial index method by using the climate forcing from a general circulation model, COSMOS. By comparing the simulated results to geological reconstructions, we first show that the modelled climate is capable of capturing the main features of the ice-sheet evolution. However, large deviations exist, likely due to the absence of nonlinear interactions between ice sheet and other climate components.

The model uncertainties of the climate forcing are examined using the output from nine climate models from the Paleoclimate Modelling Intercomparison Project Phase III. The results show a large variability in simulated ice sheets between the different models. We find that the ice sheet extent pattern resembles summer surface air temperature pattern at the Last Glacial Maximum, confirming the dominant role of surface ablation process for high-latitude Northern Hemisphere ice sheets. This study shows the importance of the upper boundary condition for ice sheet modelling, and implies that careful constraints on climate output is essential for simulating realistic glacial Northern Hemisphere ice sheets.

Evidence from proxy records indicates that millennial-scale abrupt climate shifts, called Dansgaard-Oeschger events, happened during past glacial cycles. We show that the Dansgaard-Oeschger events can regulate the mean state of the Northern Hemisphere ice sheets. Sensitivity experiments show that the simulated mean state is influenced by the amplitude of the climatic noise. The most likely cause of this phenomenon is the nonlinear response of the surface mass balance to temperature. It could also cause the retreat processes to be faster than the buildup processes within a glacial cycle. We propose that the climate variability hindered ice sheet development and prevented the Earth system from entering a full glacial state from Marine Isotope Stage 4 to Marine Isotope Stage 3 about 60,000 years ago.

Antarctic ice core and deep ocean sediment core records imply that the interglacial climate during Marine Isotope Stage 13 is relatively

cold, and ice sheets were likely larger. From perspective of equilibrium simulations, we modelled the MIS 13 climate with a coupled climate-ice sheet model AWI-CM-PISM under different orbital configurations at 495, 506 and 517 kyr BP. Summer insolation at 65 °N at 495 kyr BP is similar to the preindustrial, but with lower greenhouse gas values. It leads to more ice sheet buildup than present-day. Boreal summer at perihelion at 506 kyr BP causes a warmer summer over Northern Hemisphere continents. This could inhibit the development of Northern Hemisphere ice sheets. Lower obliquity induces cooling over the polar regions and is favorable for the ice sheet buildup. Besides polar regions, mountains with high elevations are also favorable for ice sheet buildup. The Cordilleran Ice Sheet is likely more sensitive and has faster response to boreal summer insolation change than the other large scale Northern Hemisphere ice sheets.

PUBLICATIONS

- Gowan, E. J., L. Niu, G. Knorr, and G. Lohmann (2019). "Geology datasets in North America, Greenland and surrounding areas for use with ice sheet models." In: *Earth System Science Data* 11.1, pp. 375–391. DOI: [10.5194/essd-11-375-2019](https://doi.org/10.5194/essd-11-375-2019).
- Niu, L., G. Lohmann, and E. J. Gowan (2019a). "Climate Noise Influences Ice Sheet Mean State." In: *Geophysical Research Letters* 46. DOI: [10.1029/2019GL083717](https://doi.org/10.1029/2019GL083717).
- Niu, L., G. Lohmann, S. Hinck, E. J. Gowan, and U. Krebs-Kanzow (2019b). "The sensitivity of Northern Hemisphere ice sheets to atmospheric forcing during the last glacial cycle using PMIP3 models." In: *Journal of Glaciology* 65.252, pp. 645–661. DOI: [10.1017/jog.2019.42](https://doi.org/10.1017/jog.2019.42).
- Niu, L., P. Gierz, E. J. Gowan, and G. Lohmann (in prep). "Instability of the Cordilleran Ice Sheet under different orbital forcing." In: *To be submitted*.

*Man tries to make for himself in the fashion that suits him best
a simplified and intelligible picture of the world;
he then tries to some extent to substitute this cosmos of his
for the world of experience, and thus to overcome it.
This is what the painter, the poet, the speculative philosopher,
and the natural scientist do, each in his own fashion.*

— **Albert Einstein**, *Principles of Research* (1918)

ACKNOWLEDGMENTS

The thesis was written at Alfred Wegener Institute, Helmholtz Center for Polar and Marine Research in Bremerhaven, where I got considerable support for finishing my Ph.D study.

Firstly, I would like to express my sincere gratitude to my advisor Prof. Dr. Gerrit Lohmann for the tremendous academic support of my Ph.D study and related research. He has a very pleasant personality and is full of enthusiasm on science, which inspires me a lot. I could not have imagined having a better advisor and mentor for my Ph.D study.

I would also like to thank Dr. Evan J. Gowan, Dr. Lennert Stap, Sebastian Hinck and other colleagues at AWI for the helpful discussions, in terms of ice sheet modelling, ice sheet reconstruction, ice-climate interactions, as well as scientific English writing. An additional thanks goes to all the former and current members of Paleoclimate Dynamics group, for creating such an open and harmonious working environment which I enjoyed very much.

I thank the graduate school POLMAR at AWI for the useful courses of climate research, and also China Scholar Council (CSC) for the financial support during my Ph.D study.

Importantly, great thanks to my parents and all my friends inside or outside Germany. Studying in Germany is such a special experience, and I appreciated their spiritual support and company for all the moments.

CONTENTS

I BACKGROUND

1	GENERAL INTRODUCTION	3
1.1	Motivation	3
1.2	Objectives and Structure of the Thesis	6
2	MODEL DESCRIPTION	9
2.1	The Ice Sheet Model	9
2.1.1	Ice Dynamics	10
2.1.2	The Subglacial Dynamics	10
2.1.3	The Ice Shelf Dynamics	11
2.1.4	The Surface Processes	12
2.2	The Climate	14
2.2.1	The Glacial Index Method	14
2.2.2	The Climate Model COSMOS	15
2.2.3	The Paleoclimate Modelling Intercomparison Project III (PMIP ₃)	15
2.3	The Coupled Climate-Ice Sheet Model	16
2.3.1	The Climate Model AWI-CM	18
2.3.2	The Coupling to Ice Sheet Model PISM	20

II THE SHOWCASE 1

3	NORTHERN HEMISPHERE ICE SHEET EVOLUTION THROUGH THE LAST GLACIAL CYCLE	25
3.1	Introduction	25
3.2	Experiment Design	25
3.3	Results	26
3.3.1	The Temporal Evolution of Ice Sheet Volume	29
3.3.2	Spatial Distribution of Ice Sheets	30
3.4	Discussions	33
3.4.1	The Glacial Index Method	33
3.4.2	PDD and Surface Energy Balance	34
3.4.3	Potential for Further Investigation	36
3.5	Conclusions	36
4	EFFECTS OF MODEL UNCERTAINTY ON NORTHERN HEMISPHERE ICE SHEET EVOLUTION	37
4.1	Introduction	37
4.2	Experiment Design	37
4.3	Results	38
4.4	Discussions: The atmospheric forcing from GCMs	42
4.5	Conclusions	49
5	EFFECTS OF CLIMATE VARIABILITY ON ICE SHEET MEAN STATE	53
5.1	Introduction	53

5.2	Experiment Design	54
5.3	Results	55
5.4	Discussions: The Physical Interpretation	60
5.5	Conclusions	66
III THE SHOWCASE 2		
6	EFFECTS OF ORBITAL CHANGE ON NORTHERN HEMI- SPHERE ICE SHEETS DURING MIS 13	71
6.1	Introduction	71
6.2	Experiment Design	72
6.3	The Reference PI Climate with Interactive Ice Sheets	74
6.4	The MIS 13 Climate without Interactive Ice Sheets	76
6.5	MIS 13 Climate with Interactive Ice Sheets	80
6.5.1	The 495 ka Climate	80
6.5.2	The 506 ka Climate	83
6.5.3	The 517 ka Climate	83
6.6	Discussions	84
6.6.1	The Effect of Precession	84
6.6.2	The Effect of Obliquity	86
6.6.3	The MIS 13 Ice Sheets	86
6.7	Conclusions	88
7	SUMMARY AND OUTLOOK	91
	REFERENCES	93

LIST OF FIGURES

- Figure 1.1 Present-day ice sheets, as well as other components of the Cryosphere. (Figure from NASA/-Goddard Space Flight Center Scientific Visualization Studio) 3
- Figure 1.2 Location of Northern Hemisphere ice sheets at the Last Glacial Maximum (21 kyr BP): Cordillera, Laurentide, Innuitian, Greenland, Barents-Kara, Fennoscandia and British-Irish Ice Sheets (blue line; Dyke, 2004; Gowan et al., 2016; Hughes et al., 2016). The locations of the three domes of Laurentide Ice Sheet: Labrador-Quebec, Keewatin and Foxe. The areas mentioned in this study include the Hudson Bay (HB), the Great Lakes (GL), Baffin Island (BI), Ellesmere Island (EI), Taimyr Peninsula (TP), Laptev Sea (LS), East Siberian Sea (ESS) and Chukchi Sea (CS). The yellow area is the Interior Plains, the pink area is the Canadian Shield and the purple area is the Scandinavia Mountains (SM). 4
- Figure 2.1 PISM's view of interfaces between an ice sheet and the outside world (The PISM authors, 2016) 9
- Figure 2.2 Schematic of coupling between the climate model AWI-CM and ice sheet model PISM. 18
- Figure 2.3 The spatial resolution of FESOM mesh, with higher resolution applied along the coasts and in polar and tropical regions. 19
- Figure 3.1 (a) The NGRIP ice core $\delta^{18}\text{O}$ record (Andersen et al., 2004) and the corresponding value of the glacial index. (b) The reconstructed relative sea level change from Rohling et al. (2014, dark blue line) with 1σ error bars (light blue), Lambeck et al. (2014, black line) and the modelled sea level equivalent (SLE) of the Northern Hemisphere ice sheets (red) using COSMOS-AWI. The correlation coefficient between SLE (PISM) and RSL (Rohling 2014) is 0.865. (c) Separated sea level equivalent (SLE) of Greenland Ice Sheet (green), Eurasian ice sheets (black), North American ice sheets (blue) and Northern Hemisphere ice sheets (red) through the last glacial cycle. 27

- Figure 3.2 Winter (DJF) and summer (JJA) surface air temperature for Last Glacial Maximum (LGM, a-b) from COSMOS-AWI (Zhang et al., 2013) and Present Day (PD, c-d) from NCEP Reanalysis data (Kalnay et al., 1996), and the difference between LGM and PD surface air temperature (LGM minus PD, e-f). 28
- Figure 3.3 Same as Fig. 3.2, but for precipitation. The present day precipitation is from GPCP precipitation products (Adler et al., 2003). 28
- Figure 3.4 Modelled ice thickness (m) evolution through the last glacial cycle at different climate stages. The simulation is forced by the climatology monthly mean surface air temperature and precipitation from COSMOS-AWI. 31
- Figure 3.5 Comparison of surface melt between energy balance-based scheme from COSMOS (a, d, g) and PDD-based scheme from PISM (b, e, h or c, f, i) at the LGM, present day (PD) and Eemian (Units: m/year). The right panel plots are from the reference simulation (COSMOS-AWI) with reanalysis products at PD and COSMOS GCM at the LGM as climate forcing. The middle panel plots are with COSMOS GCM at preindustrial and the LGM. 35
- Figure 4.1 Modelled sea level equivalent (SLE) of Northern Hemisphere ice sheets change through the last glacial cycle using the output of PMIP3 models. (a) Experiment PMIP3-PDobs, with climate forcing of present day conditions from reanalysis products (1981-2010) and the LGM conditions from PMIP3 GCM output. (b) Experiment PMIP3-PIpmip3, with climate forcing of present day conditions from PMIP3 preindustrial (PI) output and LGM conditions from PMIP3 GCM output. 39
- Figure 4.2 Root-mean-square deviations of SLE when compared to the reference simulation (COSMOS-AWI) for different PMIP3 models. Black circles are from experiment PMIP3-PDobs, blue triangles are from experiment PMIP3-fixCOSMOSTemp, red triangles are from experiment PMIP3-fixCOSMOSPrecip. 40
- Figure 4.3 Modelled ice thickness at the Last Glacial Maximum (LGM, 21 kyr BP) using the PMIP3 model output from experiment PMIP3-PDobs. 41

- Figure 4.4 Probability Distribution Functions (PDF) of surface air temperature (upper two rows) and precipitation (lower two rows) over the ice sheet margins (ISM) and Northern Hemisphere (NH) for different seasons (MAM, JJA, SON, DJF) for different models. For the colors, we refer to Fig. 4.1. 42
- Figure 4.5 The surface air temperature at the Last Glacial Maximum (LGM) in summer (JJA) for different models that participated in PMIP3 and the ice sheet margins at the LGM (black lines). 43
- Figure 4.6 Modelled sea level equivalent (SLE) of Northern Hemisphere ice sheets change through the last glacial cycle using the PMIP3 model output. (a) PMIP3-fixCOSMOSTemp, with surface air temperature from COSMOS-AWI, precipitation from PMIP3 models. (b) PMIP3-fixCOSMOSPrecip, with precipitation from COSMOS-AWI, surface air temperature from PMIP3 models. 44
- Figure 4.7 Modelled ice thickness at the Last Glacial Maximum (LGM, 21 kyr BP) from experiment PMIP3-fixCOSMOSTemp. 45
- Figure 4.8 Same as Fig. 4.7, except that experiment from PMIP3-fixCOSMOSPrecip. 46
- Figure 4.9 Surface albedo in summer from different models participating in PMIP3. The albedo is calculated as the ratio of surface upward shortwave radiation and surface downward shortwave radiation. (The shortwave upward radiation for FGOALS-g2 is not available from the PMIP3 data output online.) 47
- Figure 4.10 The Precipitation (Precip) difference between Last Glacial Maximum (LGM) and Present Day (PD) in winter (DJF) for different models that participated in PMIP3 (LGM minus PD). 48
- Figure 4.11 Same as Fig. 4.7, except that experiment from PMIP3-PIpmip3. 50
- Figure 4.12 Simulated ice thickness differences at the LGM between experiments from PMIP3-PDObs and PMIP3-PIpmip3, PIpmip3-PDObs. 51
- Figure 4.13 Summer (JJA) surface air temperature differences at present day between reanalysis products (PDObs) and PMIP3 PI GCM output (PIpmip3), PIpmip3-PDObs. 52

- Figure 5.1 (a) The index used to determine the forcing of the simulated ice sheets. The time series is a Greenland synthetic $\delta^{18}\text{O}$ record derived from an Antarctic temperature record (Barker et al., 2011, black line). From 0 to 5000 year BP, the index is derived from the GISP2 Greenland ice core. The red line is the same record with 5000-year smoothing. (b) The simulated ice sheet sea level equivalent (SLE) and the reconstructed sea level record from Mediterranean (Rohling et al., 2014, blue line). The black line represents the simulation forced by the original $\delta^{18}\text{O}$ record with high variability (GL_hf), while the red line represents the simulation forced by the 5000-year smoothed record with low variability (GL_lf). (c) The scatter distribution between the simulated SLE difference (GL_hf-GL_lf) and the standard deviation from the index series. Different colors and numbers indicate different glacial cycles (1: the last glacial cycle, 2: the penultimate glacial cycle, and so on). (d) The simulated ice sheet thickness at 158000 yr BP, from experiments GL_hf, GL_lf and the difference between them (GL_hf - GL_lf). (NA: North American ice sheets. EA: Eurasian ice sheets. HB: Hudson Bay.) 56
- Figure 5.2 Winter (DJF) and summer (JJA) surface air temperature for the Last Glacial Maximum (LGM, a-b) and preindustrial (PI, c-d) from COSMOS output, and the difference between the LGM and PI (LGM minus PI, e-f). 57
- Figure 5.3 Same as Fig. 5.2, but for precipitation. 57
- Figure 5.4 Coherence test between the glacial index forcing and the simulated sea level equivalent in Fig. 5.1a-b for experiment GL_hf and GL_lf. 58
- Figure 5.5 (a-h) The forcing index based on a cosine time series combined with different amplitude of white noise from year 0 to 120,000. (a) 0.05σ standard deviation. (b) 0.1σ . (c) 0.15σ . (d) 0.2σ . (e) 0.25σ . (f) 0.3σ . (g) 0.35σ . (h) 0.4σ . (i) The corresponding simulated ice sheet sea level equivalent (SLE) from year 0 to 120,000. Note that the y-axes are reversed. 59

- Figure 5.6 (a) The relation between the annual mean surface air temperature (T , °C) and the calculated surface mass balance (SMB, m w.e./year). The reddish (solid) lines represent varying degree-day factor (f_{PDD} , 0.003 - 0.009 m/(°C day)), the bluish (dashed) lines represent varying precipitation (P , 0.0 - 0.003 m/day). (b) The surface air temperature (T) over one year, from Eq. 5.1. White noise with a standard deviation of 3 °C is added on to the curve to account for the synoptic variations. The red line is with an annual mean temperature of -10 °C. The pink lines are shifted by ± 10 °C from the red line. (c) The relation between the annual mean temperature anomalies $|\Delta T|$ and the change of the resultant surface mass balance $|\Delta \text{SMB}|$, based on the intersection of dashed lines in (a). The red line is with the warm anomaly, the blue line is with the cold anomaly, the black is the difference between the red line and the blue line. 62
- Figure 5.7 (a) The Greenland synthetic $\delta^{18}\text{O}$ time series. Same as Fig. 5.1, but from 250,000 to 0 yr BP. The red line is the time series with 5000-year smoothing. (b) The simulated mean surface mass balance (SMB) over the ice sheet domain from experiment GL_hf (black) and GL_lf (red). (c-d) The scatter plot between the simulated SMB and $\delta^{18}\text{O}$ during 120,000 - 20,000 yr BP (c) and 240,000 - 140,000 yr BP (d). (e) Scatter plot between $|\Delta \delta^{18}\text{O}|$ and the resultant $|\Delta \text{SMB}|$. The differences, Δ , for $\delta^{18}\text{O}$ and SMB are between experiment GL_hf and GL_lf (GL_hf - GL_lf). 64
- Figure 6.1 The δD Dome C record (EPICA Community Members, 2006; Jouzel et al., 2007) and the LR04 benthic $\delta^{18}\text{O}$ stack (Lisiecki and Raymo, 2005). The figure is from Jouzel et al. (2007). 72

- Figure 6.2 The boreal summer insolation at 65 °N (red). The orbital parameters from Berger (1978): Obliquity (yellow), Eccentricity (brown) and Precession parameter (green, from spring equinox, $\text{param} = e \sin(\bar{\omega} + \pi)$). Benthic $\delta^{18}\text{O}$ from Lisiecki and Raymo (2005, black). δD from Antarctic Dome C (Jouzel et al., 2007, blue). CO_2 record from Hönlisch et al. (2009, purple). The dots indicate the respective values for preindustrial (PI). 73
- Figure 6.3 The simulated annual mean (Annual), summer (JJA), winter (DJF) surface air temperature (SAT) pattern for experiment Plo-ka, and the difference between Plo-ka and PInoIce. The hatched area did not pass the 0.05 significant level. 75
- Figure 6.4 The simulated sea ice concentration for experiment Plo-ka in September and March, and the difference between Plo-ka and PInoIce. The hatched area did not pass the 0.05 significant level. 76
- Figure 6.5 The simulated ice thickness for experiment Plo-ka and PInoIce. 77
- Figure 6.6 The insolation at PI and the difference between 506 kyr BP and PI. 78
- Figure 6.7 Similar as Fig. 6.3, but for experiment 506noIce, and the difference between 506noIce and PInoIce. 78
- Figure 6.8 The simulated annual mean (Annual), summer (JJA), winter (DJF) precipitation (Precip) pattern for experiment 506noIce, and the difference between 506noIce and PInoIce. The hatched area did not pass the 0.05 significant level. 79
- Figure 6.9 Similar as Fig. 6.4, but for experiment 506noIce, and the difference between 506noIce and PInoIce. 80
- Figure 6.10 Similar as Fig. 6.3 for surface air temperature (SAT), but for experiment 495-ka, and the difference between 495-ka and Plo-ka. 81
- Figure 6.11 Similar as Fig. 6.4 for sea ice concentration, but for experiment 495-ka, and the difference between 495-ka and Plo-ka. 81
- Figure 6.12 The simulated ice thickness for experiment (a) Plo-ka, (b) 495-ka, (c) 506-ka, (d) 517-ka. 82

Figure 6.13	Similar as Fig. 6.3 for surface air temperature (SAT), but for experiment 506-ka, and the difference between 506-ka and P10-ka. 83
Figure 6.14	Similar as Fig. 6.4 for sea ice concentration, but for experiment 506-ka, and the difference between 506-ka and P10-ka. 84
Figure 6.15	Similar as Fig. 6.3 for surface air temperature (SAT), but for experiment 517-ka, and the difference between 517-ka and P10-ka. 85
Figure 6.16	Similar as Fig. 6.4 for sea ice concentration, but for experiment 517-ka, and the difference between 517-ka and P10-ka. 85
Figure 6.17	Insolation difference between 506 and 495 kyr BP (506-ka - 495-ka), and 517 and 495 kyr BP (517-ka - 495-ka). 86
Figure 6.18	The surface air temperature (SAT) differences between experiment 506-ka and 495-ka (506-ka - 495-ka, left panel), and between experiment 517-ka and 495-ka (517-ka - 495-ka, right panel). 87
Figure 6.19	Similar as Fig. 6.18, but for sea ice concentration. 87

LIST OF TABLES

Table 2.1	Parameters used in our glacial cycle simulations. 13
Table 2.2	Boundary conditions for PMIP ₃ experiments (PI control and LGM). 16
Table 2.3	PMIP ₃ model descriptions. Note that all the models are prescribed with the same boundary conditions. 17
Table 6.1	Orbital parameters and greenhouse gases concentrations used in the experiments. 74
Table 6.2	Globally averaged surface air temperature (SAT) and the simulated Northern Hemisphere (NH) ice sheet volume in the experiments. 75

ACRONYMS

AMOC	Atlantic Meridional Overturning Circulation
AWI-CM	The AWI Climate Model
CMIP	Coupled Model Intercomparison Project
DO	Dansgaard–Oeschger
EMIC	Earth system Model of Intermediate Complexity
GCM	General Circulation Model
LGM	Last Glacial Maximum
MIS	Marine Isotope Stage
NGRIP	North Greenland Ice Core Project
NHIS	Northern Hemisphere ice sheets
PD	Present day
PDD	positive degree-day
PI	preindustrial
PISM	Parallel Ice Sheet Model
PMIP	Paleoclimate Modelling Intercomparison Project
RMSD	root-mean-square deviation
SIA	Shallow Ice Approximation
SLE	Sea Level Equivalent
SMB	Surface Mass Balance
SSA	Shallow Shelf Approximation

Part I

BACKGROUND

GENERAL INTRODUCTION

An ice sheet, also called a continental glacier, is a continuous sheet of land ice that covers an area of more than 50,000 km² and moves outward in many directions (American Meteorological Society, cited 2019). There are two ice sheets currently existing, the Greenland Ice Sheet and the Antarctic Ice Sheet (Fig. 1.1). The Antarctic Ice Sheet is the largest ice mass on the planet, with a potential global sea level contribution of around 58 m. The Greenland Ice Sheet could contribute about 7.4 m sea level rise if all the ice melts.

The Greenland Ice Sheet is the only Northern Hemisphere ice sheet (NHIS) at present day, while there were more ice sheets at times during the past 800,000 years. At the Last Glacial Maximum (LGM) (~21,000 yr BP), there were the Laurentide Ice Sheet, Cordilleran Ice Sheet and Innuitian Ice Sheet on the North American continent; the Barents-Kara Ice Sheet, Fennoscandia Ice Sheet and British-Irish Ice Sheet were in Eurasia (Clark et al., 2009, Fig. 1.2). All the ice sheets contributed to an sea level drop of more than 120 m (Austermann et al., 2013; Lambeck et al., 2014; Whitehouse et al., 2012).

1.1 MOTIVATION

During the past 800,000 years, the Earth’s climate went through vast changes known as glacial-interglacial cycles, with a periodicity of around 100 kyr. The Northern Hemisphere ice sheets advanced and retreated periodically with the same pace. Summer insolation at high northern latitudes is commonly accepted as the main driving and

The Northern Hemisphere ice sheets and the glacial cycles.

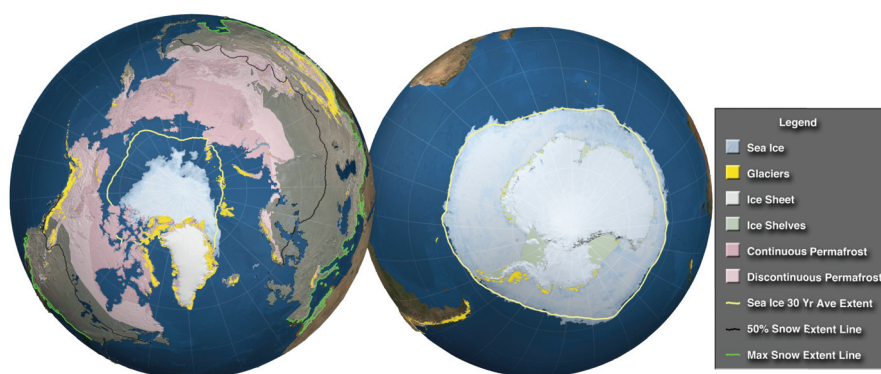


Figure 1.1: Present-day ice sheets, as well as other components of the Cryosphere. (Figure from NASA/Goddard Space Flight Center Scientific Visualization Studio)

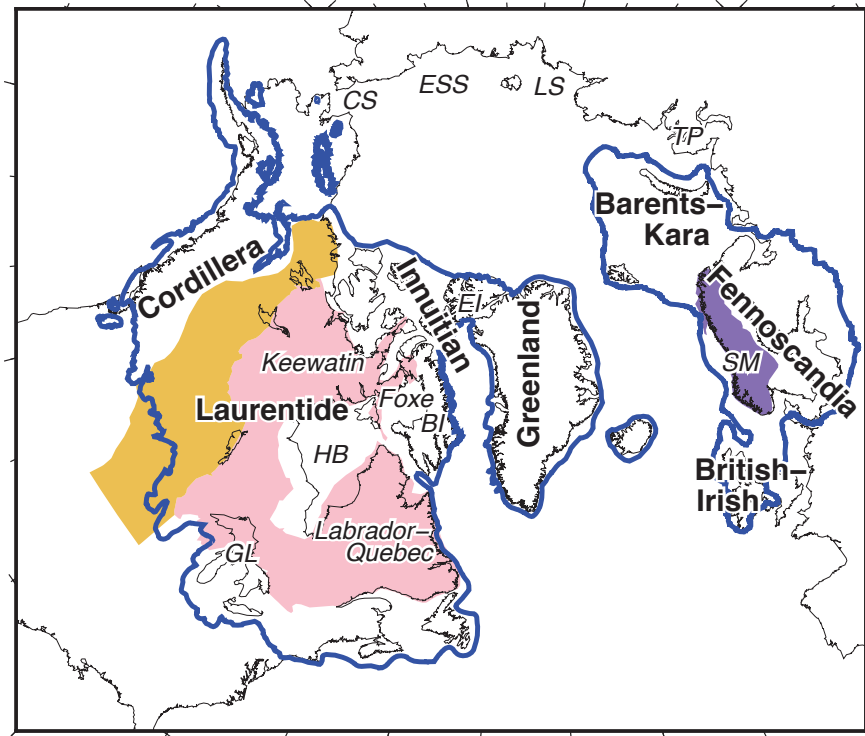


Figure 1.2: Location of Northern Hemisphere ice sheets at the Last Glacial Maximum (21 kyr BP): Cordillera, Laurentide, Innuitian, Greenland, Barents-Kara, Fennoscandia and British-Irish Ice Sheets (blue line; Dyke, 2004; Gowan et al., 2016; Hughes et al., 2016). The locations of the three domes of Laurentide Ice Sheet: Labrador-Quebec, Keewatin and Foxe. The areas mentioned in this study include the Hudson Bay (HB), the Great Lakes (GL), Baffin Island (BI), Ellesmere Island (EI), Taimyr Peninsula (TP), Laptev Sea (LS), East Siberian Sea (ESS) and Chukchi Sea (CS). The yellow area is the Interior Plains, the pink area is the Canadian Shield and the purple area is the Scandinavia Mountains (SM).

modulating factor for glacial-interglacial cycles (Milankovitch theory, Hays et al., 1976; Milankovitch, 1941). However, orbital forcing alone cannot explain the strong 100 kyr cycle of Northern Hemisphere ice sheets, which have larger amplitude, slower build up and faster retreat than the insolation signal. This indicates that internal climatic feedbacks acting as nonlinear amplifiers are also of vital importance (Abe-Ouchi et al., 2013; Huybers, 2011; Huybers and Wunsch, 2005; Imbrie et al., 1993; Lisiecki, 2010).

Northern Hemisphere ice sheets are among the largest topographic features that can amplify, pace or drive global climate change on different time scales (Clark et al., 1999). The extensive coverage of ice sheets lowers surface albedo and alters the Earth's energy budget (Abe-Ouchi et al., 2007). Large ice sheet height can modify atmospheric circulation, downwind ocean surface temperature and sea ice coverage (Liakka et al., 2012; Löfverström et al., 2014, 2015; Ullman et al., 2014; Zhang et al., 2014b). The freshwater flux from ice sheet melt and ice-rafting from ice sheet calving also can modulate the strength of Atlantic Meridional Overturning Circulation (AMOC) and result in global scale climate shifts (Bond and Lotti, 1995; Carlson and Clark, 2012; Ganopolski and Rahmstorf, 2001).

Given the importance of the ice sheets in the climate system, full reconstruction of both their extent and geometry is essential. Using radiocarbon-dating, geomorphological features, relative sea level reconstructions or other types of geological data, the evolution of the Northern Hemisphere ice sheets has been reasonably established since the LGM (Carlson and Clark, 2012; Clark et al., 2009; Dyke, 2004; Gowan et al., 2016; Hughes et al., 2016; Margold et al., 2015). However, it remains poorly constrained prior to the LGM (Kleman et al., 2010; Svendsen et al., 2004). The geometry, volume and exact timing of ice sheet evolution is difficult to infer from the geological record alone because the most recent glaciation destroyed older landforms.

Alternatively, numerical modelling is an effective way for assessing the dynamic evolution of ice sheets, as well as understanding the interactions between ice sheets and other climate components (e.g. Stokes et al., 2012). Ideally, the ice sheet models are embedded within global circulation models to capture the feedbacks between the climate and the ice sheet. However, this approach is not yet computationally feasible over glacial-interglacial time scales. Therefore, the interactions between the climate and ice sheets are often studied separately with comprehensive models. Climatic effects on ice sheets under glacial-interglacial scales still need to be better constrained.

In this thesis, we use numerical modelling to scrutinize the climatic influence on Northern Hemisphere ice sheet (NHIS) evolution. The role of atmosphere is the main focus, since the Northern Hemisphere ice sheets are mainly land-based and are strongly influenced by the atmosphere.

Why are the Northern Hemisphere ice sheets important?

How to infer the Northern Hemisphere ice sheet evolution?

Climatic influence matters!

1.2 OBJECTIVES AND STRUCTURE OF THE THESIS

The general structure of this thesis is as follows. Chapter 2 provides the model description of the conducted research. Chapter 3 to 6 present the main findings of the thesis. Chapter 7 contains the final summary and an outlook. The work in Chapter 3 and 4 is published in Niu et al. (2019b) in *Journal of Glaciology*. The work in chapter 5 is published in Niu et al. (2019a) in *Geophysical Research Letters*. The work in chapter 6 is in preparation in Niu et al. (in prep).

There are several specific questions addressed in this thesis:

1. **Was the Northern Hemisphere ice sheet evolution solely consistent with a linear combination of a glacial and interglacial climate state during the last glacial cycle?** (Chapter 3)

From previous studies, the answer is negative (e.g. Charbit et al., 2007). The nonlinear feedback between ice sheet and climate or unresolved processes are not taken into account. In our study, with a new generation of General Circulation Model (GCM) as forcing, we show to what extent the model can reproduce realistic Northern Hemisphere ice sheet evolution. By comparing with independent ice sheet reconstructions, we deduce highly sensitive regions and time periods that are influenced by other nonlinear processes.

2. **What are the effects of upper boundary conditions on Northern Hemisphere ice sheet modelling?** (Chapter 4)

The climate forcing is found to be model dependent. In this chapter, we test the sensitivity of simulated Northern Hemisphere ice sheets which arises from uncertain climate forcing. By using output from The Paleoclimate Modelling Intercomparison Project (PMIP) Phase III, we discuss the resultant uncertainty and the major contributor of the ice sheet development.

3. **What are the effects of climate variability on Northern Hemisphere ice sheet mean state?** (Chapter 5)

Evidence from proxies indicates that millennial-scale abrupt climate shifts, called Dansgaard–Oeschger (DO) events, happened during past glacial cycles. In this chapter, we show that the DO events can regulate the mean state of the Northern Hemisphere ice sheets (NHIS). More generally, we investigate the influence of climate variability (hereafter called "climate noise") on the mean state of the ice sheets. The most likely interpretation of the results is also discussed.

4. **What are the effects of orbital change on Northern Hemisphere ice sheet evolution during Marine Isotope Stage 13?** (Chapter 6)

Records from Antarctic ice cores and the benthic $\delta^{18}\text{O}$ data indicate that the interglacial during Marine Isotope Stage (MIS) 13 ($\sim 524 - 474$ kyr BP) was relatively cold and ice sheets were likely larger. In this chapter, using a coupled climate-ice sheet model, we investigate the influence of different orbital configurations on MIS 13 climate. From the perspective of equilibrium simulations, we discuss the resultant Northern Hemisphere ice sheet states.

MODEL DESCRIPTION

2.1 THE ICE SHEET MODEL

The Parallel Ice Sheet Model (PISM) (version 0.7.3) is an open source, three-dimensional thermo-mechanically coupled shallow ice sheet model (Aschwanden et al., 2012; Bueler and Brown, 2009; The PISM authors, 2016; Winkelmann et al., 2011, Fig. 2.1). We implemented an atmospheric module into the model with a glacial index forcing scheme, based on PISM's extensible atmosphere and ocean coupling feature. The solid earth deformation (glacial isostatic adjustment, GIA) is calculated with the Lingle and Clark method (Bueler et al., 2007; Lingle and Clark, 1985). The spatial domain is defined on a Northern Hemisphere polar stereographic grid. The horizontal resolution is 20 km or 40 km in our study.

A combination of Shallow Ice Approximation (SIA) and Shallow Shelf Approximation (SSA) ("SIA+SSA hybrid") is used to compute stress balances in the ice. The Glen-Paterson-Budd-Lliboutry-Duval flow law is used for ice rheology, in which ice deformation is a function of temperature, pressure and liquid water fraction (Aschwanden et al., 2012). Eigencalving (Levermann et al., 2012) and thickness-calving routine are used for the ice shelf calving, which means that the calving is controlled by the horizontal strain rates and a threshold of ice thickness. Surface mass balance is computed by the semi-empirical positive degree-day (PDD) scheme. More details are described in the following sections.

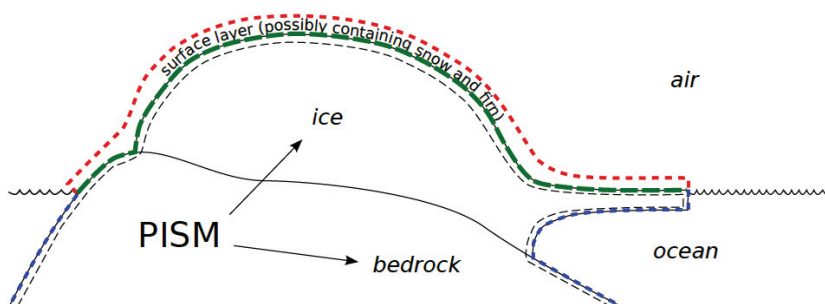


Figure 2.1: PISM's view of interfaces between an ice sheet and the outside world (The PISM authors, 2016)

2.1.1 Ice Dynamics

The stress balance computation is a combination of the [SIA](#) and [SSA](#), which are dominant in grounded and floating ice respectively. Other regions such as ice streams, which have significant internal ice deformation and basal sliding are solved by combining the velocity solution of the two approximations (Bueler and Brown, 2009; Winkelmann et al., 2011).

Isotropic ice rheology is used for ice deformation (Paterson, 1994), called the Glen-Paterson-Budd-Lliboutry-Duval flow law (Aschwanden et al., 2012; Lliboutry and Duval, 1985; Paterson and Budd, 1982). Governed by the Glen constitutive law (Glen, 1952; Nye, 1953), ice deformation is temperature dependent, while also a function of pressure and liquid water fraction. A non-dimensional enhancement factor for both [SIA](#) and [SSA](#) is applied to the flow law. Following the recommendations of Cuffey and Paterson (2010), we set the [SIA](#) enhancement factor E_{SIA} to 5. The values of the other parameters and related references are summarized in Table 2.1. Surface gradients are computed by finite differences to determine the driving stress. The conservation of energy is solved within the ice, the subglacial layer and a layer of thermal bedrock. A geothermal heat flux input is included at the lower boundary. For initialization, the ice temperature is set to the solution of a steady one-dimensional differential equation in which conduction and vertical advection are in balance. The vertical velocity is calculated by linearly interpolating between the surface mass balance rate at the top and zero at the bottom (Aschwanden et al., 2012; The PISM authors, 2016).

2.1.2 The Subglacial Dynamics

The basal resistance to ice flow is computed based on the hypothesis that a layer of till underlies the ice sheet (Bueler and Brown, 2009; Clarke, 2005). A pseudo-plastic sliding law is used for determining sliding:

$$\vec{\tau}_b = -\tau_c \frac{\vec{u}}{u_{\text{threshold}}^q |\vec{u}|^{1-q}}, \quad (2.1)$$

where $\vec{\tau}_b$ is the basal shear stress, τ_c is the yield stress, \vec{u} is the sliding velocity and $u_{\text{threshold}}$ is a parameter called threshold velocity and q is the pseudo-plastic sliding exponent (Table 2.1).

The Mohr-Coulomb criterion (Cuffey and Paterson, 2010) is used to determine the yield stress τ_c ,

$$\tau_c = c_0 + (\tan \phi) N_{\text{till}}, \quad (2.2)$$

which is related to the till material property (the till friction angle ϕ) and the effective pressure of the saturated till N_{till} . The till friction

angle value, $\phi = 30^\circ$, is a typical value from lab experiments (Cuffey and Paterson, 2010, p. 268). The till cohesion value, c_0 , is set to 0 (Schoof, 2006). The effective pressure, N_{till} , is determined by the following parameterization:

$$N_{\text{till}} = \delta P_o 10^{(e_0/C_c)(1-(W_{\text{till}}/W_{\text{till}}^{\text{max}}))}. \quad (2.3)$$

This is based on laboratory experiments on till extracted from an ice stream in Antarctica (Tulaczyk et al., 2000b). P_o is the ice overburden pressure, W_{till} is the effective thickness of water in the till, $W_{\text{till}}^{\text{max}}$ is the maximum amount of water in the till, e_0 is the till reference void ratio, C_c is the till compressibility coefficient and δ is the effective fraction overburden pressure in the till. The water in the base is not conservative in our simulations, it is stored in the till up to the maximum thickness ($W_{\text{till}}^{\text{max}}$). The water exceeding that thickness is drained off instantaneously (Bueller and Brown, 2009; Tulaczyk et al., 2000a).

2.1.3 The Ice Shelf Dynamics

The model for marine portions of ice sheets is from the PIK (Potsdam Institute for Climate Impact Research) component of PISM (Albrecht et al., 2011; Levermann et al., 2012; Winkelmann et al., 2011). The flotation criterion for determining whether the ice floating or grounded is combined with a time-dependent land-sea mask, including relative sea level change. For ice shelf dynamics in PISM, SSA is dominant. The ice shelf calving mechanism is controlled by two schemes. The calving rate is a function of the horizontal strain rates, but the ice shelf is automatically removed when the ice thickness is thinner than the threshold (H_{calthres}) of 200 m.

For the boundary condition at the base of the ice shelf, we follow the setup from Martin et al. (2011). The ice at the basal boundary is at pressure melting temperature. The mass flux from ice shelf to ocean is related to the heat flux Q_{heat} between ocean and ice (Martin et al., 2011, Eq. 3-5), which is:

$$Q_{\text{heat}} = \rho_{\text{oce}} c_{\text{poce}} \gamma_T F_{\text{melt}} (T_{\text{oce}} - T_f). \quad (2.4)$$

Here, ρ_{oce} is density of ocean water. c_{poce} is specific heat capacity of ocean mixed layer. γ_T is the thermal exchange velocity. T_f is a virtual temperature which represent the ocean water freezing temperature at different depths. The ocean temperature, T_{oce} , is set to a constant value of -1.7°C (Beckmann and Goosse, 2003). F_{melt} is a dimensionless model parameter that we set to 1×10^{-2} to increase the melt rate.

2.1.4 The Surface Processes

Within the surface processes layer, surface mass balance is computed by the semi-empirical positive degree-day (PDD) scheme (Reeh, 1989). Instead of taking radiative heat fluxes directly as forcing, it assumes that the melt rate of snow and ice is proportional to the sum of the positive surface air temperature values over the year. The related PDD parameters (Table 2.1) are the amount of snow or ice that melts per Kelvin and day. They are calibrated using measurements from present day ice sheets and glacier surfaces (Ritz, 1997). The PDD method is widely used for paleo ice sheet modelling since it requires less variables than energy balance models and is computationally efficient (e.g. Charbit et al., 2007; Charbit et al., 2002; Greve et al., 1999; Marshall et al., 2000, 2002; Rodgers et al., 2004; Tarasov and Peltier, 2004; Zweck and Huybrechts, 2005).

In PDD scheme, the monthly mean surface air temperature and precipitation are used as input. For accumulation, precipitation when temperature is below 0 °C is considered to be snow, and temperature above 2 °C is considered to be rain. For temperatures intermediate of these values, the percentage of snow and rain is linearly interpolated. For ablation, the PDD value is calculated as follows (Calov and Greve, 2005, Eq. 6):

$$PDD = \int_0^A dt \left[\frac{\sigma}{\sqrt{2\pi}} \exp\left(-\frac{T_{\text{mon}}^2}{2\sigma^2}\right) + \frac{T_{\text{mon}}}{2} \operatorname{erfc}\left(-\frac{T_{\text{mon}}}{\sqrt{2}\sigma}\right) \right]. \quad (2.5)$$

A random temperature with a normal distribution with a mean value of 0 ("white noise" variation) is added onto the monthly mean temperature at each grid point to account for synoptic variability. The standard deviation σ is 5 K.

Table 2.1: Parameters used in our glacial cycle simulations.

Parameter	Name	Value	Unit	Reference
E_{SIA}	SIA enhancement factor	5.0	1	Cuffey and Paterson, 2010
E_{SSA}	SSA enhancement factor	1.0	1	Cuffey and Paterson, 2010
q	Pseudo-plastic sliding exponent	0.25	1	Aschwanden et al., 2013
$u_{\text{threshold}}$	Pseudo-plastic threshold velocity	100.0	m a^{-1}	Aschwanden et al., 2013
ϕ	Till friction angle	30	$^{\circ}$	Cuffey and Paterson, 2010, p. 268
c_0	Till cohesion	0	kPa	Schoof, 2006
e_0	Till reference void ratio	0.69	1	Tulaczyk et al., 2000b
C_c	Till compressibility coefficient	0.12	1	Tulaczyk et al., 2000b
δ	Till effective fraction overburden	0.01	1	-
$W_{\text{fill}}^{\text{max}}$	Maximum amount of water in till	1	m	-
H_{calthres}	Calving ice threshold thickness	200	m	-
T_{oce}	Ocean temperature	-1.7	$^{\circ}\text{C}$	Beckmann and Goosse, 2003
F_{melt}	Ocean model melt factor	1×10^{-2}	1	-
σ	Standard deviation of the daily temperature	5.0	K	Ritz, 1997
F_{snow}	PDD factor for snow	3.3×10^{-3}	$\text{m K}^{-1} \text{day}^{-1}$	Ritz, 1997
F_{ice}	PDD factor for ice	8.8×10^{-3}	$\text{m K}^{-1} \text{day}^{-1}$	Ritz, 1997
θ_{refreeze}	Refreezing rate of melted snow	0.6	1	Ritz, 1997

2.2 THE CLIMATE

This section describes the upper boundary conditions used for standalone ice sheet modelling.

2.2.1 *The Glacial Index Method*

Ideally, coupling an ice sheet model to a sophisticated General Circulation Model (GCM) is an effective way to produce numerical ice sheet reconstructions. However, this approach is not yet computationally feasible over glacial-interglacial time scales. Alternatively, an approach of coupling ice sheet models to Earth system Model of Intermediate Complexitys (EMICs) (Claussen et al., 2002) has been used (e.g., Bauer and Ganopolski, 2017; Charbit et al., 2005; Fyke et al., 2011; Ganopolski et al., 2010). The missing processes in EMICs due to the coarse spatial resolution may also have large effects on regional ice sheet distributions.

Another approach for long-term ice sheet simulations is the Glacial Index method. It synthesizes the necessary boundary conditions by combining the temporal evolution of the climate as deduced from climate reconstructions (often based on an ice core record, since the isotope record is correlated with temperature) with the spatial signature of glacial and interglacial climate modes deduced from a limited number of time slice simulations (e.g., Charbit et al., 2007; Charbit et al., 2002; Greve et al., 1999; Marshall et al., 2000, 2002; Rodgers et al., 2004; Tarasov and Peltier, 2004; Zweck and Huybrechts, 2005). The basis of this approach is the assumption that to first order climate can be separated into a spatial mode and a temporal index globally modulating it over time. The climate patterns are usually only available as time slice experiments for specific, well constrained periods, such as the LGM or the preindustrial (PI). The glacial index approach is computationally fast, and is efficient for testing the sensitivity of ice sheet response to climate forcing.

For our standalone ice sheet modelling, the index is defined as follows:

$$I(t) = \frac{\delta^{18}O(t) - \delta^{18}O_{PI}}{\delta^{18}O_{LGM} - \delta^{18}O_{PI}}, \quad (2.6)$$

where $\delta^{18}O(t)$ is an isotopic ice core record from Greenland or Antarctica for representing the global temperature variations. The isotopic values of $\delta^{18}O_{LGM}$ and $\delta^{18}O_{PI}$ represent full glacial conditions and interglacial conditions respectively. Thus, the value of I is 1 for the LGM ($t = 21$ kyr BP, $\delta^{18}O(t) = \delta^{18}O_{LGM}$) and 0 for present-day ($t=0$ kyr BP, $\delta^{18}O(t) = \delta^{18}O_{PI}$). For the other time periods, the index is linearly interpolated.

The paleoclimate fields calculated using the index method are based on the linear relationship between the present-day and the LGM:

$$T_m(t, x, y) = T_{mPI}(x, y) + \frac{T_{mLGM}(x, y) - T_{mPI}(x, y)}{I_{LGM} - I_{PI}} I(t), \quad (2.7)$$

$$P_{m1}(t, x, y) = P_{mPI}^*(x, y) + \frac{P_{mLGM}(x, y) - P_{mPI}^*(x, y)}{I_{LGM} - I_{PI}} I(t), \quad (2.8)$$

$$P_{m2}(t, x, y) = \max[P_{m1}(t, x, y), 0], \quad (2.9)$$

$$P_m(t, x, y) = P_{m2}(t, x, y) \cdot \exp[-\beta H(t, x, y)]. \quad (2.10)$$

Here T_m and P_m are long-term monthly mean surface temperature and precipitation. Equation 2.9 is used to avoid negative precipitation. Equation 2.10 is a precipitation correction due to surface elevation (H) change, based on the exponential relationship between water vapor saturation pressure and temperature in the upper atmosphere. A tuning parameter β is used for reducing the precipitation at high elevations, so that the modelled ice sheet volume matches the global sea level curve. A slight modification is made for present day precipitation to eliminate the error caused by the precipitation elevation correction:

$$P_{mPI}^*(x, y) = P_{mPI}(x, y) \cdot \exp[\beta H_{PI}(x, y)]. \quad (2.11)$$

A freely evolving lapse rate correction for temperature is not included for two reasons. Firstly, the climate forcing at the LGM has already accounted for temperature change due to elevation change. Secondly, including a temperature lapse rate correction will give the ice sheet one extra degree of freedom to evolve.

2.2.2 The Climate Model COSMOS

The climate used for forcing the Northern Hemisphere ice sheets (NHIS) through the last glacial cycle (Chapter 3) is derived from the Community Earth System Models COSMOS. It includes the atmosphere model ECHAM5, ocean model MPI-OM and a land-vegetation model JSBACH. ECHAM5 is in T31 resolution ($\sim 3.75^\circ$) with 19 levels, MPI-OM is in GR30 resolution ($3.0^\circ \times 1.8^\circ$) with 40 levels.

The COSMOS Earth system model has been used and evaluated for different paleo climate scenarios, like the last millennium (Jungclaus et al., 2010), the Miocene warm climate (Knorr et al., 2011; Knorr and Lohmann, 2014), the Pliocene (Stepanek and Lohmann, 2012), internal variability of climate system (Wei et al., 2012), Holocene variability (Fischer and Jungclaus, 2011; Wei and Lohmann, 2012), and the glacial climate (Gong et al., 2013; Zhang et al., 2013). It is appropriate as the climate forcing for our PISM simulations.

2.2.3 The Paleoclimate Modelling Intercomparison Project III (PMIP3)

The first generation of The Paleoclimate Modelling Intercomparison Project (PMIP) was in the early 1990s, during which the climate-

Table 2.2: Boundary conditions for PMIP₃ experiments (PI control and LGM).

Boundary Conditions		PI	LGM
Orbital	<i>eccentricity</i>	0.016724	0.018994
Parameters	<i>obliquity</i>	23.446 °	22.949 °
	<i>perihelion-180°</i>	102.04 °	114.42 °
Trace	CO ₂	280 ppm	185 ppm
Gases	CH ₄	760 ppb	350 ppb
	N ₂ O	270 ppb	200 ppb
Ice Sheet Configuration		Modern	ICE-6G, GLAC, ANU

modelling community were aware that the climate changes response to forcing are model dependent. The project were established to better understand the Earth system, as well as evaluate the capability of state-of-art models to reproduce different climates. Thus, coordinated model experiments were set among different modelling groups, so that model-model and model-data comparisons can be conducted. For the first phase (PMIP₁), the project focused on atmosphere-only GCMs. For the second and the third phase, comparisons among coupled atmosphere-ocean models and atmosphere-ocean-vegetation models were conducted. In PMIP₃, the chosen coordinated paleoclimate experiments include mid-Holocene, the LGM, Last millennium (past 1000 years), early-Holocene, 8.2 kyr BP event, Last Interglacial, mid-Pliocene and the preindustrial (PI) (serves as baseline and included in Coupled Model Intercomparison Project (CMIP) 5). In our study, we mainly use the PI and the LGM experiments.

There are nine PMIP₃ models available online for both PI and LGM experiments. For model comparison, all models use the same boundary conditions (orbital parameters, trace gases and ice sheet configuration, see Table 2.2). The Preindustrial Control run use modern-day ice sheet configuration, greenhouse gases around 1750 and orbital parameters for 1950 AD. For the LGM experiment, the orbital parameters are from Berger (1978), trace gases values are from Dällenbach et al. (2000), Flückiger et al. (1999), and Monnin et al. (2001). The ice sheet configuration is a blended product obtained by averaging three different ice sheet reconstructions: ICE-6G, GLAC and ANU (Abe-Ouchi et al., 2015). More details of the protocols can be found at <https://pmip3.lsce.ipsl.fr/>.

2.3 THE COUPLED CLIMATE-ICE SHEET MODEL

Figure 2.2 illustrates the coupling scheme between General Circulation Model (GCM) The AWI Climate Model (AWI-CM) and the ice sheet model PISM. The variable fields are exchanged through iterative

Table 2.3: PMIP3 model descriptions. Note that all the models are prescribed with the same boundary conditions.

Model	Group ^a	Atm. resolution	Carbon cycle	Reference
COSMOS-AWI	AWI	96x48xL19 (T31L19)	yes	Stepanek and Lohmann, 2012; Zhang et al., 2013
CCSM4	NCAR	288x192xL26	no	Andres and Peltier, 2013; Brady et al., 2013; Tian and Jiang, 2013; Vettoretti and Peltier, 2013
CNRM-CM5	CNRM /CER-FACS	256x128xL31	no	Voltaire et al., 2013
COSMOS-ASO	FUB	96x48xL19 (T31L19)	yes	Budich et al., 2010; Radatz et al., 2007; Roeckner et al., 2003, 2004; Valcke, 2006; Wetzel et al., 2010
FGOALS-g2	LASG /IAP	128x60xL26	no	Zheng and Yu, 2013
GISS-E2-R	GISS	144x90xL40	no	Schmidt et al., 2014
IPSL-CM5A-LR	IPSL	96x95xL39	yes	Kageyama et al., 2013a,b
MIROC-ESM	MIROC	128x64xL80	yes	Ohgaito et al., 2013; Sueyoshi et al., 2013
MPI-ESM-P	MPI	196x98xL47 (T63L47)	no	Giorgetta et al., 2013; Jungclaus et al., 2013; Man et al., 2014
MRI-CGCM3	MRI	320x160xL48 (TL159L48)	no	Yukimoto et al., 2012

^a **AWI**: Alfred Wegener Institute Helmholtz Center for Polar and Marine Research. **NCAR**: National Center for Atmospheric Research. **CNRM/CERFACS**: Centre National de Recherches Météorologiques / Centre Européen de Recherche et Formation Avancée, Calcul Scientifique. **FUB**: Freie Universität Berlin, Institute for Meteorology. **LASG/IAP**: LASG, Institute of Atmospheric Physics, Chinese Academy of Sciences and CESS, Tsinghua University. **GISS**: NASA Goddard Institute for Space Studies. **IPSL**: Institut Pierre-Simon Laplace. **MIROC**: Japan Agency for Marine-Earth Science and Technology, Atmosphere and Ocean Research Institute (The University of Tokyo), and National Institute for Environmental Studies. **MPI**: Max-Planck-Institut für Meteorologie (Max Planck Institute for Meteorology). **MRI**: Meteorological Research Institute.

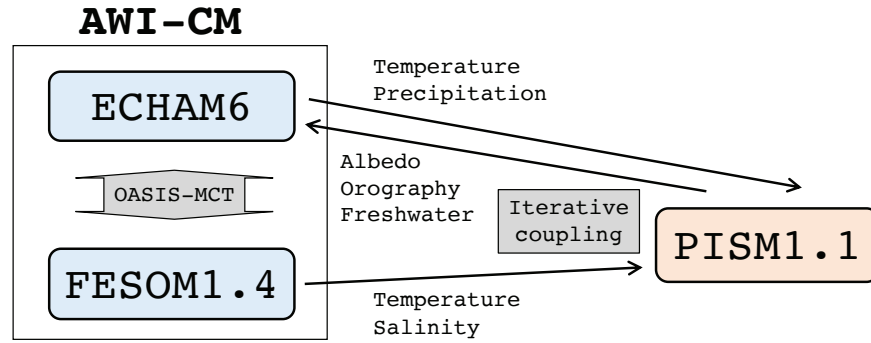


Figure 2.2: Schematic of coupling between the climate model AWI-CM and ice sheet model PISM.

coupling. Firstly, the climate model with prescribed ice boundaries is integrated for a certain period, then the ice sheet model is switched on and integrated with prescribed climate forcing. The ice configuration in AWI-CM is then updated according to the PISM results for the new run. As such the simulations between the climate model and the ice sheet model are changed back and forth. The details of the climate model and the coupling scheme are described in Sect. 2.3.1 and 2.3.2.

2.3.1 The Climate Model AWI-CM

The AWI Climate Model (AWI-CM) is a coupled atmosphere-ocean model developed at Alfred Wegener Institute (AWI, Rackow et al., 2018; Sidorenko et al., 2015). The atmosphere model is ECHAM6, the ocean model is the Finite Element Sea ice-Ocean Model (FESOM, version 1.4). FESOM and ECHAM6 exchange data every 6 model hours via OASIS₃-MCT.

ECHAM6 is the sixth generation of the ECHAM series of atmospheric general circulation models that is developed at the Max Planck Institute for Meteorology in Hamburg (Stevens et al., 2013). It incorporates between diabatic processes and large-scale circulations. The spectral-transform dynamical core is based on vorticity and divergence form of the primitive equations, with temperature and surface pressure being the thermodynamic coordinates. It also consists of a transport model for other scalar quantities and a suite of physical parameterizations for diabatic processes or boundary data sets for externalized parameters. Besides, it contains the JSBACH land vegetation model that accounts for the land processes, e.g. the heat and water storage and exchange with the atmosphere, photosynthesis, carbon processes in plants and soils and hydrological discharge (hydrological model). The resolution is T63 ($\sim 1.9^\circ$) with 47 vertical levels, resolving the atmosphere at up to 0.01 hPa.

FESOM 1.4 is a global sea-ice ocean model on an unstructured-mesh with multi-resolution modelling functionality developed at AWI

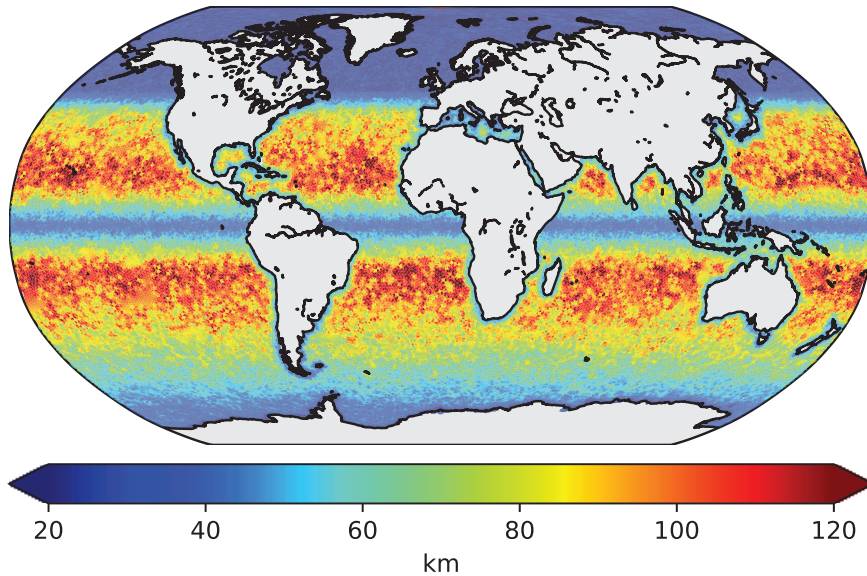


Figure 2.3: The spatial resolution of FESOM mesh, with higher resolution applied along the coasts and in polar and tropical regions.

(Danilov et al., 2004; Wang et al., 2014). With the unstructured mesh, high spatial resolution can be applied in dynamically active regions while a relative coarse resolution can be kept elsewhere to save computational demand (Fig. 2.3). It uses finite elements to solve the hydrostatic primitive equations. The variational formulation with the finite element method includes two steps. Firstly, the primitive equations are multiplied by a test function and integrated over the model domain. Secondly, the unknown variables are approximated with a sum over a finite set of basis functions. A combination of continuous, piecewise linear basis functions in two dimensions for surface elevation and in three dimensions for velocity and tracers are used. For 2D FESOM, the triangular surface mesh with 126859 nodes is used (CORE II mesh). For 3D FESOM, the mesh is generated by dropping vertical lines from the surface 2D nodes with 46 vertical z-level grids (3668773 nodes). The spatial resolution ranges from ~ 10 km to ~ 180 km.

AWI-CM shows comparative performance as other sophisticated climate models (e.g. models that participated in the fifth phase of CMIP), regarding not only the present-day mean climate state but also the internal climate variability (Danilov et al., 2004; Wang et al., 2014). In addition, AWI-CM is also used for investigating the dynamics of paleoclimate, e.g. the LGM, the mid-Holocene, and the last interglacial. The model version used in this study follows the guidelines of the framework of CMIP6 and PMIP4 in low resolution (AWI-ESM-1.1-LR), in which dynamic vegetation is also included.

2.3.2 *The Coupling to Ice Sheet Model PISM*

The ice sheet model coupled to [AWI-CM](#) is [PISM](#) version 1.1 (Sect. 2.1). The spatial resolution of the ice sheet simulations is 20 km. The [SIA](#) enhancement factor E_{SIA} is set to 2 (Cuffey and Paterson, 2010). The other parameter settings for the ice sheet dynamics are the same as the standalone ice sheet model setup. Here, [PISM](#) is forced by both the atmosphere and the ocean from [AWI-CM](#).

The variable exchange between [AWI-CM](#) and [PISM](#) happens through iterative coupling (Fig. 2.2). For the ice sheet model [PISM](#), the surface air temperature and precipitation from ECHAM6 is taken as atmospheric forcing. Then the surface melt is calculated based on the [PDD](#) scheme. The ocean temperature and salinity from FESOM is taken as ocean forcing. For the climate model [AWI-CM](#), the updated albedo, orography and freshwater change are used as new boundaries. The ice volume change due to ablation, calving, and basal melting under grounded ice or ice shelves, is considered as freshwater discharge into the ocean via the hydrological model in ECHAM6. The change of bathymetry in FESOM due to the migration of the grounding line or ice shelf change is not technically applicable at this moment. Because FESOM has an unstructured mesh, changing bathymetry would require a change of the ocean mesh and that is not yet possible. Bilinear interpolation is used to account for the mismatch of the resolution between the atmosphere or ocean model and the ice sheet model.

The response times of the Earth system components to changes in the forcing differ strongly. The atmosphere, the land and ocean surface are fast components. The response timescale to a perturbed forcing is within tens of years. For the deep ocean circulation, the timescale is of the order of thousand years. The ice sheets require the longest timescale for reaching equilibrium states, which can be tens of thousands of years. As a result, the timescale of reaching equilibrium state of the Earth system depends on the slowest climate components, i.e. the ice sheet and the deep ocean.

The coupling between the climate model and the ice sheet model can either be synchronous or asynchronous. In case of synchronous coupling, both models run with the same time periods before data exchange. This can be applied in transient simulations when the boundary conditions require being updated timely. However, it is computationally expensive especially for the climate model, which can only be integrated for tens of model years per day. Alternatively, asynchronous coupling can be used especially for equilibrium state simulations. In this case, the climate model with fast components can be integrated for a shorter time period while the slowly changing ice sheets are integrated for a longer time period.

In this thesis, we focus on simulating equilibrium Earth system states. Therefore, we use asynchronous coupling, with 1-year climate modelling versus 100-year ice sheet modelling.

Part II

THE SHOWCASE 1

— The standalone ice sheet modelling.

NORTHERN HEMISPHERE ICE SHEET EVOLUTION THROUGH THE LAST GLACIAL CYCLE

3.1 INTRODUCTION

Northern Hemisphere ice sheets are among the largest topographic scales during the last glacial period. Numerical simulations are essential for understanding the relation between ice sheets and the other climate components. However, neither climate reconstructions nor off-line paleo climate simulations provide the temporally and spatially-varying boundary conditions required for simulations with stand-alone ice sheet models. Climate reconstructions are too sparse to provide a spatially detailed temperature distribution and usually do not provide reliable, quantitative precipitation information. Climate simulations rely on reconstructed ice sheet geometries as a boundary condition and are usually only available as time slice experiments for specific, well constrained periods, such as the LGM or the preindustrial (PI). Based on these time slice experiments and combined with glacial index method, the dynamics of Northern Hemisphere ice sheets have been studied on different time periods, e.g. the Last Deglaciation, the LGM or the whole last glacial cycle (Charbit et al., 2007; Charbit et al., 2002; Greve et al., 1999; Marshall et al., 2000, 2002; Rodgers et al., 2004; Tarasov and Peltier, 2004; Zweck and Huybrechts, 2005).

In this chapter, by using the glacial index method, we simulated Northern Hemisphere ice sheet evolution through the last glacial cycle with climate forcing from COSMOS. Comparisons between the simulated results and the geological reconstructions are conducted both spatially and temporally. By comparing with independent ice sheet reconstructions, we first evaluated the model performances and show to what extent the model can reproduce the realistic Northern Hemisphere ice sheet evolution. Moreover, we deduce highly sensitive regions and time periods that cannot be inferred from the first order climate pattern. These cases may indicate the sensitive regions that influenced by nonlinear feedback and unresolved processes.

3.2 EXPERIMENT DESIGN

The spatial domain of ice sheet modelling covers the Northern Hemisphere using a polar stereographic grid with a resolution of 20x20 km. For the climate forcing, we use the index method that described in Sect. 2.2.1. The glacial index is derived from the North Greenland

Ice Core Project (NGRIP) $\delta^{18}\text{O}$ 50-year average record (Andersen et al., 2004, 122.95 kyr BP - 0 kyr BP, Fig. 3.1a). The value of I is 1 for LGM and 0 for Present day (PD) ($I_{\text{LGM}}=1$, $t=21$ kyr BP; $I_{\text{PI}}=0$, $t=0$ kyr BP; Equ. 2.6), which represent full glacial conditions and interglacial conditions respectively. The climate forcing at the LGM (T_{mLGM} and P_{mLGM}) is from equilibrium simulations using GCM COSMOS, with simulations conducted at Alfred Wegener Institute Helmholtz Center for Polar and Marine Research (Zhang et al., 2013, COSMOS-AWI, Fig. 3.2a-b and 3.3a-b). External forcing and boundary conditions are set according to the PMIP3 protocol (Sect. 2.2.3). For present-day climate, the air temperature fields are from NCEP/NCAR Reanalysis long term monthly mean datasets (1981-2010, Fig. 3.2c-d; Kalnay et al., 1996). Precipitation fields are from GPCP long term monthly mean datasets (1981-2010, Fig. 3.3c-d; Adler et al., 2003). Moreover, we also ran simulation using the climate output of preindustrial (PI) run from COSMOS as present-day climate. All the climate fields are bilinearly interpolated onto the ice sheet model grids.

As is shown in Fig. 3.2e-f and 3.3e-f, the surface air temperature at the LGM is colder than PD globally except for some areas in the southern part of Eurasian continent. Due to higher elevation and albedo, the surface temperature where ice sheets existed at the LGM can be lower by up to -36 °C from PD both in winter and summer. Less precipitation existed in the eastern part of North America and Scandinavia in winter at the LGM than PD, while more precipitation was in the northwestern part of North America and southwest of England. In summer, less precipitation was in northern North America and more precipitation in southern North America at the LGM than PD.

The model run starts at 122.9 kyr BP during the Last Interglacial (from 122.9 to 0 kyr BP). The initial conditions are set to present day. The basal topography data we use is ETOPO1 (Amante and Eakins, 2009). The basal geothermal heat flux data is from Davies (2013). All of the data are bilinearly interpolated onto the 20 km model grid. The relative sea level time series for the land-sea mask is from Rohling et al. (2014, Fig. 3.1b). We use the tuning parameter ($\beta = 0.75 \text{ km}^{-1}$, Equ. 2.10) to match the modelled ice sheet volume with the global sea level curve at the LGM within those observation uncertainties (Austermann et al., 2013; Lambeck et al., 2014; Whitehouse et al., 2012). By increasing β , the amount of precipitation can be reduced considerably. Otherwise, the modelled sea level equivalent at the LGM can be twice as large as the far field sea level record.

3.3 RESULTS

We analyzed the simulated ice sheet evolution both spatially and temporally. We compared the performance of the simulated ice sheets

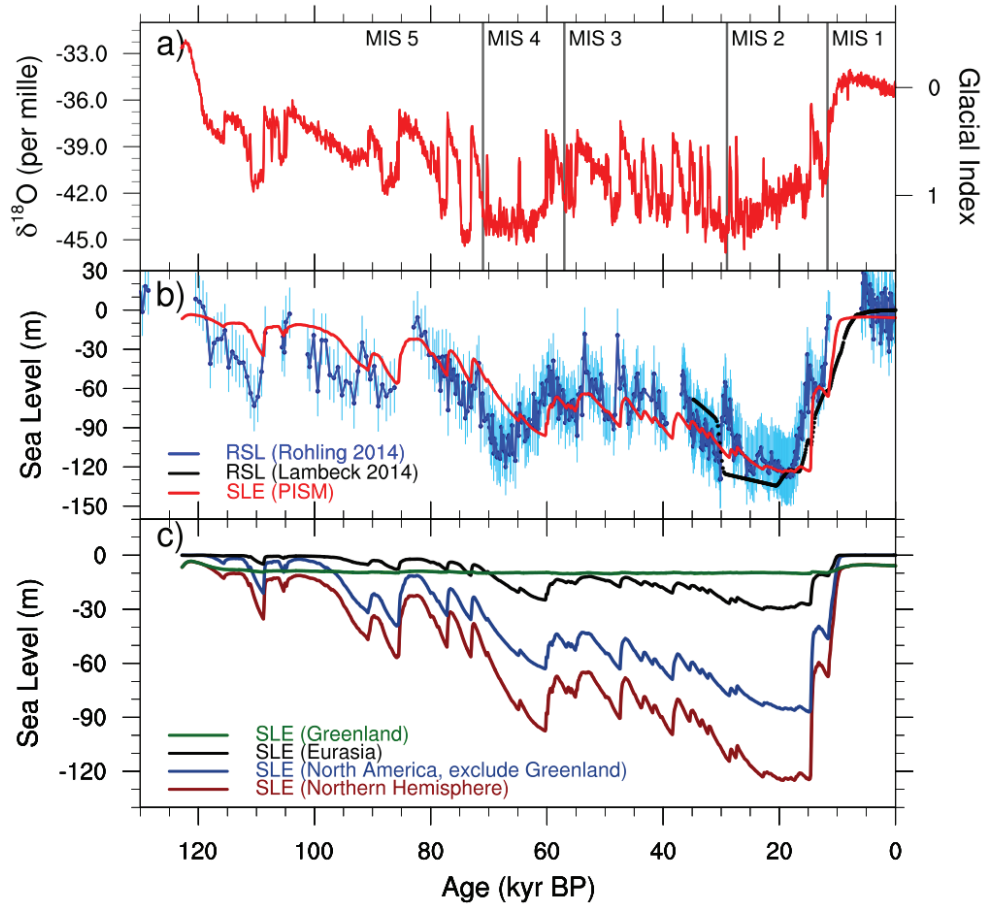


Figure 3.1: (a) The NGRIP ice core $\delta^{18}\text{O}$ record (Andersen et al., 2004) and the corresponding value of the glacial index. (b) The reconstructed relative sea level change from Rohling et al. (2014, dark blue line) with 1σ error bars (light blue), Lambeck et al. (2014, black line) and the modelled sea level equivalent (SLE) of the Northern Hemisphere ice sheets (red) using COSMOS-AWI. The correlation coefficient between SLE (PISM) and RSL (Rohling 2014) is 0.865. (c) Separated sea level equivalent (SLE) of Greenland Ice Sheet (green), Eurasian ice sheets (black), North American ice sheets (blue) and Northern Hemisphere ice sheets (red) through the last glacial cycle.

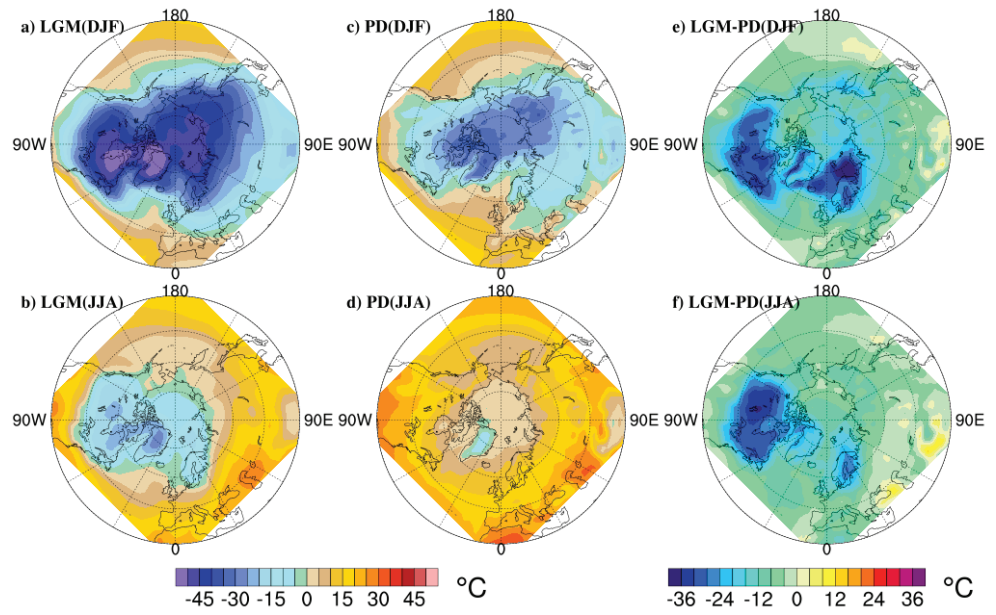


Figure 3.2: Winter (DJF) and summer (JJA) surface air temperature for Last Glacial Maximum (LGM, a-b) from COSMOS-AWI (Zhang et al., 2013) and Present Day (PD, c-d) from NCEP Reanalysis data (Kalnay et al., 1996), and the difference between LGM and PD surface air temperature (LGM minus PD, e-f).

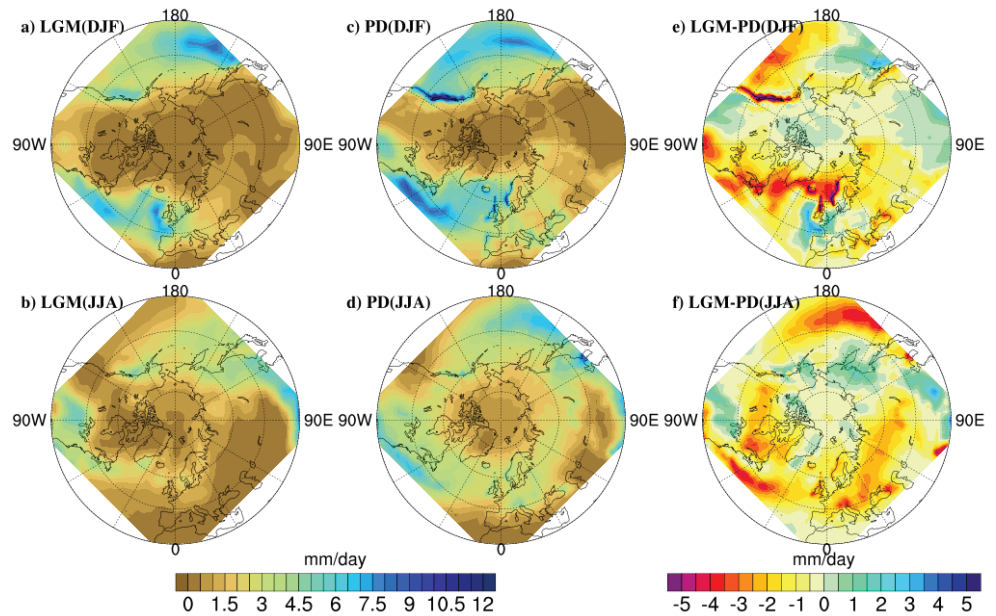


Figure 3.3: Same as Fig. 3.2, but for precipitation. The present day precipitation is from GPCP precipitation products (Adler et al., 2003).

with reconstructions of sea level and ice sheet extent. The results forced with reanalysis data as present-day condition are similar as the one with PI COSMOS output. Therefore we mainly focus on the simulation forced with the reanalysis data in the following text.

3.3.1 *The Temporal Evolution of Ice Sheet Volume*

Figure 3.1b shows a comparison between simulated ice volume (in units of eustatic Sea Level Equivalent (SLE), red line) and relative sea level reconstructions (Lambeck et al., 2014; Rohling et al., 2014). Generally, the modelled ice volume change resembles a sawtooth curve with slow ice sheet buildup and fast retreat. The total ice volume decreases slightly in response to higher temperature before 121 kyr BP. After that, the ice volume increases with several fluctuations, for instance, at 109 kyr BP, 91 kyr BP and 86 kyr BP. In response to the cold signals in NGRIP during MIS 4 (80 - 60 kyr BP), the ice volume increases significantly by up to 90 m SLE. These features agree well with the reconstructed curve, but there are some differences. During MIS 4, the modelled local sea level minimum happens around 7 kyr later than the relative sea level curve. The starting times of the modelled ice sheet retreat are later than the reconstruction, indicating that the modelled ice sheet responses are less sensitive. One potential reason could be that a cryo-hydrologic warming to the ice which can cause nonlinear ice flow response is not currently captured by PISM (Colgan et al., 2015). A mismatch of the age models of the NGRIP data and the Rohling sea level curve can also cause this inconsistency. The amplitude of the SLE variability is not as large as the reconstructed time series, especially during the glacial inception. This is probably because we use constant PDD parameters for calculating the surface ablation, which might cause a partial mismatch between the simulated results and the reconstructed sea level due to different insolation contributions.

Between 60 kyr BP and 25 kyr BP, the simulated SLE fluctuated with higher frequency in response to the high amplitude millennial scale variability in the ice core, which are called DO events. The regions that mainly contributed to the ice sheet variations were around the ice sheet margins (not shown). The total ice sheet volume reached its maximum (around 120 m SLE) at around 24 kyr BP, and remained near this value until 15 kyr BP. If a sea level contribution of 10 m from Antarctica Ice Sheets is included (Whitehouse et al., 2012), the maximum SLE value is comparable with the far-field sea level records (134 m; Austermann et al., 2013; Lambeck et al., 2014). Afterwards, it retreated rapidly to half of its maximum value by 13.5 kyr BP. A slight increase in ice volume happened at 11.7 kyr BP, corresponding with the Younger Dryas. The total ice volume continued decreasing until 9 kyr BP, then became stable with 6-7 m SLE remaining. The final timing of deglaciation is

earlier than the geological constraints (Cuzzone et al., 2016; Lambeck et al., 2014; Ullman et al., 2016). There are large uncertainties in the reconstructed sea level during the Holocene (Rohling et al., 2014), while the variability of the simulated ice volume is insignificant.

The individual sea level contributions in the Greenland, Eurasian and North American (excluding Greenland) ice sheets varied between different marine isotope stages (Fig. 3.1c). The Greenland Ice Sheet (green) was the main contributor to sea level fall during MIS 5e, and after that remained relatively stable with 10 m SLE until the deglaciation (around 14 kyr BP). North American ice sheets (blue) started to build up from MIS 5d, while the Eurasian ice sheets (black) development was restricted before MIS 4. The amplitude of ice sheet volume change response to DO events for Eurasian ice sheets was smaller than North American ice sheets. The maximum ice volume of Eurasian ice sheets was during MIS 2 with 30 m, and around 80 m for North American ice sheets. At 15 kyr BP, North American ice sheets were slightly larger than at 20 kyr BP, while the Eurasian ice sheets were smaller than before. The SLE increase during the Younger Dryas was more than 6 m, mainly derived from the North American ice sheets in our simulation. However, far-field sea level evidences show that sea-level rise slowed down during the Younger Dryas (Bard et al., 2010), with extensive end moraines found for the Eurasian ice sheets (Cuzzone et al., 2016). The timing of final deglaciation for the Eurasian ice sheets shows agreement with previous studies (9.1 kyr BP; Cuzzone et al., 2016), while it is too early for the North American ice sheets (around 7 kyr BP; Ullman et al., 2016).

3.3.2 *Spatial Distribution of Ice Sheets*

Snapshots of ice sheet thickness at different key periods are shown in Fig. 3.4. Consistent with the SLE change (Fig. 3.1b), the extent of the Greenland Ice Sheet shrank slightly during MIS 5e. As the climate became colder, a thin ice sheet started to build up along the northeast coast of North America, in the region of Baffin Island and the Labrador-Quebec sector. It advanced westward into the Interior Plains during MIS 5d, when the Cordilleran Ice Sheet and the Scandinavian Ice Sheet also started to build up as low profile, thin ice sheets. During MIS 5c, the ice sheets retreated again with ice remaining on Baffin Island and Ellesmere Island. Compared to MIS 5d, the MIS 5b ice sheets were much thicker in Baffin Island and the Labrador-Quebec sector. According to Kleman et al. (2010), an ice divide close to the Labrador coast in the Quebec sector existed during MIS 5b or 5d, and may indicate the location of glacial inception for North American ice sheets started around the northeast coast. The Cordilleran Ice Sheet also grew notably during MIS 5b. Ice sheet retreat happened during MIS 5a, with

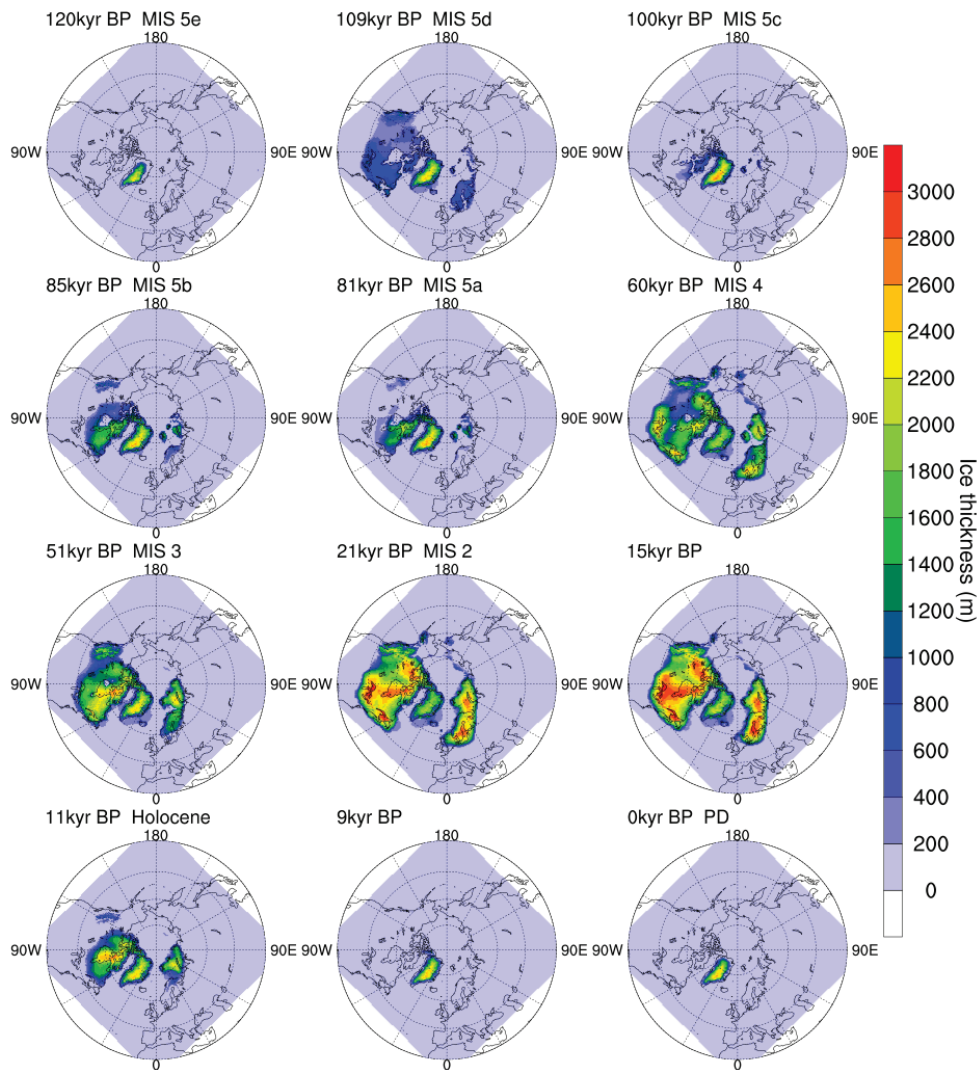


Figure 3.4: Modelled ice thickness (m) evolution through the last glacial cycle at different climate stages. The simulation is forced by the climatology monthly mean surface air temperature and precipitation from COSMOS-AWI.

ice remaining on the northeast coast of North America and ice caps in the Barents-Kara area.

During *MIS 4*, the ice sheets extended far further south in both North America and Eurasia. For North America, the ice sheets built up in Labrador-Quebec, Keewatin, the Great Lakes and Cordilleran areas separately, leaving the Hudson Bay Lowlands, the western part of Hudson Bay and south of Keewatin almost ice free. Large ice sheets grew at the southern margin of Laurentide ice sheet prior to the *LGM* (Carlson et al., 2018; Wood et al., 2010), which our simulations are able to reproduce. For Eurasia, the Barents-Kara Ice Sheet, the Scandinavian Ice Sheet and the British-Irish Ice Sheet built up, while the Scandinavian Ice Sheet and Barents-Kara Ice Sheet separated. During *MIS 3*, the total ice volume increased gradually, accompanied with

fluctuations due to the DO events. This is inconsistent with recent studies showing that the Laurentide Ice Sheet advanced rapidly towards the LGM (Carlson et al., 2018; Dalton et al., 2016). During this period, the Scandinavian Ice Sheet and Barents-Kara Ice Sheet merged, the western Laurentide Ice Sheet and eastern Laurentide Ice Sheet merged, and the Cordilleran Ice Sheet and the Laurentide Ice Sheet merged. At around 21 kyr BP, the Northern Hemisphere ice sheets reached their maximum extent.

The ice domes in the Keewatin and Labrador sectors were probably dynamically independent for most of the time before the LGM. The Labrador dome expanded southward earlier than the Keewatin sector at around MIS 4. For Eurasian ice sheets, geological evidence indicates that the Barents-Kara Ice Sheet extended further east to the Taimyr Peninsula prior to the LGM, and the Barents-Kara Ice Sheet became smaller while the Scandinavian Ice Sheet became bigger during each successive glaciation (Svendsen et al., 2004). In other words, the Eurasian ice sheets advanced progressively further southwest from MIS 4 to the LGM. In our simulation, the Barents-Kara Ice Sheet did not build up prior to MIS 4 and there was no change in ice sheet extent through time. This is likely because the large-scale North American ice sheet build-up changed the atmospheric stationary waves. The modified atmospheric circulation favored the growth of southwestern Eurasian ice sheets (Liakka et al., 2012; Löfverström et al., 2014; Roe and Lindzen, 2001). Since the index method cannot account for differences in atmospheric circulation due to different ice sheet configurations, it is unsurprising that there is this mismatch.

The ice sheet configuration during the LGM is relatively well known. There were three major domes of Laurentide Ice Sheet: Labrador, Keewatin and Foxe (Bryson et al., 1969; Dyke and Prest, 1987; Margold et al., 2015; Prest, 1968), which can also be observed in our simulation. The North American ice sheets extended southward to 40 °N with ice sheet thickness up to 3000 m. The interior of Alaska was ice free during the LGM. For Eurasia, the ice sheet covered the Barents-Kara Sea, the Scandinavia and extended southwest to the British-Irish area.

Most of the Northern Hemisphere ice sheets started to retreat at around 15 kyr BP, while the British-Irish Ice sheet retreated earlier at 16.5 kyr BP. By around 13 kyr BP, the total ice volume decreased to half of its maximum volume (Fig. 3.1b), with ice covered regions persisting on Hudson Bay and the Canadian Shield, the center of Cordilleran region, most of Barents-Kara Sea and part of Scandinavia. By 9 kyr BP, all the ice sheets completely retreated except the Greenland Ice Sheet, which is slightly too early for the Laurentide Ice Sheet (Cuzzone et al., 2016; Dyke, 2004; Lambeck et al., 2014; Ullman et al., 2016).

For the simulated conditions at present day (0 kyr BP), the Greenland ice sheet volume is around $2.4 \times 10^{15} \text{ m}^3$ (5.8 m SLE), with a maximum thickness of 2694 m and an ice covered area of 1.9×10^{12}

m². The magnitude is comparable with the previous studies (e.g., Fettweis, 2007; Mote, 2003).

3.4 DISCUSSIONS

3.4.1 *The Glacial Index Method*

In the previous section, we compared the simulated ice sheets to geological evidence. Consistent with previous studies that used the glacial index method (e.g. Charbit et al., 2007; Marshall et al., 2002; Tarasov and Peltier, 2004), we confirm that the method is capable of capturing the first order pattern of the North Hemisphere ice sheet evolution. Furthermore, more features (for example, the glacial inception pattern and the ice sheet configuration at the LGM) are captured with forcing from COSMOS-AWI than in previous studies (e.g. Charbit et al., 2007; Marshall et al., 2002).

However, several aspects need to be considered carefully when using this method. First of all, there is a circularity between the ice sheet simulation and the GCM simulation. The GCM output used as climate forcing is based on a reconstructed ice sheet configuration with fixed ice sheet topography and surface albedo (Abe-Ouchi et al., 2015). Due to higher elevation and higher albedo over the ice surface, the surface temperature at the LGM is much lower over the prescribed ice sheet regions than that of bare-land regions (Fig. 3.2). The strong temperature gradient at the ice sheet margins restricted the southern extent of the simulated ice sheets. More precipitation is simulated in the southern margins of the ice sheets at the LGM than PD (Fig. 3.3). This precipitation bias resulted in more ice buildup around the southern margins of the ice sheets.

As we mentioned before, the feedback between the ice sheet, atmosphere and ocean cannot be inferred with this method. Recent studies found that large ice sheets can significantly modify the stationary waves or jet streams, and the atmospheric response can reorganize the structure of the ice sheets (Liakka et al., 2012; Löfverström et al., 2014, 2015; Ullman et al., 2014). Also, the final deglaciation of the modelled ice sheets is too early compared to the geological evidence, especially in North America (Cuzzone et al., 2016; Dyke, 2004; Hughes et al., 2016; Rohling et al., 2014; Ullman et al., 2016). This indicates that these regions might still be cold during that time, while the linear interpolation based on the Greenland ice core record may not have the signal. The fluctuations in the Greenland record may reflect local climate changes that are on orbital and millennial time scales, which may not be global in nature (Banderas et al., 2018; Seguinot et al., 2016). Temperature and isotope signals imprinted in Greenland due to regional and global climate conditions change may also be different (Buizert et al., 2014; Pausata and Löfverström, 2015).

To adequately capture the feedback between ice sheets and the atmosphere, it is necessary to use *GCMs* bidirectionally coupled to ice sheet models. An approach of coupling ice sheet models to *EMICs* (Claussen et al., 2002) has been used (e.g., Bauer and Ganopolski, 2017; Charbit et al., 2005; Fyke et al., 2011; Ganopolski et al., 2010). However, the spatial grids from *EMICs* are very coarse. Despite the computational expensive for long-duration simulations, coupling to a sophisticated *GCM* could be an effective way for solving orbital time scale problems with higher resolution and more sophisticated atmospheric dynamics (Ziemen et al., 2019). Combined with Regional Climate Models (RCMs), *GCM* simulations can be enhanced to solve regional conditions over the ice sheet margins (Pollard, 2010). In this case, atmospheric forcing that is taken from *GCMs* needs to be better constrained.

3.4.2 *PDD and Surface Energy Balance*

The semi-empirical *PDD* method is applied for computing the surface ablation. It uses only the surface temperature for computing melt. The *PDD* scaling parameters are obtained with measurements from modern glacier conditions, while different glaciers or paleo scenarios might give different values. It may underestimate the influence of shortwave radiation for the surface melt, which has been considered as a major driver for glacial cycles (Bauer and Ganopolski, 2017; Berg et al., 2011; Robinson and Goelzer, 2014; Ullman et al., 2015). In order to assess the validity of the *PDD* method in our stand-alone simulations, we compared the surface melt simulated by PISM's *PDD* model to the melt computed by energy balance model of COSMOS, which uses a much more sophisticated energy balance scheme but at lower resolution (T31) and with fixed ice sheet configuration (Fig. 3.5).

For consistency, we also compared the results with COSMOS *PI* and *LGM* output as climate forcing. The results show good agreements between *PDD*-based approach and energy balance based approach. At the *LGM*, all the results show similar melt pattern around the margins of the North American and Eurasian ice sheets. For the present day and the Eemian, the snow melt extent in the North American and Asian continents in COSMOS is broader. For the Greenland ice sheet, the surface melt patterns still match well, especially in the southernmost region. The simulation with reanalysis products show more melt around Greenland, which is probably because the observational data contain the warming signal of the previous century. Previous studies argued that the Laurentide Ice Sheet would never deglaciate if the *PDD* approach is used (Bauer and Ganopolski, 2017; Ullman et al., 2015). This is why we tuned the precipitation to balance the extra total mass gain. In our simulation, the deglaciation is driven by the index method going towards the Present day state. For the current

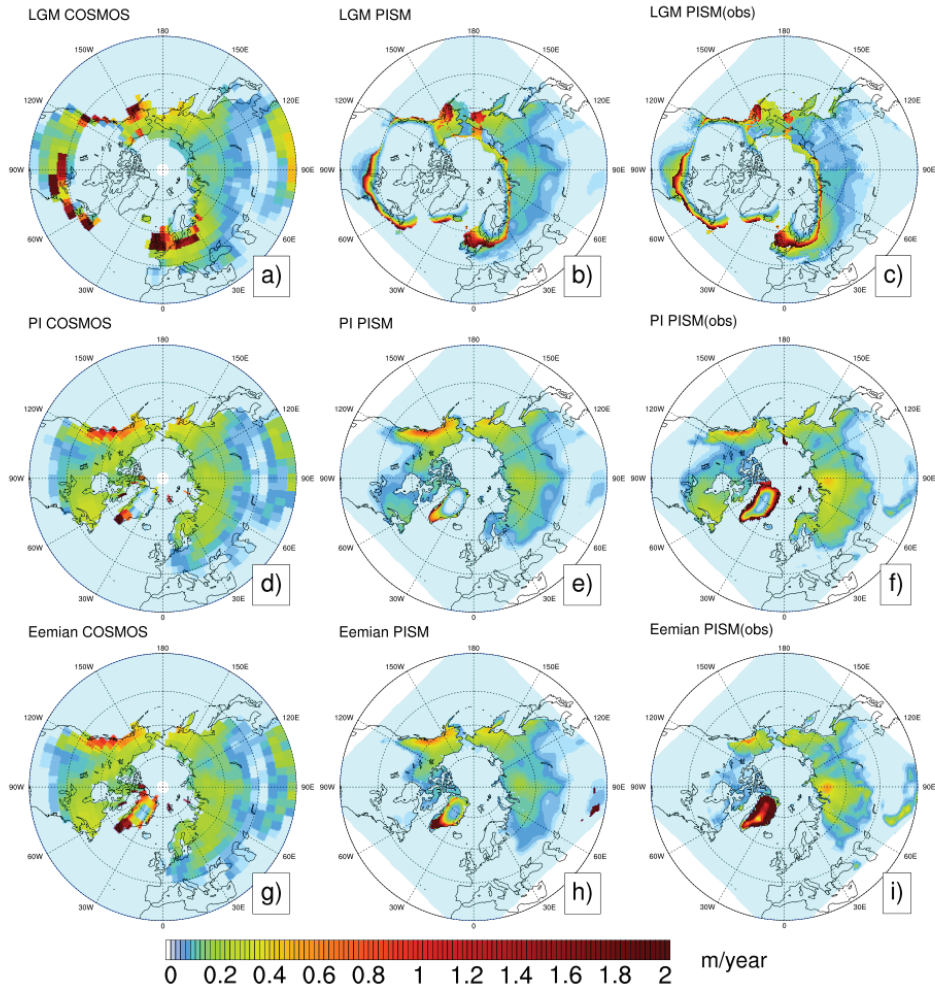


Figure 3.5: Comparison of surface melt between energy balance-based scheme from COSMOS (a, d, g) and PDD-based scheme from PISM (b, e, h or c, f, i) at the LGM, present day (PD) and Eemian (Units: m/year). The right panel plots are from the reference simulation (COSMOS-AWI) with reanalysis products at PD and COSMOS GCM at the LGM as climate forcing. The middle panel plots are with COSMOS GCM at preindustrial and the LGM.

study, the PDD-based scheme may still be a suitable alternative to computationally expensive surface energy balance models.

3.4.3 *Potential for Further Investigation*

A future step in investigating ice sheet sensitivity to climate forcing would be the incorporation of more elaborated schemes than PDD (e.g. Krebs-Kanzow et al., 2018a) where the surface energy balance is taken more explicitly into account. Recent work has also highlighted the role of ocean forcing in driving glacial ice sheet variability (Bassis et al., 2017). In our study, we fixed the ocean forcing and did not sample this potential source of climate-driven ice sheet change. Variability of the ice-substrate interface could also be included in future work (Gowan et al., 2019).

3.5 CONCLUSIONS

We simulated the Northern Hemisphere ice sheets through the last glacial cycle using the glacial index method based on the NGRIP ice core. Consistent with previous studies, we show that this method is capable of capturing the main features of the Northern Hemisphere ice sheet evolution during the last glacial cycle but not all of them. During glacial inception, the ice sheets first built up along the coast of the Quebec-Labrador sector. The growth of the eastern Laurentide Ice Sheet was earlier than the western Laurentide Ice Sheet during the build-up stage (Kleman et al., 2010). For the LGM, the simulated ice extent resembles the geological reconstruction quite well, with the ice sheet extent extending southward to 40 °N, and maximum ice thicknesses up to 3000 m, an ice free Alaska region and a British-Irish Ice sheet (Dyke, 2004; Hughes et al., 2016). The Northern Hemisphere ice sheets contribute about 120 m SLE, with the North American ice sheets contributing about 80 m, Eurasian ice sheets 30 m, and Greenland ice sheet 10 m at the LGM. A multi-domed Laurentide Ice Sheet was observed in our simulation, consistent with observations (Bryson et al., 1969; Dyke and Prest, 1987; Prest, 1968).

Several concerns need to be considered carefully when using this method. The circularity between the ice sheet simulation and the GCM simulation can significantly influence the southern margins of the simulated ice sheets. The feedbacks between the atmosphere and the ice sheet cannot be inferred with this method. Even with these caveats, the glacial index method is an efficient way for testing the sensitivity of the ice sheets to climate forcing. For future studies, we plan to use an alternative ablation scheme to PDD, surface energy balance, for checking the influence of surface ablation.

EFFECTS OF MODEL UNCERTAINTY ON NORTHERN HEMISPHERE ICE SHEET EVOLUTION

4.1 INTRODUCTION

Using output from General Circulation Model (GCM) intercomparison projects, the sensitivity of ice sheets to the forcing has been investigated in earlier studies (Charbit et al., 2007; Dolan et al., 2015; Fyke et al., 2014; Pollard, 2000; Yan et al., 2014). Pollard (2000) found considerable scatter of surface mass budgets for the Northern Hemisphere ice sheets among the atmosphere-only models from the first generation of The Paleoclimate Modelling Intercomparison Project (PMIP). Same case is also shown in the simulated ice sheets (Charbit et al., 2007). The simulated Greenland ice sheet during a warm climate has also been found to be highly dependent on the climate forcing (Dolan et al., 2015; Fyke et al., 2014; Yan et al., 2014).

PMIP3 is the third phase of the paleoevaluation project PMIP to compare different atmosphere-ocean coupled GCMs (Braconnot et al., 2012). In our study, we used PMIP3 output to test the sensitivity of atmospheric effects on ice sheet evolution during the last glacial cycle. Based on the experiments from Chapter 3, we investigated the uncertainties linked to the atmospheric forcing using different models. For GCMs, although forced with the same boundary conditions, the simulated climate is model dependent, and therefore the modelled ice sheet evolution may also be different. The ice sheet configurations used for the PMIP3 model simulations, as well as the other boundary conditions are consistent among all the simulations.

4.2 EXPERIMENT DESIGN

Climates modelled by different GCMs vary between each other and contain model deficiencies. Using the same parameters from the initial experiment from COSMOS-AWI, we run the same simulation using the other PMIP3 ensemble members (Braconnot et al., 2012; Meinshausen et al., 2011). For present day conditions, we first use the reanalysis products (as described in Chapter 3) to make sure all the experiments have consistent present-day conditions. We name this set of experiments "PMIP3-PDObs". Further discussion regarding the choice of reanalysis products or GCM preindustrial (PI) output is given in Sect. 4.4. In total there are nine PMIP3 models available online (Table 2.3) with monthly climatology data for surface air temperature and precipitation as input. More details are archived in Sect. 2.2.3.

4.3 RESULTS

Figure 4.1a shows the *SLE* time series from experiment PMIP3-PDobs. Most models succeeded in reproducing the observed sea level fall (100 m to 150 m) at the *LGM*, except CNRM-CM5 and MRI-CGCM3 (16 m and 49 m respectively). The total ice volume in GISS-E2-R is relatively large during cold stages, and smaller during warm stages, compared to the other models. The root-mean-square deviation (*RMSD*) relative to the reference simulation for the *SLE* are calculated in Fig. 4.2 (black circles). The models that are most different from our reference model are CNRM-CM5 and MRI-CGCM3 (*RMSD* values are 48 m and 36 m respectively). The other models are more consistent with each other, with a *RMSD* less than 12 m.

The models exhibit large differences at the *LGM*, both in ice sheet thickness and extent (Fig. 4.3). Consistent with the *SLE* time series, the ice sheets from CNRM-CM5 are small in extent, with ice sheets in the western coast of North America, Keewatin region, Labrador, southern Greenland, and the Scandinavia Mountains. MRI-CGCM3 shows similar results with more ice covering Hudson Bay, Greenland and Barents-Kara Sea. Compared with the results from COSMOS-AWI, there is less ice in North America in GISS-E2-R. Instead, there is ice build up in Siberia, where there is no evidence of an *LGM* Ice Sheet (Niessen et al., 2013, Fig. 4.1, green line). For the other models, the general patterns are similar to the COSMOS-AWI model, except for CCSM4 and FGOALS-g2, which have ice sheet growth on the East Siberian Sea, Laptev Sea and Chukchi Sea.

In order to investigate why the ice sheets have such a diverse range of extents, when the only difference is the atmospheric forcing, we compared the surface air temperature and precipitation. We found that the ice sheet extent is strongly related to the summer surface air temperature. Figure 4.4 shows the Probability Distribution Functions of the surface air temperature and precipitation ice sheet margins and Northern Hemisphere during different seasons. The ice sheet margins are generally located where summer temperatures are confined to between -5 and 5 °C. The spatial distribution also shows a similar pattern (Fig. 4.5). The ice sheet extent pattern during the *LGM* resembles the summer surface air temperature pattern, where the ice sheet margin is similar to the -5 °C isothermal lines. For precipitation, no clear relationship emerges.

To study the individual roles of temperature and precipitation, we conducted two additional sets of experiments. One experiment keeps the temperature the same as COSMOS-AWI, while using the precipitation from the PMIP3 models (PMIP3-fixCOSMOSTemp). The other experiment is the opposite (PMIP3-fixCOSMOSPrecip). When forced with the same temperature, the simulated *SLE* evolution has closer agreement between the simulations (Fig. 4.6a) with *RMSD* values

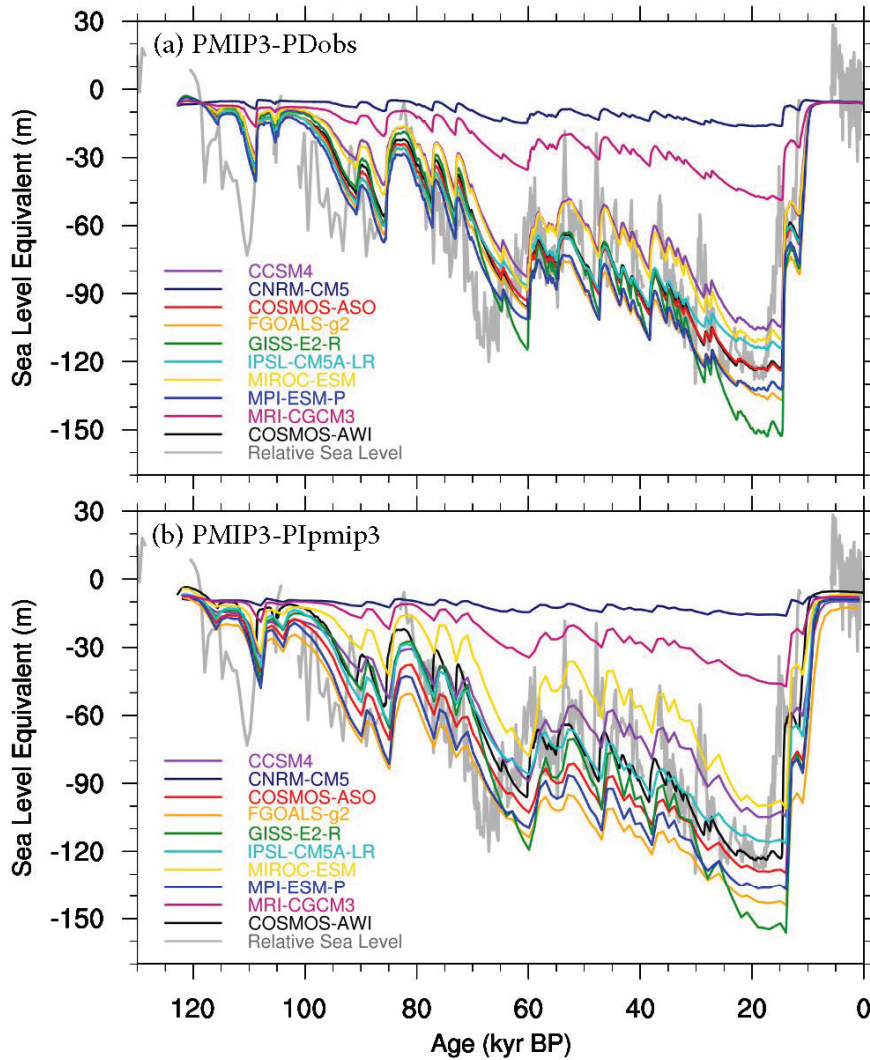


Figure 4.1: Modelled sea level equivalent (SLE) of Northern Hemisphere ice sheets change through the last glacial cycle using the output of PMIP₃ models. (a) Experiment PMIP₃-PDobs, with climate forcing of present day conditions from reanalysis products (1981-2010) and the LGM conditions from PMIP₃ GCM output. (b) Experiment PMIP₃-PIpmip₃, with climate forcing of present day conditions from PMIP₃ preindustrial (PI) output and LGM conditions from PMIP₃ GCM output.

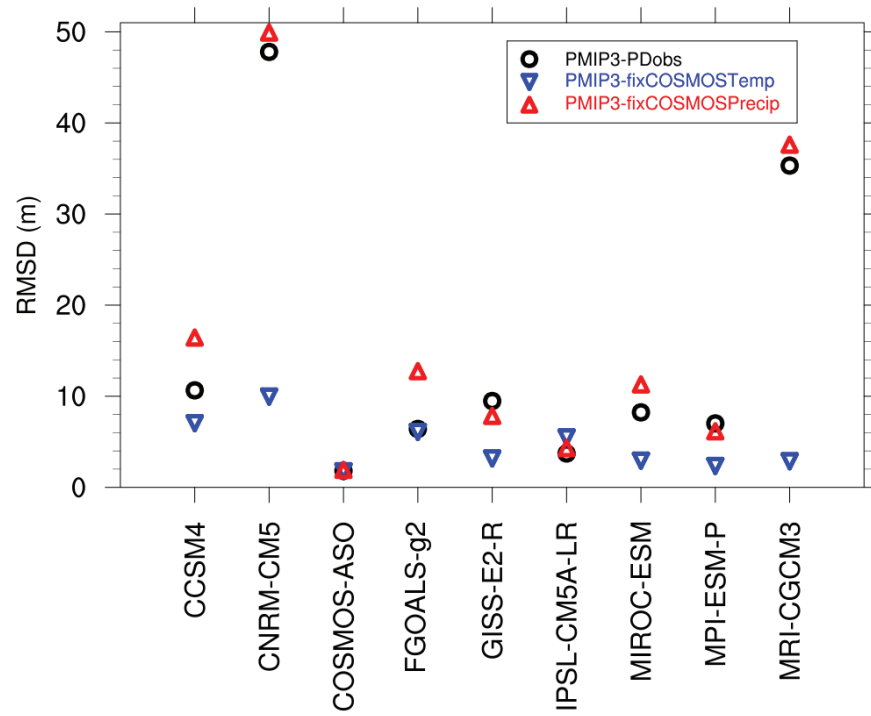


Figure 4.2: Root-mean-square deviations of SLE when compared to the reference simulation (COSMOS-AWI) for different PMIP₃ models. Black circles are from experiment PMIP₃-PDobs, blue triangles are from experiment PMIP₃-fixCOSMOSTemp, red triangles are from experiment PMIP₃-fixCOSMOSPrecip.

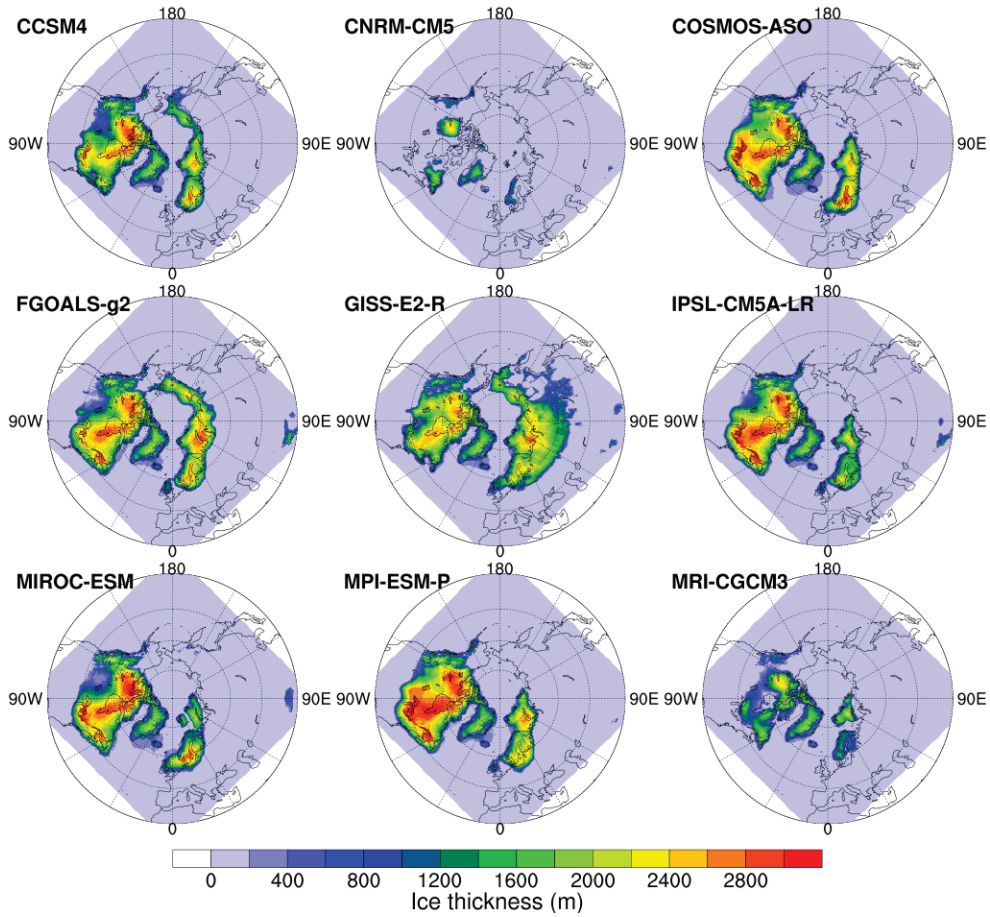


Figure 4.3: Modelled ice thickness at the Last Glacial Maximum (LGM, 21 kyr BP) using the PMIP₃ model output from experiment PMIP₃-PDobs.

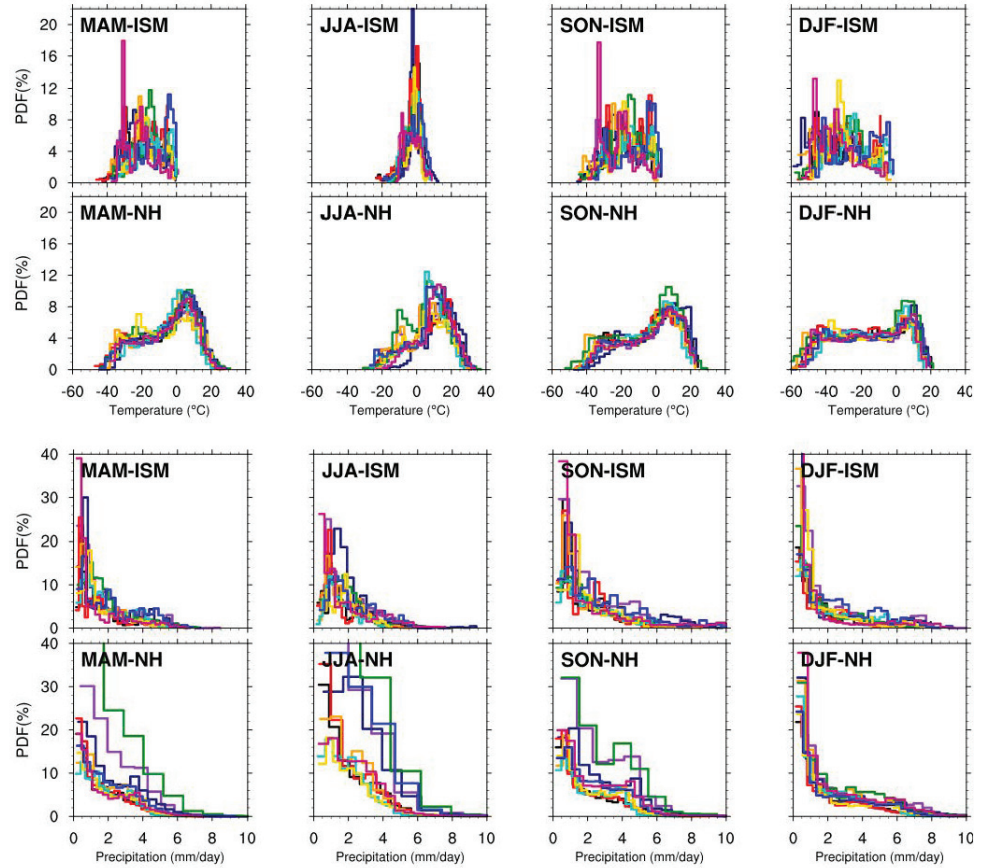


Figure 4.4: Probability Distribution Functions (PDF) of surface air temperature (upper two rows) and precipitation (lower two rows) over the ice sheet margins (ISM) and Northern Hemisphere (NH) for different seasons (MAM, JJA, SON, DJF) for different models. For the colors, we refer to Fig. 4.1.

less than 11 m (Fig. 4.2, blue triangles). The ice sheet extent at the LGM also shows more consistency between simulations (Fig. 4.7), but with quite different ice sheet thickness distribution, which is mainly caused by the differences in precipitation. The results from PMIP3-fixCOSMOPrecip are more similar as the experiments from PMIP3-PDobs (Fig. 4.6b, 4.8). The failure of ice sheet build up at the LGM, especially for CNRM-CM5 and MRI-CGCM3, are mainly a result of a warm temperature bias. This contributes to a larger variability compared with the PMIP3-PDobs simulations, with larger *RMSD* values in 6 out of 9 models (Fig. 4.2, red triangles).

4.4 DISCUSSIONS: THE ATMOSPHERIC FORCING FROM GCMS

As is shown in Sect. 4.3, the summer surface air temperature seems to be an important control on ice sheet extent. This is consistent with previous studies showing that summer ablation is more important

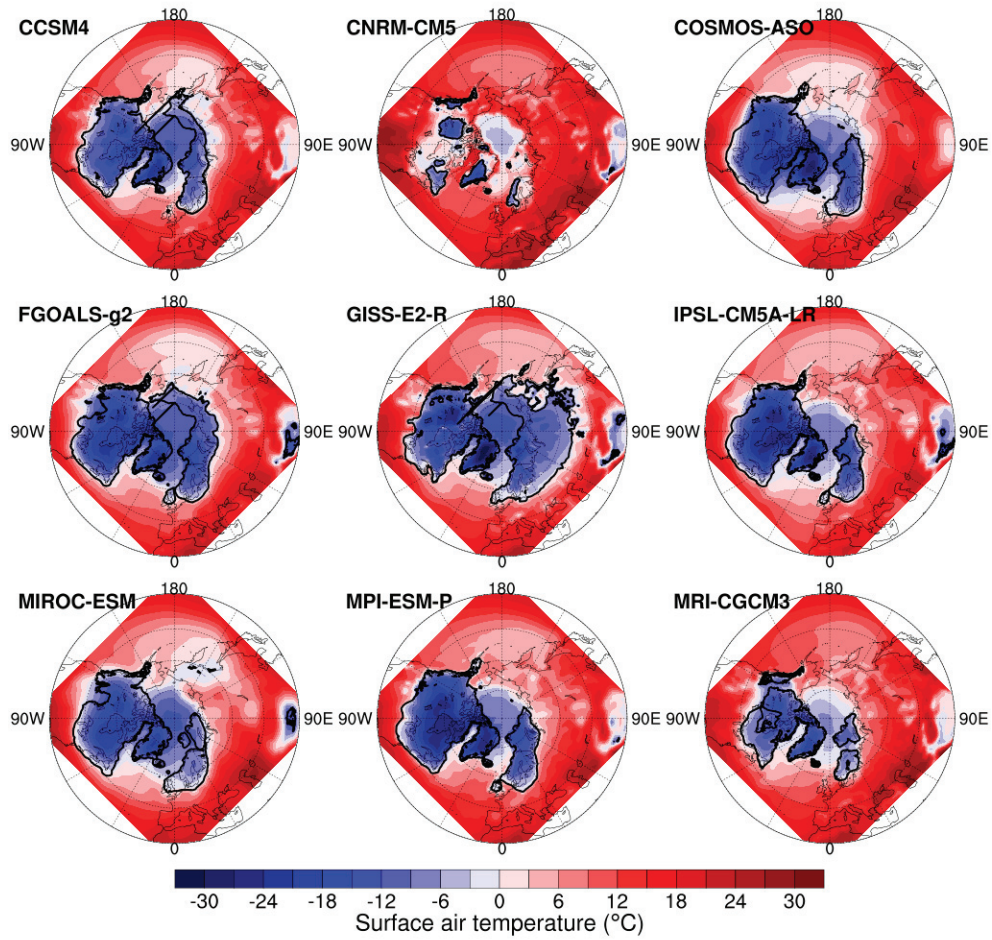


Figure 4.5: The surface air temperature at the Last Glacial Maximum (LGM) in summer (JJA) for different models that participated in PMIP₃ and the ice sheet margins at the LGM (black lines).

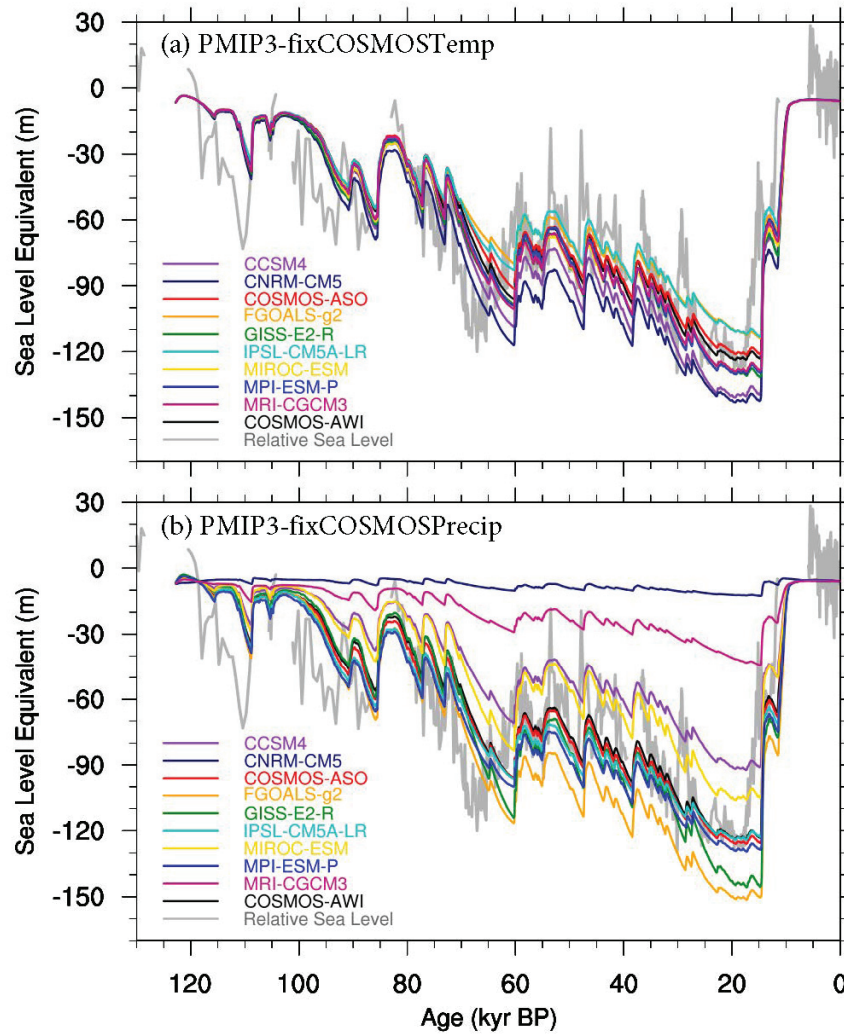


Figure 4.6: Modelled sea level equivalent (SLE) of Northern Hemisphere ice sheets change through the last glacial cycle using the PMIP3 model output. (a) PMIP3-fixCOSMOSTemp, with surface air temperature from COSMOS-AWI, precipitation from PMIP3 models. (b) PMIP3-fixCOSMOSPrecip, with precipitation from COSMOS-AWI, surface air temperature from PMIP3 models.

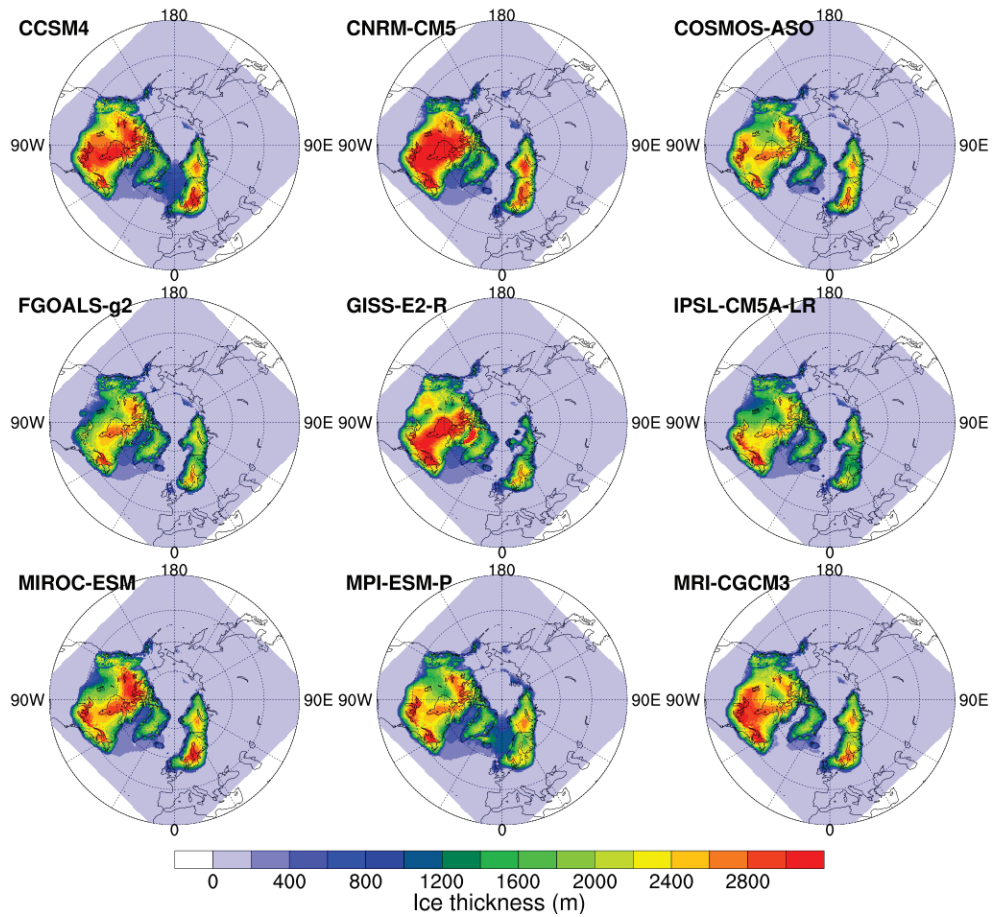


Figure 4.7: Modelled ice thickness at the Last Glacial Maximum (LGM, 21 kyr BP) from experiment PMIP3-fixCOSMOSTemp.

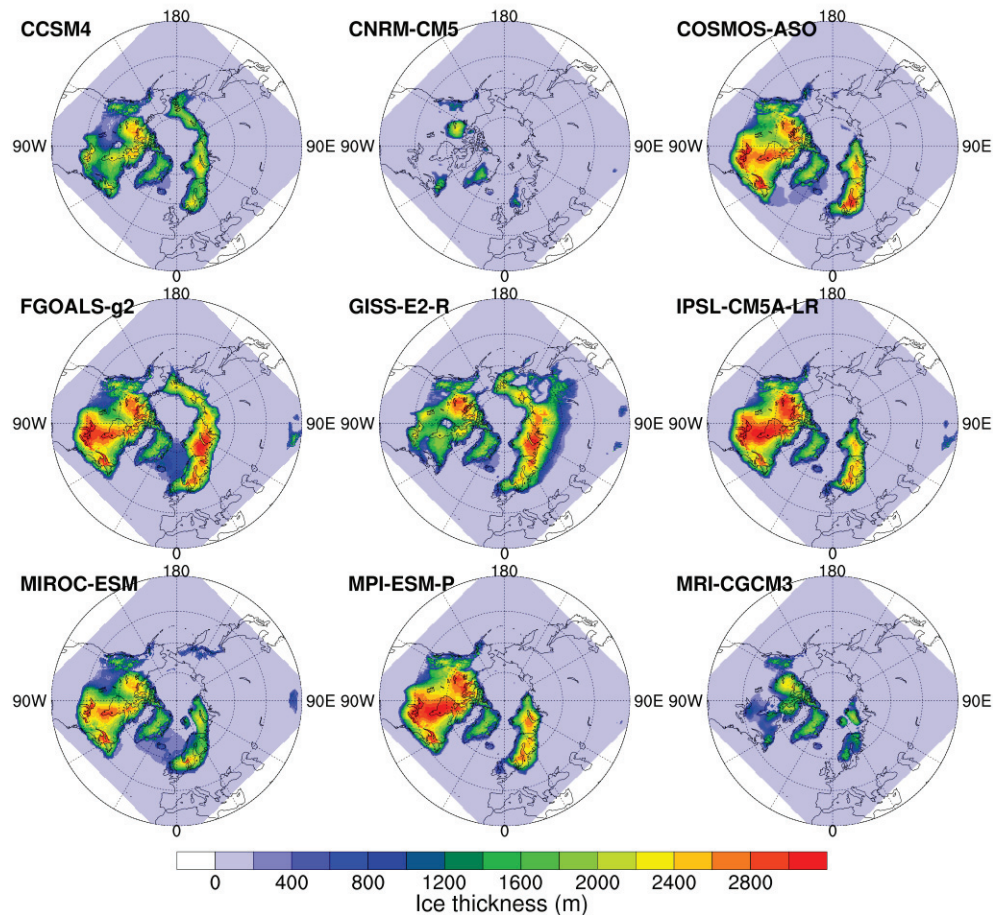


Figure 4.8: Same as Fig. 4.7, except that experiment from PMIP3-fixCOSMOSPrecip.

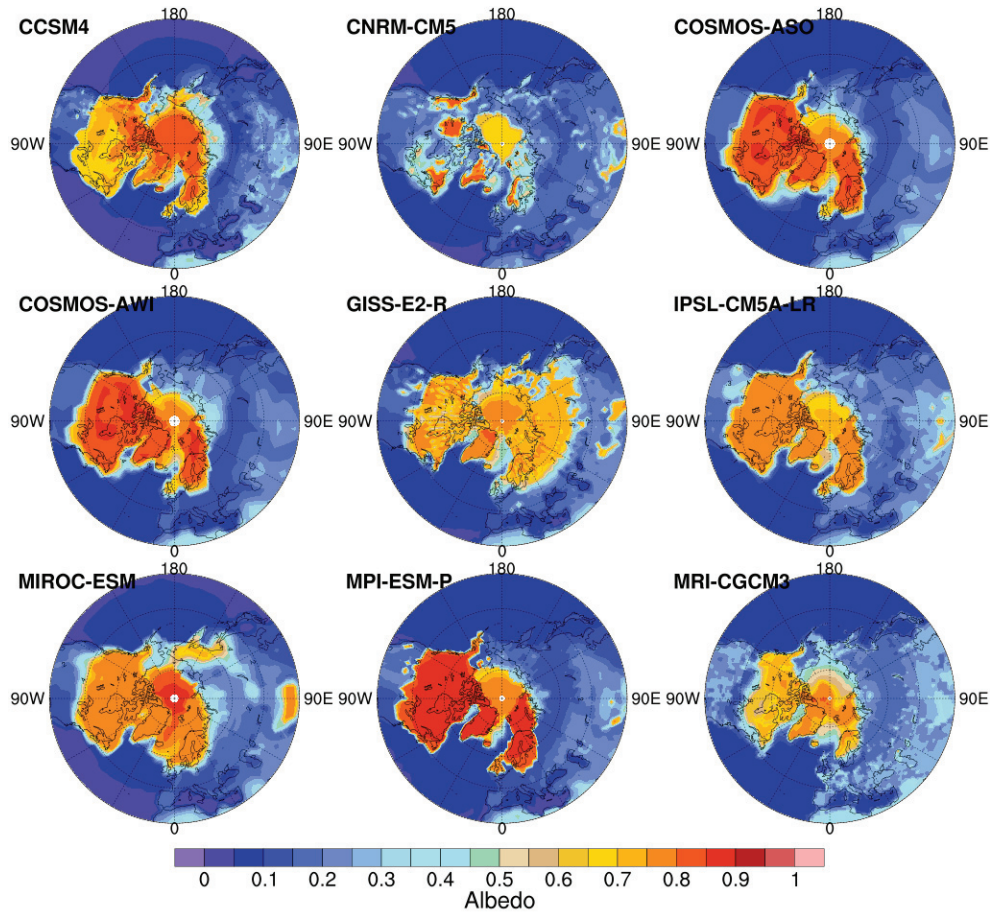


Figure 4.9: Surface albedo in summer from different models participating in PMIP3. The albedo is calculated as the ratio of surface upward shortwave radiation and surface downward shortwave radiation. (The shortwave upward radiation for FGOALS-g2 is not available from the PMIP3 data output online.)

than snow accumulation in the winter for the evolution of the ice sheets (e.g. Gallée et al., 1992). The differences in ablation among GCMs can considerably influence the resultant surface mass balance. The large variability in GCM directly translate into a large variability in simulated ice sheets. We speculate that the differences in simulated surface air temperature are the consequence of the different albedo schemes employed by the GCMs. By calculating the ratio of upwelling shortwave radiation and downwelling shortwave radiation at the surface, we obtain significant differences between the models (Fig. 4.9).

In winter and colder areas, accumulation is a more prominent process than ablation. From our simulations, a multi-domed pattern at the LGM can be observed in almost all of the model results (Fig. 4.3). According to the present day precipitation pattern (Fig. 3.3c-d),

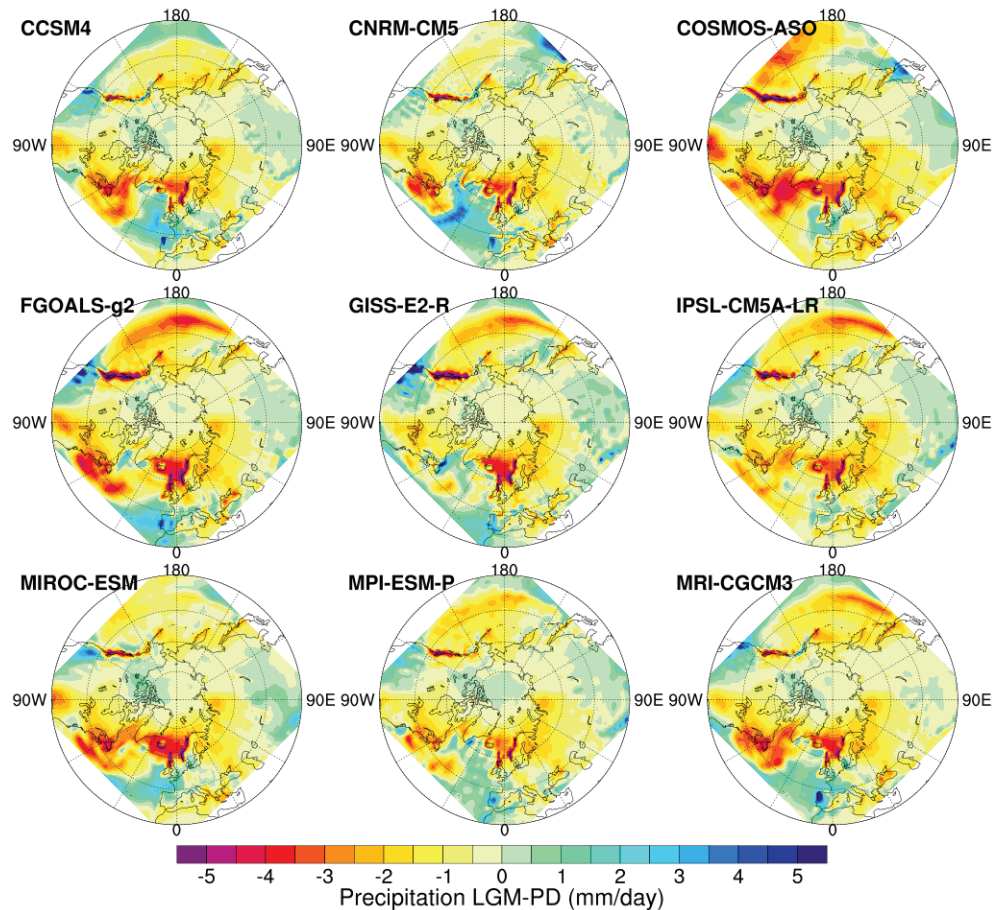


Figure 4.10: The Precipitation (Precip) difference between Last Glacial Maximum (LGM) and Present Day (PD) in winter (DJF) for different models that participated in PMIP₃ (LGM minus PD).

precipitation is large along the coast of North America and Europe, while the middle of the continents is relatively dry, especially in the Keewatin region. So how did ice sheet domes form in these regions? Investigating the temperature and precipitation patterns, we find that in all the models, there was more precipitation in winter in Keewatin at the LGM than present day (Fig. 4.10), which resulted in accumulation in that region. Also, as is shown in experiment PMIP₃-fixCOSMOSTemp, the difference of precipitation pattern could strongly result in a change of the ice sheet geometry.

In our PMIP₃ experiments, we prescribed the present day climate by using the reanalysis products from 1981-2010. The simulated ice sheets varied significantly even though we only changed the LGM climate. In order to make the model comparison more consistent, we replaced the reanalysis products with the modelled PMIP₃ preindustrial GCM output and ran the experiments again (PMIP₃-PIpmip₃).

Comparing the sea level equivalent time series (Fig. 4.1b) with the one from PMIP₃-PDobs (Fig. 4.1a), we find that the curves show a

similar pattern, but are more scattered. The differences in sea level equivalent for Greenland at present day can be up to 6 or 7 meters due to the different Preindustrial conditions in different models. The simulated ice thickness pattern at the LGM in PMIP3-PIpmip3 is almost the same as in PMIP3-PDobs (Fig. 4.11). The most distinct result is the one that used MIROC-ESM forcing, with a difference of more than 600 m in the central area of Laurentide Ice Sheet (Fig. 4.12). Comparing the summer (JJA) surface air temperature difference between the reanalysis products and the PMIP3-PI-GCM output, we find that the MIROC-ESM PI temperatures exhibit a large warm bias over the northern hemisphere continents (Fig. 4.13). This resulted in less ice sheet buildup than in the PMIP3-PDobs experiment. For the other models, the ice thickness difference is less than 600 m, with slightly thicker ice in Eurasia and most of northern North America except for Hudson Bay and Arctic Archipelago in the PMIP3-PIpmip3 experiments (Fig. 4.12). Comparing the corresponding summer temperature differences (Fig. 4.13), we find that the anomaly patterns also matched, with a warmer climate leading to a smaller ice volume and a colder climate resulting in a larger ice volume. For most of the PMIP3 models (COSMOS-ASO, FGOALS-g2, GISS-E2-R, IPSL-CM5A-LR, MPI-ESM-P, MRI-CGCM3), the GCM preindustrial conditions are generally colder than the reanalysis products, resulting in a larger ice sheets. This is probably because the reanalysis products are from a time period of 1981-2010, which contains the hottest years of the past century and the climate is perturbed by increased greenhouse gases.

4.5 CONCLUSIONS

We simulated Northern Hemisphere ice sheet evolution during the last glacial cycle using the output from PMIP3 GCMs. There is considerable scatter among the results, showing the sensitivity of glacial-interglacial Northern Hemisphere ice sheets to atmospheric forcing. The ice sheet extent is best explained by the summer surface air temperatures, showing the dominant role of surface ablation process. Precipitation related to ice sheet accumulation is a secondary control factor for modifying the ice sheet geometry.

We highlight that the ice sheet response to forcing from different climate models is strongly model dependent. Large scatter exists among the state-of-the-art GCMs. Additional constraints on climate output should be considered carefully for simulating glacial-interglacial Northern Hemisphere ice sheets.

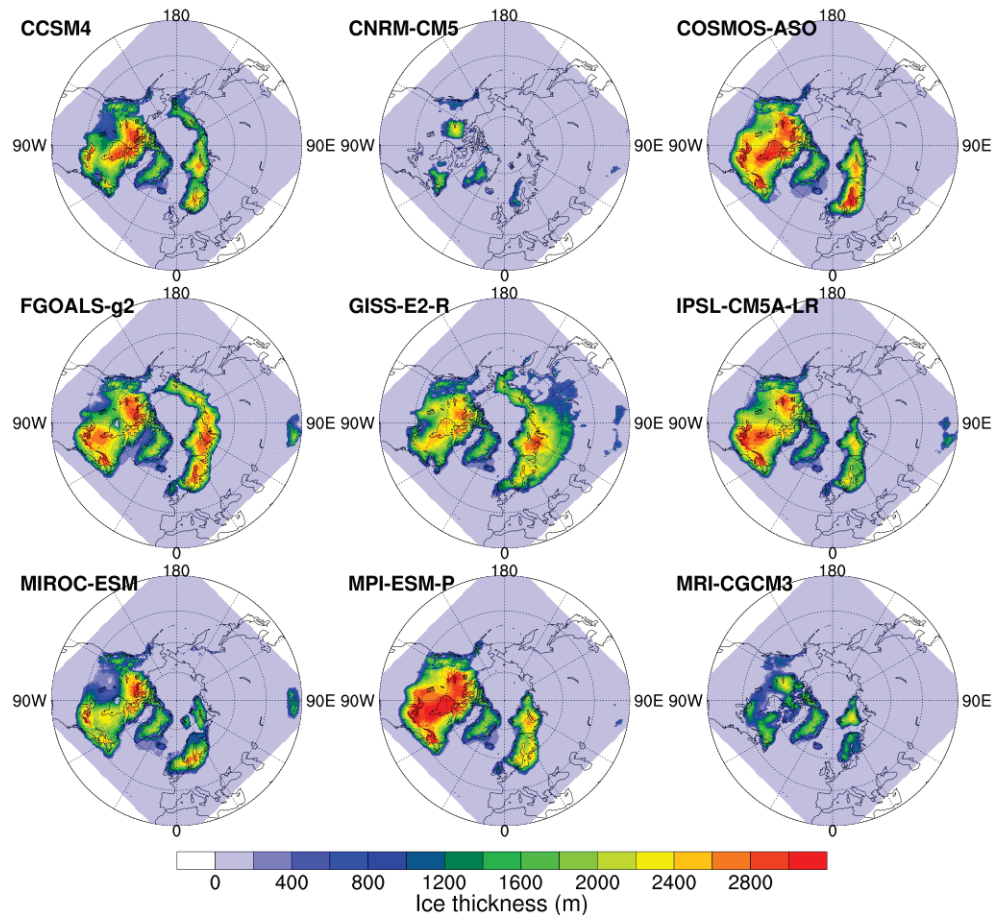


Figure 4.11: Same as Fig. 4.7, except that experiment from PMIP3-PIpmip3.

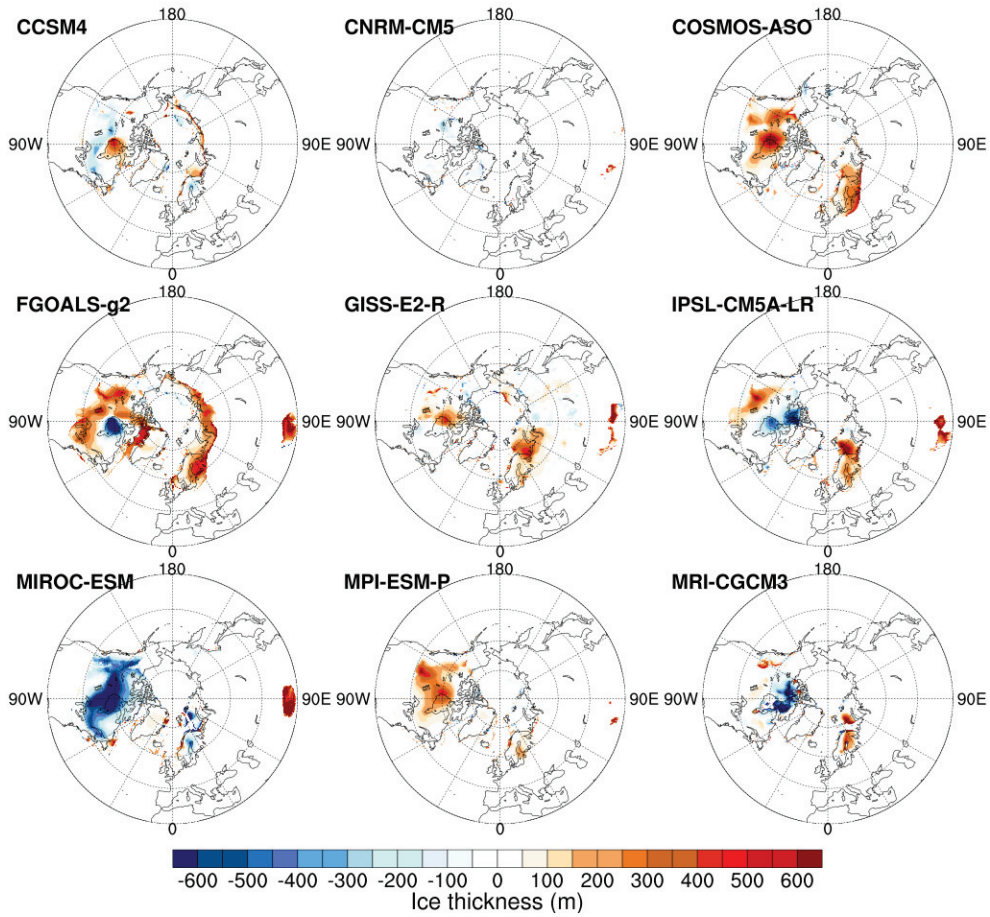


Figure 4.12: Simulated ice thickness differences at the LGM between experiments from PMIP3-PDobs and PMIP3-PIpmip3, PIpmip3-PDobs.

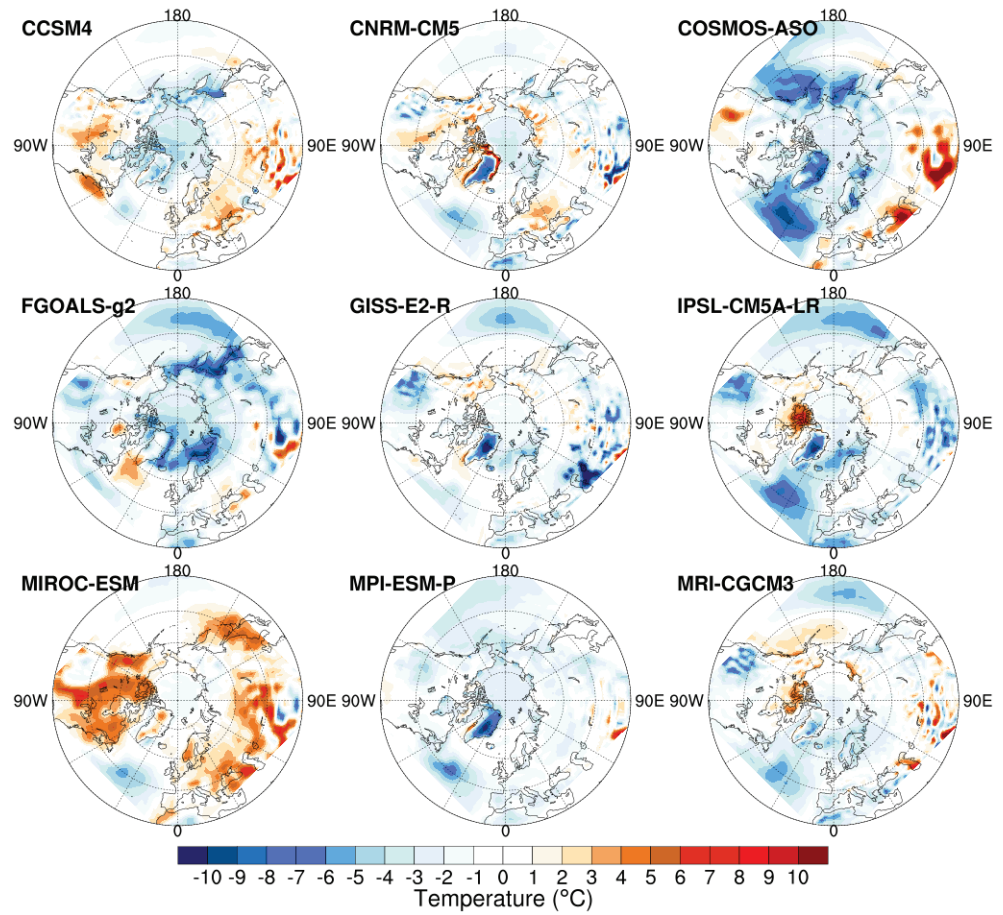


Figure 4.13: Summer (JJA) surface air temperature differences at present day between reanalysis products (PDobs) and PMIP3 PI GCM output (Pipmip3), Pipmip3-PDobs.

EFFECTS OF CLIMATE VARIABILITY ON ICE SHEET MEAN STATE

5.1 INTRODUCTION

Millennial-scale abrupt shifts between cold and warm states, called Dansgaard–Oeschger (DO) events (Dansgaard et al., 1993), are observed in Greenland ice core records through the last glacial cycle. The DO events began with a rapid warming of 8 to 15 °C within a few decades, followed by gradual cooling before a jump back to a cold state (Huber et al., 2006). Spectral analysis shows a typical recurrence time of 1470 years (Schulz, 2002). However, whether DO events are periodic or noise induced is still debated (Alley et al., 2001; Benzi et al., 1982; Ditlevsen et al., 2007; Ganopolski and Rahmstorf, 2002). In Antarctic ice cores, millennial scale oscillations with nearly opposite phase compared to Greenland are found, showing that this phenomenon is global in scale and might be related to the Atlantic ocean heat transport (Dima et al., 2018; EPICA Community Members, 2006). Other proxy records from different areas (e.g. North Atlantic Ocean sediments, European pollen and Chinese loess) also contain these signals (Bond et al., 1993; Porter, 2001; Woillard and Mook, 1982). Despite large research efforts, no consistent theory of the physical mechanism of the cause of DO events is widely accepted (Ganopolski and Rahmstorf, 2001; Petersen et al., 2013; Zhang et al., 2014b).

Global and regional change in surface temperature variability on decadal to millennial timescales (here called "climate noise") declined when the Earth system transitioned from a glacial to an interglacial condition (Rehfeld et al., 2018; Shao and Ditlevsen, 2016). The Northern Hemisphere ice sheets were restricted to Greenland during interglacials, and advanced further south to cover large portions of North America and northern Europe during glacials. Larger climatic variability (DO events) happened when ice sheets were intermediate in size, indicating that DO cycles are likely more closely linked to ice sheet evolution than to other potential drivers within the Earth system (Rahmstorf, 1995). Various studies applied numerical climate models to uncover the mechanism behind DO events, in terms of fresh-water perturbations or other potential drivers (Bond and Lotti, 1995; Broecker, 1994; Clark et al., 2001; Ganopolski and Rahmstorf, 2001; Rahmstorf, 1995; Zhang et al., 2014a; Zhang et al., 2014b). What is common to all these theories is that climate mean state determines climate variability. In the majority of these studies, the simulated climate states (here called "climate mean state") are prescribed with predefined

insolation, greenhouse gases and ice sheet configuration. Under this premise, the thermohaline circulation exhibits several modes, which could be linked to millennial-scale climate variability. With massive discharge of freshwater from ice sheets, the Atlantic Meridional Overturning Circulation (AMOC) is weakened and leads to a reduction of heat transport to the Northern Hemisphere, constituting a cold state (stadial). With a reduction of freshwater discharge, the AMOC is strengthened, constituting a warm state (interstadial).

However, how the climate variability regulates the mean state has not been fully investigated (as is shown in Fig. 1 in Timmermann and Lohmann, 2000). Cessi (1994) pointed out that the magnitude of stochastic noise is capable of modifying the equilibrium state of the ocean circulation in a Stommel two-box model (Stommel, 1961). Timmermann and Lohmann (2000) confirmed noise-induced transitions could be produced in a simplified ocean circulation model. Marshall et al. (2000) and Charbit et al. (2002) found that large century- to millennial-scale climate variability strongly impacts the evolution of simulated ice sheets. In a recent study, Mikkelsen et al. (2018) showed that the incorporation of interannual temperature fluctuations results in a smaller equilibrium Greenland ice sheet volume. These studies suggest that climate variability could in turn drive mean state changes.

In this chapter, we first investigate the influence of DO-like climate fluctuations on the Northern Hemisphere ice sheet evolution during glacial-interglacial cycles. We show how the ice sheet mean state is regulated by the fluctuations. Secondly, we conducted sensitivity experiments to see how the amplitude of climate noise affects the simulated ice sheets. Finally, a physical interpretation of our results is presented.

5.2 EXPERIMENT DESIGN

Abrupt temperature shifts imprinted in Greenland ice cores between cold (stadials) and warm (interstadials) states range from 8 to 15 °C in amplitude (Huber et al., 2006). The two distinct climate states are likely related to the Atlantic meridional overturning circulation, where interstadial (stadial) climate with strong (weak) overturning circulation is close to the preindustrial (the Last Glacial Maximum) condition (Ganopolski and Rahmstorf, 2001; Zhang et al., 2014a). From this perspective, the glacial index method (Sect. 2.2.1) is suitable for investigating the influence of these climate fluctuations on ice sheet evolution, since it synthesizes the necessary boundary conditions. Note that millennial-scale climate fluctuations cannot be fully represented with this method since orbital-scale signals may be misrepresented. However, matching the simulated ice sheets to the geological constraints under different time or spatial scales is not the main focus of this study.

Similar as the previous chapters, the simulations are driven by a glacial index I combined with monthly near-surface air temperature and precipitation fields at two time slices, the PI warm state ($I = 0$) and the LGM cold state ($I = 1$, Fig. 5.1a). The PI and the LGM climate states are taken from equilibrium simulations using the General Circulation Model COSMOS (Fig. 5.2, 5.3; Stepanek and Lohmann, 2012; Zhang et al., 2013). The isotope records from the Greenland ice cores are often used as a glacial index, but they only date back to the Last Interglacial (127,000 yr BP) due to the relatively high accumulation rate over Greenland. To extend our simulation, we use an 800,000-year synthetic record of Greenland climate variability from Barker et al. (2011), which is based on the Antarctica ice core record and a thermal bipolar seesaw model (Fig. 5.1a, black line). The Greenland synthetic record exhibits a larger variability within the last two glacial cycles than in the earlier cycles. This is likely because the signals are attenuated in the older and thinner ice layers. The model setup is the same as in the previous chapters (Chapt. 3, 4), except that the tuning factor β is 0.6 km^{-1} .

5.3 RESULTS

We conducted two experiments. One simulation was forced by the Greenland 800,000-year synthetic record which contains high frequency DO signals (GL_hf, Fig. 5.1a, black). In the other simulation, the DO signals and other high frequency variability were eliminated by applying a 5000-year running mean filter (GL_lf, Fig. 5.1a, red). The results show that the ice sheets grow larger when the DO signals are absent, while the mean forcing states are the same (Fig. 5.1b). The difference of the ice sheet volume between the two experiments, expressed as the equivalent contribution to eustatic sea level change (SLE), can be up to 60 m. The simulated SLE curves are compared to a reconstructed relative sea level record Rohling et al., 2014. The root-mean-square deviation (RMSD) between the model and the reconstruction is 40.3 m for GL_hf, and 52.0 m for GL_lf. During the last two glacial cycles, the consistency between the GL_hf SLE and the reconstruction increased significantly, with RMSD value of 21.7 m (42.0 m for GL_lf). A coherence test shows strong association between the simulated SLE and the climate forcing time series within the millennial timescale (Fig. 5.4). Note that the DO signals are stronger during the last two glacial cycles than for older times. We propose that the DO-like fluctuations significantly inhibit the ice sheet buildup processes. The relationship between the SLE difference of the two simulations and the amplitude of the climate variability (standard deviation of the index) is shown in Figure 5.1c. The simulated ice sheet volume is reduced in experiment GL_hf, which has large climate variabil-

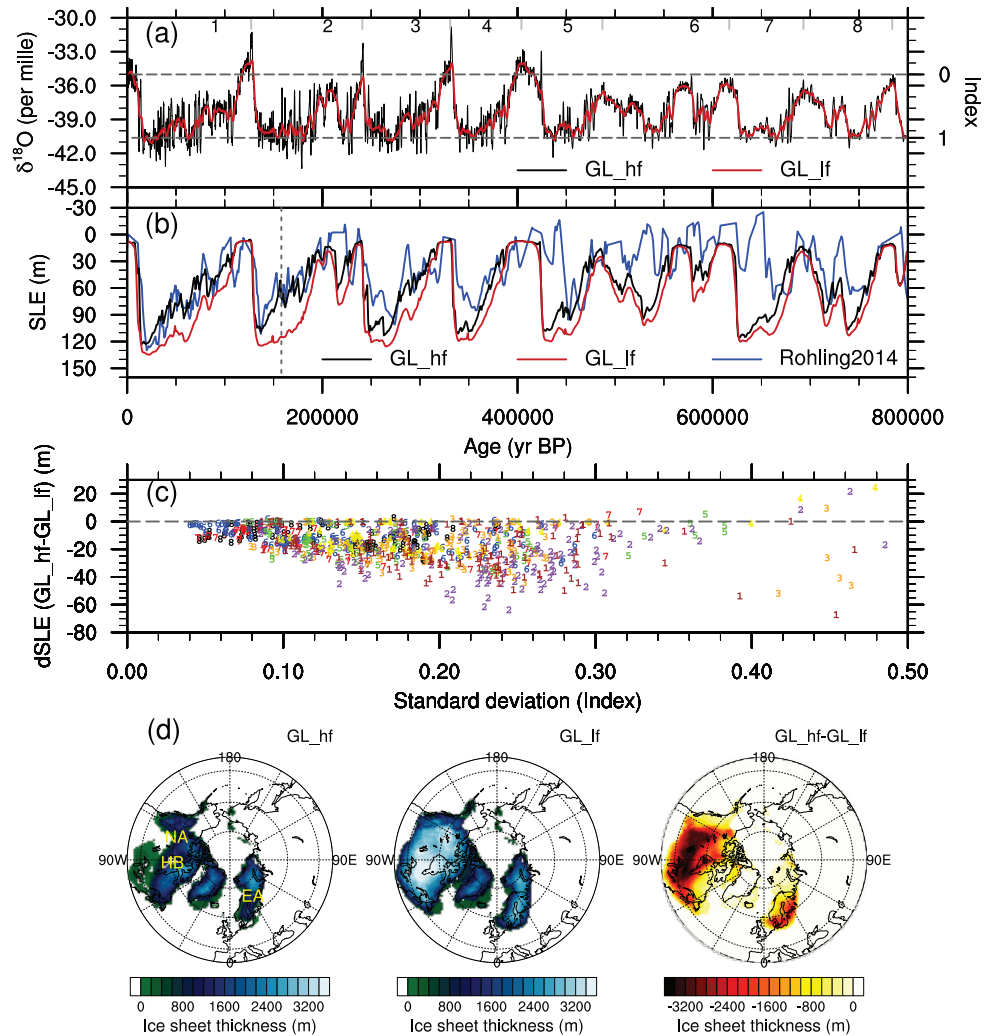


Figure 5.1: (a) The index used to determine the forcing of the simulated ice sheets. The time series is a Greenland synthetic $\delta^{18}\text{O}$ record derived from an Antarctic temperature record (Barker et al., 2011, black line). From 0 to 5000 year BP, the index is derived from the GISP2 Greenland ice core. The red line is the same record with 5000-year smoothing. (b) The simulated ice sheet sea level equivalent (SLE) and the reconstructed sea level record from Mediterranean (Rohling et al., 2014, blue line). The black line represents the simulation forced by the original $\delta^{18}\text{O}$ record with high variability (GL_hf), while the red line represents the simulation forced by the 5000-year smoothed record with low variability (GL_lf). (c) The scatter distribution between the simulated SLE difference (GL_hf-GL_lf) and the standard deviation from the index series. Different colors and numbers indicate different glacial cycles (1: the last glacial cycle, 2: the penultimate glacial cycle, and so on). (d) The simulated ice sheet thickness at 158000 yr BP, from experiments GL_hf, GL_lf and the difference between them (GL_hf - GL_lf). (NA: North American ice sheets. EA: Eurasian ice sheets. HB: Hudson Bay.)

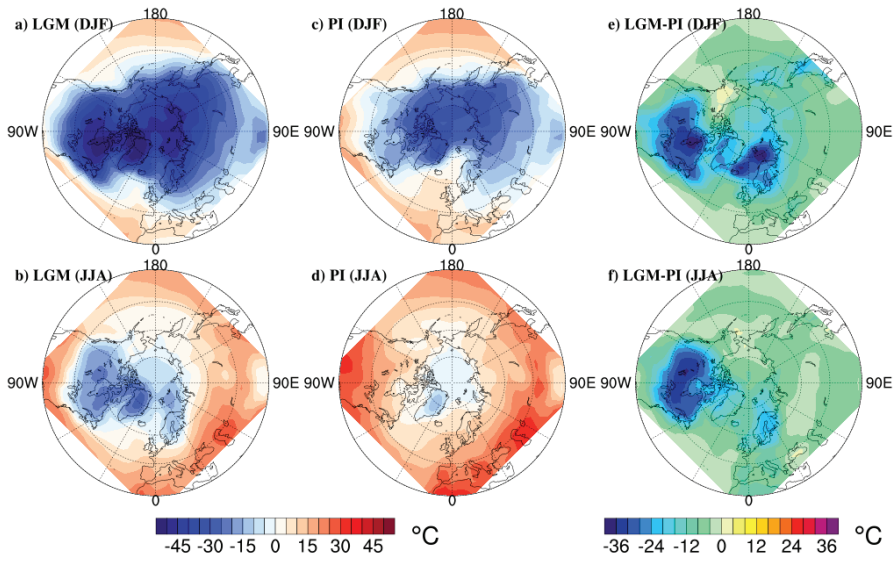


Figure 5.2: Winter (DJF) and summer (JJA) surface air temperature for the Last Glacial Maximum (LGM, a-b) and preindustrial (PI, c-d) from COSMOS output, and the difference between the LGM and PI (LGM minus PI, e-f).

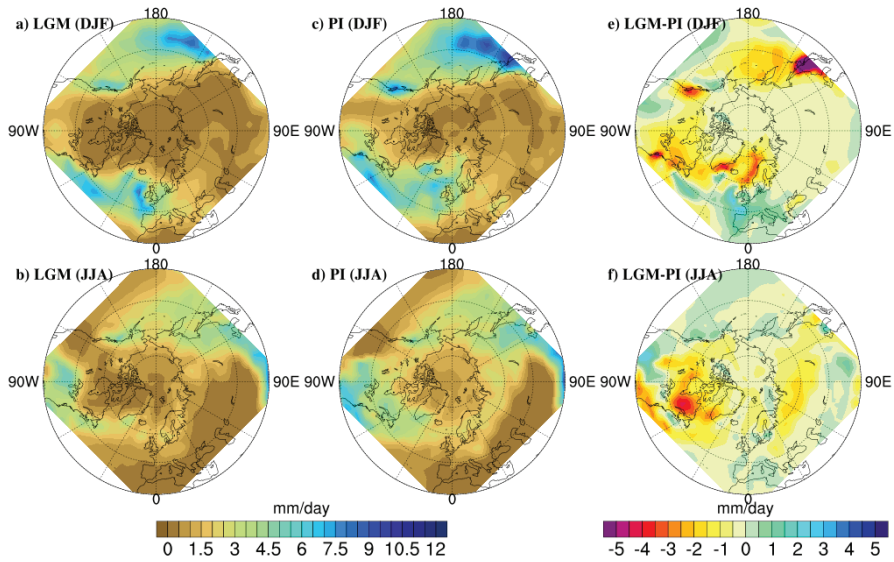


Figure 5.3: Same as Fig. 5.2, but for precipitation.

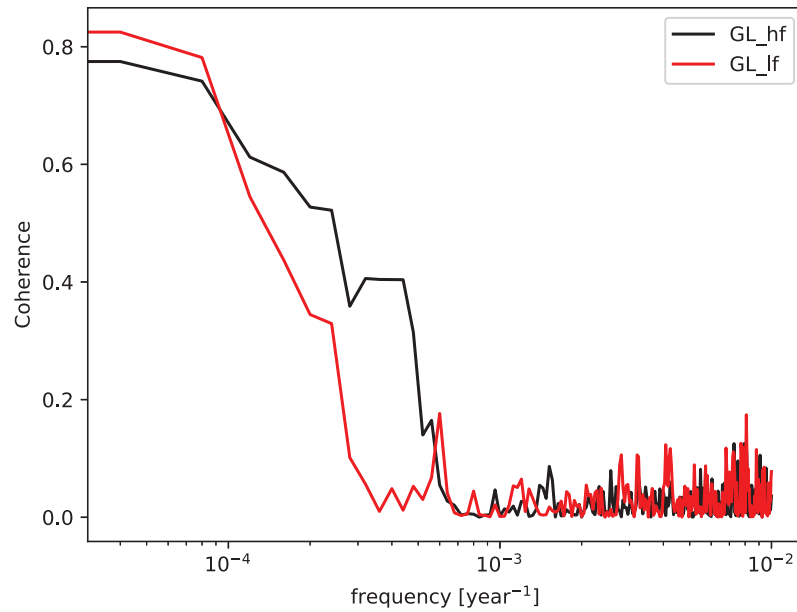


Figure 5.4: Coherence test between the glacial index forcing and the simulated sea level equivalent in Fig. 5.1a-b for experiment GL_hf and GL_lf.

ity. The larger the variability, the larger the maximum SLE difference ($|\text{GL_hf}-\text{GL_lf}|$) becomes.

The spatial distribution of the ice sheets also differs between the two experiments. Figure 5.1d shows the simulated ice sheet thickness pattern at 158,000 yr BP, when the SLE difference ($|\text{GL_hf}-\text{GL_lf}|$) is ~ 40 m (Fig. 5.1b). The North American ice sheets and Eurasian ice sheets extend much further south to around 40°N with lower climate variability (GL_lf). In experiment GL_hf, the North American ice sheets only reach the southern margin of the Hudson Bay. The difference in ice sheet thickness can be more than 3000 meters in southern North American ice sheets (Fig. 5.1d). Our results exhibit two distinct simulated ice sheet mean states during the ice sheet buildup stage. Ice sheets reach maximal full glacial conditions much earlier when the DO signals are absent.

To assess the influence of climate variability on the mean state of the ice sheets, we carried out sensitivity experiments. The isotopic record used for GL_hf and GL_lf is replaced by a cosine-based index. It ranges from 0 to 1 with a period of 120,000 years (Fig. 5.5). For different sensitivity experiments, white noise with different standard deviation σ (from 0 to 0.4 with 0.05 interval) was added onto the index. The simulations run for 120,000 years. The other parameters of the model setup are the same as before.

The results show hysteresis in all the simulated ice sheets. The glacial maximum occurs around year 70,000, instead of year 60,000 when temperature forcing is the lowest (Fig. 5.5i). The ice sheet retreat

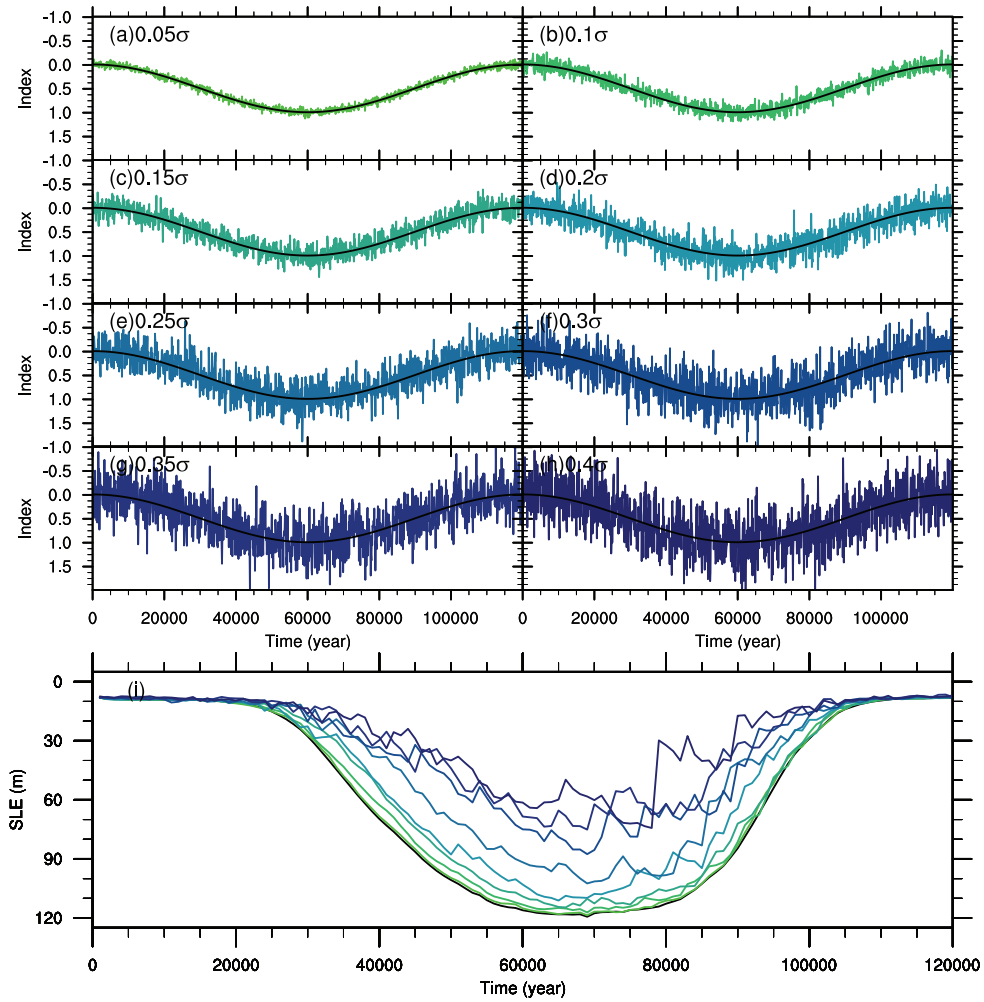


Figure 5.5: (a-h) The forcing index based on a cosine time series combined with different amplitude of white noise from year 0 to 120,000. (a) 0.05σ standard deviation. (b) 0.1σ . (c) 0.15σ . (d) 0.2σ . (e) 0.25σ . (f) 0.3σ . (g) 0.35σ . (h) 0.4σ . (i) The corresponding simulated ice sheet sea level equivalent (SLE) from year 0 to 120,000. Note that the y-axes are reversed.

period (from year 70,000 to year 120,000) is shorter than the buildup periods (from year 0 to year 70,000). All simulations end with similar **SLE** (about 8 meters) at 120,000 year. With different σ values, the simulated maximum **SLE** differs. The index with larger variability results in a smaller **SLE**. The simulated ice sheet with 0.4σ is half the size of the one with 0σ (black line). From the sensitivity experiments, we confirm that the simulated ice sheet mean state is influenced by the amplitude of climate noise. Larger amplitude variability slows down the ice sheet buildup process and results in smaller ice sheets at the glacial maximum.

5.4 DISCUSSIONS: THE PHYSICAL INTERPRETATION

Our results show that the simulated ice sheets tend to be smaller when influenced by climate noise. One possible reason could be the nonlinear response of Surface Mass Balance (**SMB**) to temperature. Such non-linearity could cause an asymmetry of the change in surface mass balance in response to positive and negative temperature anomalies. We demonstrate this in a theoretical way as follows.

We assume the annual temperature cycle in one location follows a cosine function (Reeh, 1989),

$$T(t) = T_{\text{mean}} + (T_{\text{mean}} - T_{\text{July}}) \cdot \cos(2\pi t/A) + T_{\text{noise}}(t), \quad (5.1)$$

where T_{mean} and T_{July} are the annual mean ($-10 \text{ }^\circ\text{C}$) and July mean ($0 \text{ }^\circ\text{C}$) surface air temperatures respectively. The time t is in days and A is one year (365 days). White noise (T_{noise}) with a standard deviation of $3 \text{ }^\circ\text{C}$ is added to account for synoptic variations (Krebs-Kanzow et al., 2018b, Fig. 5.6b, red). The potential surface melt rate over the year (M_A) can be computed with the semi-empirical **PDD** method (Reeh, 1989). The related degree-day factor value f_{PDD} is a freely tuned parameter to match the observed surface energy balance under different situations. Assuming a constant precipitation (P) of 0.002 m w.e./day and for snow

$$P_{\text{snow}}(t) = \begin{cases} P & \text{if } T(t) < 0 \\ 0 & \text{otherwise} \end{cases},$$

the surface mass balance over one year (SMB_A) can be estimated with a refreezing rate ($f_{\text{refreeze}} = 0.6$) as follows:

$$PDD = \int_0^A dt \int_0^\infty dT \cdot T(t), \quad (5.2)$$

$$M_A = f_{\text{PDD}} \cdot PDD, \quad (5.3)$$

$$P_{\text{snow}A} = \int_0^A P_{\text{snow}}(t) \cdot dt, \quad (5.4)$$

$$\text{SMB}_A = P_{\text{snow}A} - M_A \cdot (1 - f_{\text{refreeze}}) \quad (5.5)$$

Temperature changes are represented by shifting the annual cycle temperature curve up and down. The corresponding annual surface mass balance (SMB_A , noted with **SMB**) can also be calculated, as is shown in Fig. 5.6a (black line, $P = 0.002$ m/day, $f_{PDD} = 0.003$ m°C⁻¹ day⁻¹). We find a nonlinear relationship between the annual surface mass balance and the annual mean temperature. To be more specific, SMB is a concave downward function of T , i.e. $\frac{\partial^2(SMB)}{\partial T^2} < 0$. The larger the increase of temperature, the larger the loss of surface mass balance. We also varied the P and f_{PDD} values to test the sensitivity of the calculated surface mass balance (Fig. 5.6a). When we vary f_{PDD} from 0.003 m°C⁻¹ day⁻¹ for snow to 0.009 m°C⁻¹ day⁻¹ for ice (Ritz, 1997), the resultant **SMB** ranges from -4.38 to -13.14 m w.e./year with $T_{mean} = 10$ °C. However, the **SMB** has a linear response from 0 to ~1 m w.e./year when precipitation increases from 0 to 1 m/year.

Around the ice sheet margins of the non-marine terminating Northern Hemisphere ice sheets, the annual surface mass balance is negative at lower altitudes and positive at higher altitudes. Now we focus on the black line in Fig. 5.6a and assume that a point is located around the ice sheet margin with annual mean temperature of -6 °C and surface mass balance of 0 m w.e./year (intersection of dotted lines). The change of surface mass balance ($|\Delta SMB|$) responding to positive or negative temperature anomalies ($|\Delta T|$) are shown in Fig. 5.6c. Focusing on the red line (blue line), when the positive (negative) temperature anomaly increase, the surface mass balance decreases (increases) and the rate of change increases (decreases). As a result, the change of surface mass balance due to a warm anomaly can not be balanced by an identical cold anomaly ($d|\Delta SMB| \neq 0$, black line). In our case, a temperature variation of ± 5 °C can cause a potential reduction of 0.4 m w.e./year of surface mass balance. In summary, for a melt-dominated process, the increase of surface mass budget responding to negative temperature anomaly cannot compensate the decrease of surface mass budget responding to positive temperature anomaly. Thus, climate noise leads to a decrease of mean surface mass balance.

In reality, the surface mass budget is not only influenced by temperature but also precipitation change. The exponential relationship between water vapor saturation pressure and temperature can result in precipitation increase by 5-7% per degree increase in temperature (Huybrechts, 2002). As is shown in Fig. 5.3e-f, more precipitation is simulated in most of the Northern Hemisphere at **PI** than at the **LGM**. Such an adjustment could increase snow accumulation in winter which competes with the higher melt in the summer. This effect could be significant especially for accumulation-dominated areas, where **SMB** becomes a concave upward function of T , i.e. $\frac{\partial^2(SMB)}{\partial T^2} > 0$. In this case, climate noise would lead to an increase of mean surface mass balance. For example, in some regions in Antarctica, surface mass balance is increasing due to increasing precipitation with present warming

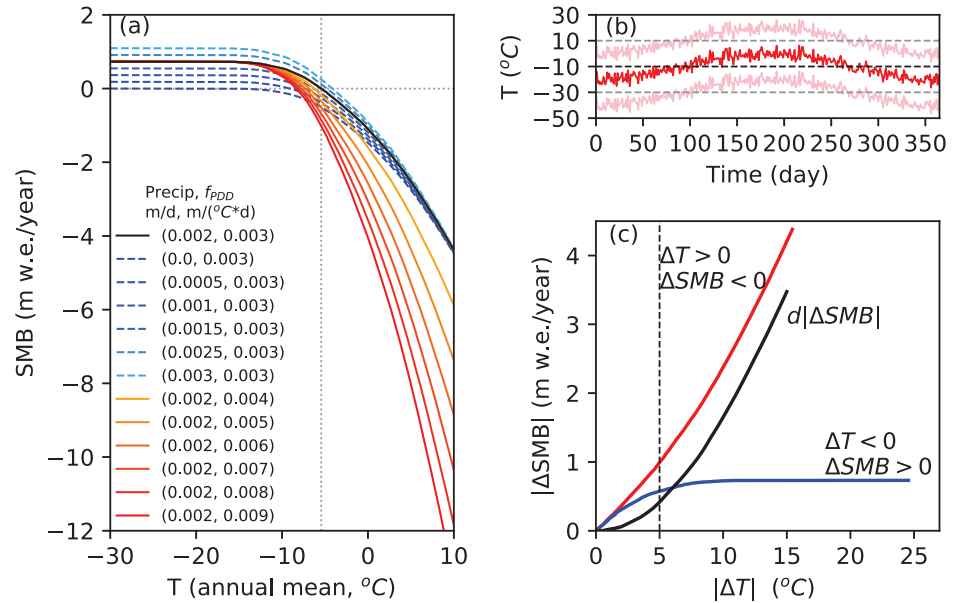


Figure 5.6: (a) The relation between the annual mean surface air temperature (T , °C) and the calculated surface mass balance (SMB, m w.e./year). The reddish (solid) lines represent varying degree-day factor (f_{PDD} , 0.003 - 0.009 m/(°C day)), the bluish (dashed) lines represent varying precipitation (P , 0.0 - 0.003 m/day). (b) The surface air temperature (T) over one year, from Eq. 5.1. White noise with a standard deviation of 3 °C is added on to the curve to account for the synoptic variations. The red line is with an annual mean temperature of -10 °C. The pink lines are shifted by ± 10 °C from the red line. (c) The relation between the annual mean temperature anomalies $|\Delta T|$ and the change of the resultant surface mass balance $|\Delta SMB|$, based on the intersection of dashed lines in (a). The red line is with the warm anomaly, the blue line is with the cold anomaly, the black is the difference between the red line and the blue line.

(Frieler et al., 2015). However, we propose that once the warming passes a tipping point, the melt process will be dominant and result to considerable surface mass loss.

The total ice sheet mass balance through time is much more complex due to calving and basal melting under grounded ice and ice shelves. However, we argue that surface mass balance is the main process accounting for ice gain, while the other processes account for ice loss and are mainly dependent on the ice sheet geometry (Cuffey and Paterson, 2010). In the sensitivity experiments (Fig. 5.5), the maximum ice sheet volume decreases when large temperature fluctuations are added. The larger the amplitude of the variability, the larger the decrease is. Another notable result from that is the hysteresis of the simulated ice sheet evolution, where the buildup processes are much slower than the retreat processes. One possible explanation is delayed isostatic rebound, in which the fast retreat is governed mainly by rapid ablation due to the lowered surface elevation (Abe-Ouchi et al., 2013). We propose that the non-linear relationship between surface mass balance and temperature could be another explanation. Due to that, the response time of the ice sheet buildup and retreat processes differ substantially (Ruddiman, 2001). Finally, although the maximum states are a function of the magnitude of the variability, all simulations end with similar SLE, showing the importance of climate mean state to interglacial states.

We also compared the simulated mean surface mass balance over the ice sheet domain for experiments GL_hf and GL_lf (Fig. 5.7b). We focus on the last two glacial cycles when the DO signals are more pronounced (Fig. 5.7a). For GL_lf, the surface mass balance is relatively constant (around 0.025 m/year) during the ice sheet buildup stages (e.g. 120,000 - 20,000 yr BP and 240,000 - 140,000 yr BP), while negative surface mass balance occurs mainly during glacial terminations. For GL_hf, the surface mass balance shows a strong asymmetric response to DO fluctuations. The positive SMB is no more than 0.064 m/year in response to DO fluctuations, while negative SMB can be as low as -0.205 m/year. The relationship between the $\delta^{18}\text{O}$ index and SMB is shown in Fig. 5.7c-d. Similar to Fig. 5.6a, the simulated SMB has a nonlinear response when climate forcing shifts between cold and warm states. The relation between the difference of $\delta^{18}\text{O}$ ($|\Delta\delta^{18}\text{O}|$) and the resultant surface mass balance ($|\Delta\text{SMB}|$) for the two experiments (GL_hf-GL_lf, Fig. 5.7e) shows similar features as in Fig. 5.6c, where the positive ΔSMB response to negative temperature anomalies has an upper limit (blue) while the negative ΔSMB is more scattered (red). This can lead to a significant reduction of the mean surface mass balance than without the variability.

Mikkelsen et al. (2018) demonstrated that interannual temperature fluctuations cause a smaller steady-state ice sheet volume of 1 m SLE using a minimal ice sheet model and from a theoretical derivation.

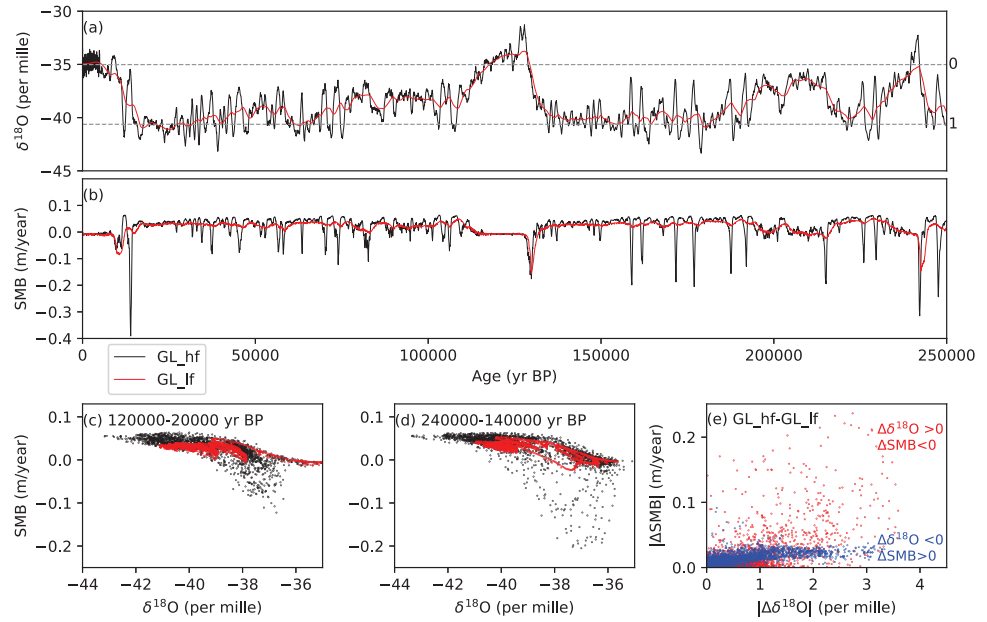


Figure 5.7: (a) The Greenland synthetic $\delta^{18}\text{O}$ time series. Same as Fig. 5.1, but from 250,000 to 0 yr BP. The red line is the time series with 5000-year smoothing. (b) The simulated mean surface mass balance (SMB) over the ice sheet domain from experiment GL_hf (black) and GL_lf (red). (c-d) The scatter plot between the simulated SMB and $\delta^{18}\text{O}$ during 120,000 - 20,000 yr BP (c) and 240,000 - 140,000 yr BP (d). (e) Scatter plot between $|\Delta\delta^{18}\text{O}|$ and the resultant $|\Delta\text{SMB}|$. The differences, Δ , for $\delta^{18}\text{O}$ and SMB are between experiment GL_hf and GL_lf (GL_hf-GL_lf).

In our study, we show that it is also valid for transient ice sheets under millennial-scale abrupt climate fluctuations. The maximum deviation of simulated ice sheet volume response to **DO** fluctuations can be up to 60 m **SLE**. More generally, the mean state of ice sheets is influenced by the amplitude of climate noise. Forced with high amplitude climate fluctuations, the ice sheet volume can be reduced significantly compared to the case without climate noise (Fig. 5.5). This phenomenon is attributed to the non-linearity of surface mass balance to temperature. The surface mass budgets are calculated with the **PDD** method. Since it is a semi-empirical method and can be tuned to match the observations, we hypothesize that using a surface energy balance model would lead to similar results.

Siddall et al. (2008) synthesized various reconstructed sea level records and found millennial-scale sea level fluctuations of 20 to 30 m magnitude during Marine Isotope Stage (**MIS**) 3 (60 - 27 kyr BP). Sea level fluctuated between 40 m and 80 m during **MIS** 4 (70 - 60 kyr BP) and **MIS** 3 (Chappell, 2002; Lambeck and Chappell, 2001), which is in line with the **GL_hf** simulation (Fig. 5.1b, black line). Comparing our results to the reconstructed sea level record from Rohling et al. (2014, blue line), we found better match when the **DO** fluctuations are considered (Fig. 5.1b). The terrestrial ice sheet reconstructions before the **LGM** are not well constrained, especially for North American ice sheets, due to erosion during the most recent glaciation (Dalton et al., 2016; Kleman et al., 2010; Svendsen et al., 2004). A synthesis of geological records in the Hudson Bay Lowlands suggests that the Laurentide Ice Sheet was significantly reduced during **MIS** 3 and grew rapidly towards the **LGM** (Dalton et al., 2019). Terrestrial chronologies from southern Greenland during early to late Holocene show that the Greenland ice sheet margins are sensitive to not only long-term (larger than 1000 years) but also short-term (less than 100 years) climate fluctuations (Reusche et al., 2018). Based on this evidence, we propose that the Northern Hemisphere ice sheets possibly underwent larger variability in response to the millennial-scale abrupt climate shifts than previously assumed (Stokes et al., 2012).

This study presents a novel perspective on the interplay between ice sheet evolution and climate noise. During glacial inception, smaller climate variability created conditions favorable for ice sheet buildup. As ice sheets grew, larger climate variability arose and prevented the ice sheets from further growth. This forms a negative feedback between the climate variability and ice sheet evolution, leading the Earth system towards an intermediate state. The simulated ice sheets without climate variability reached full glacial conditions much earlier than when there was significant climate variability (Fig. 5.1b), which can be more than 40,000 years. During **MIS** 4, the boreal summer insolation decreased to as low as the **LGM**, while CO_2 value was relatively high (~ 205 ppm) and the ice sheets were at an intermediate

size (Ahn and Brook, 2008; Lisiecki and Raymo, 2005). Van Meerbeeck et al. (2009) found a warmer equilibrium climate at MIS 3 than at the LGM, and showed that the climate sensitivity to insolation forcing is higher than greenhouse gas forcing. Schaefer et al. (2015) showed evidence that the Southern Hemisphere went from an interglacial condition to a full glacial condition at $\sim 65,100$ yr BP within a 15,000 year interval. They proposed that Northern Hemisphere ice sheets require half a glacial cycle to reach full glacial conditions. In our simulation (GL_hf), Northern Hemisphere ice sheets further build up with lower insolation during MIS 4, and reach an intermediate state with 80 m SLE. However, without the DO oscillations (GL_lf), ice sheets reach a full glacial state at 64 kyr BP, and maintain their shape through MIS 3. In other words, the climate variations favored maintaining an intermediate ice sheet configuration and corresponding climate. We propose that the large variability slowed down the ice sheet buildup process, and prevented the Earth system from entering a full glacial state from MIS 4 to MIS 3.

In our study, we emphasize the important role that DO fluctuations played on Northern Hemisphere ice sheet evolution. Similar to Cessi (1994) and Timmermann and Lohmann (2000), we show that the ice sheet mean state is regulated by DO-like fluctuations, and are affected by the climatic noise level. Although the glacial index that we used may not accurately represent the millennial-scale climate variability, the nonlinear dependence of the surface mass balance on temperature is considered to be a robust phenomenon. The nonlinear interactions between the ice sheet and atmosphere or ocean are not considered within this method (Abe-Ouchi et al., 2007; Liakka et al., 2012; Löffverström et al., 2015), and may affect the influence of the climate noise level on ice sheet development. A more complex coupled model is needed to account for the interplay between the ice sheet, the ocean and the atmosphere or other climate components, and to quantify the effect of climate noise on the climate (Rehfeld et al., 2018).

5.5 CONCLUSIONS

Our study shows that climate noise can significantly slow ice sheet development, and influence the ice sheet mean state. The larger the amplitude of the variability, the smaller the resultant ice sheets. We interpret that the nonlinear dependence of the surface mass balance on the temperature is the main reason for this phenomenon. In addition, this nonlinearity could also result in a hysteresis of the ice sheet evolution, whereby the buildup process is much slower than the retreat process. We propose that the DO events may significantly inhibit the development of Northern Hemisphere ice sheets, and prevented the Earth system from reaching a full glacial state from MIS 4 to MIS 3. This gives us a new perspective on understanding the role of

climate variations played within the Earth system, and shows that the Northern Hemisphere ice sheets are sensitive to millennial-scale abrupt climate shifts.

Part III

THE SHOWCASE 2

— The coupled climate-ice sheet modelling.

EFFECTS OF ORBITAL CHANGE ON NORTHERN HEMISPHERE ICE SHEETS DURING MIS 13

6.1 INTRODUCTION

The benthic $\delta^{18}\text{O}$ records from deep-sea sediments indicate that the variability of ice sheet volume is much smaller before ~ 400 kyr BP than after (Lisiecki and Raymo, 2005, Fig. 6.1). The temperature reconstruction from the Antarctic ice core deuterium record also shows the same feature (EPICA Community Members, 2006; Jouzel et al., 2007), as well as the greenhouse gas change (Siegenthaler et al., 2005). Overall, the interglacials were much cooler before 420 kyr BP than those after. The reason for this transition is still unknown.

Marine Isotope Stage (MIS) 13 (~ 524 to 474 kyr BP) is one of the interglacials which were relatively cooler than present day and probably had larger ice sheets. It is a long-lasting interglacial that has been split into three sub-stages, MIS 13.1, MIS 13.2 and MIS 13.3. MIS 13.1 is also divided into three sub-stages (13.11, 13.12, 13.13, Fig. 6.2). Correspondingly, the greenhouse gas values were relatively low, with CO_2 around 240 ppm. Although MIS 13 was less warm, the East Asian summer monsoon was found to be exceptionally strong (Yin and Guo, 2008).

Several modelling studies have been conducted to uncover the background climate during MIS 13. Besides the perihelion during Northern Hemisphere summer, a remnant Eurasian ice sheet is found can reinforce the East Asian summer monsoon through an atmospheric wave train (Muri et al., 2013; Yin et al., 2008). Using the Earth system Model of Intermediate Complexity (EMIC) LOVECLIM, Yin et al. (2009) further investigated the individual and combined effects of ice sheets and precession on MIS 13 climate with sensitivity experiments. They tested different sizes of ice sheets ranging from PI to the LGM, and different orbital forcing with two opposite precession configurations. They found that the strength of East Asian summer monsoon depends on ice sheet size under different astronomical configurations.

However, in all these studies, the ice sheets are prescribed. The ice sheet sizes and their locations are assumed based on the benthic $\delta^{18}\text{O}$ and the ice sheet configuration at the LGM (Yin et al., 2009). In our study, for the first time, we use a more sophisticated general circulation model (AWI-CM) with interactive Northern Hemisphere ice sheets (PISM). From an equilibrium perspective, we test the influence of difference orbital forcing on the Northern Hemisphere ice sheet configuration and the climate state. Firstly, we evaluate the perfor-

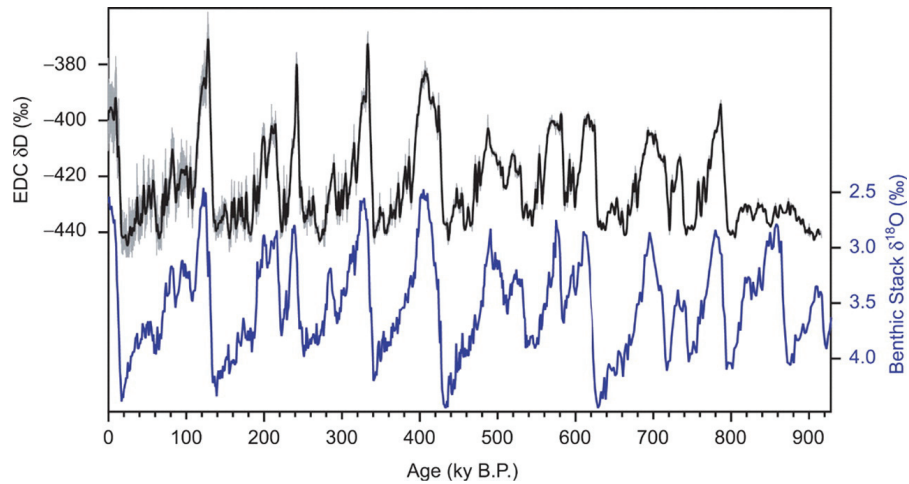


Figure 6.1: The δD Dome C record (EPICA Community Members, 2006; Jouzel et al., 2007) and the LR04 benthic $\delta^{18}O$ stack (Lisiecki and Raymo, 2005). The figure is from Jouzel et al. (2007).

mance of the coupled climate-ice sheet model AWI-CM-PISM under the preindustrial (PI) scenario. The simulated state with coupled PISM is compared to the simulation with fixed ice sheet configuration. Secondly, we investigate the MIS 13 climate under different astronomical configurations and the effects on the Northern Hemisphere ice sheet evolution. The feedback between the climate and ice sheets are then discussed.

6.2 EXPERIMENT DESIGN

As described in the model description (Sect. 2.3.2), the asynchronous coupling with 1x100 between AWI-CM and PISM is used in order to reach an equilibrium state. One experiment under PI scenario (PIo-ka) is first conducted as the reference simulation. Then we focus on the MIS 13 climate, for which three time slices (495, 506, 517 kyr BP) with different astronomical parameters are selected (Table 6.1). The boreal summer insolation at 65 °N reached its minima at 495 kyr BP and 517 kyr BP, with boreal summer at aphelion. However, the obliquity was the highest at 495 kyr BP and the lowest at 517 kyr BP. The boreal summer insolation at 65 °N reached maximum at 506 kyr BP at perihelion, and the obliquity was at an intermediate value. The greenhouse gas values are kept the same for the sensitivity analysis of the astronomical forcing of the MIS 13 climate (with a CO₂ concentration of 240 ppm, Loulergue et al., 2008; Siegenthaler et al., 2005; Spahni et al., 2005).

For the preindustrial (PI) scenario, the model is initialized from an equilibrium PI simulation without ice sheet dynamics (PInoIce, AWI-CM alone simulation, integrated for 2961 years). Afterwards, the climate model is integrated with ice sheet dynamics (PIo-ka) for 350

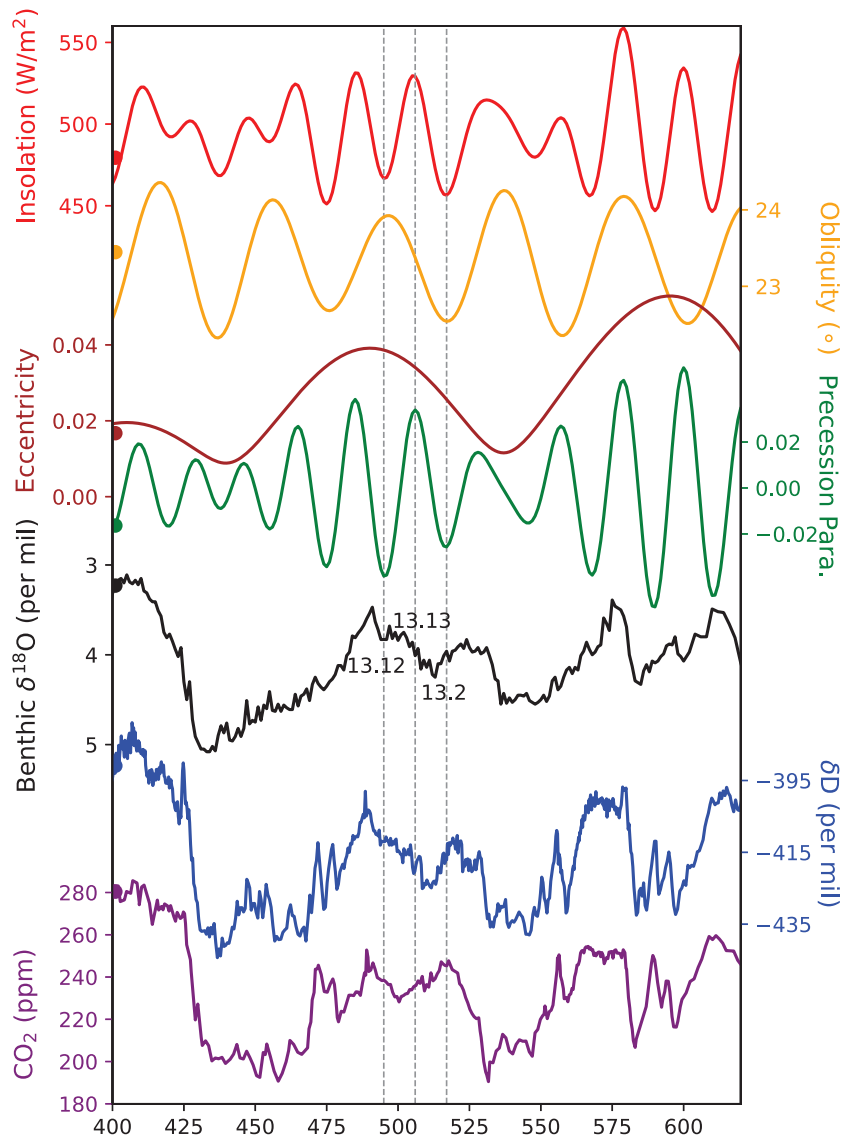


Figure 6.2: The boreal summer insolation at 65°N (red). The orbital parameters from Berger (1978): Obliquity (yellow), Eccentricity (brown) and Precession parameter (green, from spring equinox, param = $e \sin(\bar{\omega} + \pi)$). Benthic $\delta^{18}\text{O}$ from Lisiecki and Raymo (2005, black). δD from Antarctic Dome C (Jouzel et al., 2007, blue). CO_2 record from Hönisch et al. (2009, purple). The dots indicate the respective values for preindustrial (PI).

Table 6.1: Orbital parameters and greenhouse gases concentrations used in the experiments.

Exp. Name	Obliquity (°)	Eccentricity	Perihelion (lon, °)	CH ₄ (ppb)	CO ₂ (ppm)	N ₂ O (ppb)	Dyn. Ice
PInoIce	23.446	0.016724	102.157	760	280	270	No
506noIce	23.376	0.034046	274.100	510	240	280	No
PIo-ka	23.446	0.016724	102.157	760	280	270	Yes
495-ka	23.907	0.038638	97.617	510	240	280	Yes
506-ka	23.376	0.034046	274.100	510	240	280	Yes
517-ka	22.543	0.025640	91.309	510	240	280	Yes

years (ice sheet model for 35000 years) until the ice sheets reach a quasi-equilibrium state .

For the sensitivity experiments during MIS 13, we initialized the experiment 506noIce without coupled ice sheet and ran it for 745 model years (Table 6.1), so that the atmosphere component reached a quasi-equilibrium state. Then we activated the coupled ice sheets and ran the three time slice experiments with different orbital configurations. The orbital configuration was kept the same for experiment 506-ka for 350 climate model years (35000 years for ice sheets) until the ice sheet reached a stable state. The orbital configurations at the other two time slices were set to different values respectively, and ran for 550 climate model years.

6.3 THE REFERENCE PI CLIMATE WITH INTERACTIVE ICE SHEETS

The global mean surface air temperature for experiment PIo-ka with interactive ice sheets is 12.80 °C, which is 0.16 °C cooler than that without interactive ice sheets (PInoIce, 12.96 °C). The main contributing areas for this cooling are in the Southern Ocean. These regions are colder than those in PInoIce both in summer and winter (Fig. 6.3). Correspondingly, more sea ice is simulated in the Southern Hemisphere, especially around West Antarctica (Fig. 6.4).

The surface air temperature anomaly for PIo-ka compared to PInoIce in the North Atlantic displays a dipole pattern, with negative anomaly north of 50 °N and positive anomaly south of 50 °N. This indicates that the AMOC is weaker, causing a reduction of the northward head transport over the northern North Atlantic. A cold anomaly is also obtained in northern Canada, e.g. Hudson Bay and the Arctic Archipelago. In the northern part of the Eurasian continent, the seasonal cycle becomes weaker in experiment PIo-ka than in PInoIce, where the summer is colder while the winter is warmer (Fig. 6.3). The change in precipitation between these two experiments is not significant, except that

Table 6.2: Globally averaged surface air temperature (SAT) and the simulated Northern Hemisphere (NH) ice sheet volume in the experiments.

Exp. Name	Glob. Mean SAT (°)	Ice Sheet Volume (NH) Sea Level Equivalent (m)
PInoIce	12.96	-
506noIce	11.92	-
PIo-ka	12.80	~11
495-ka	11.88	~25
506-ka	11.90	~10
517-ka	11.60	~27.5

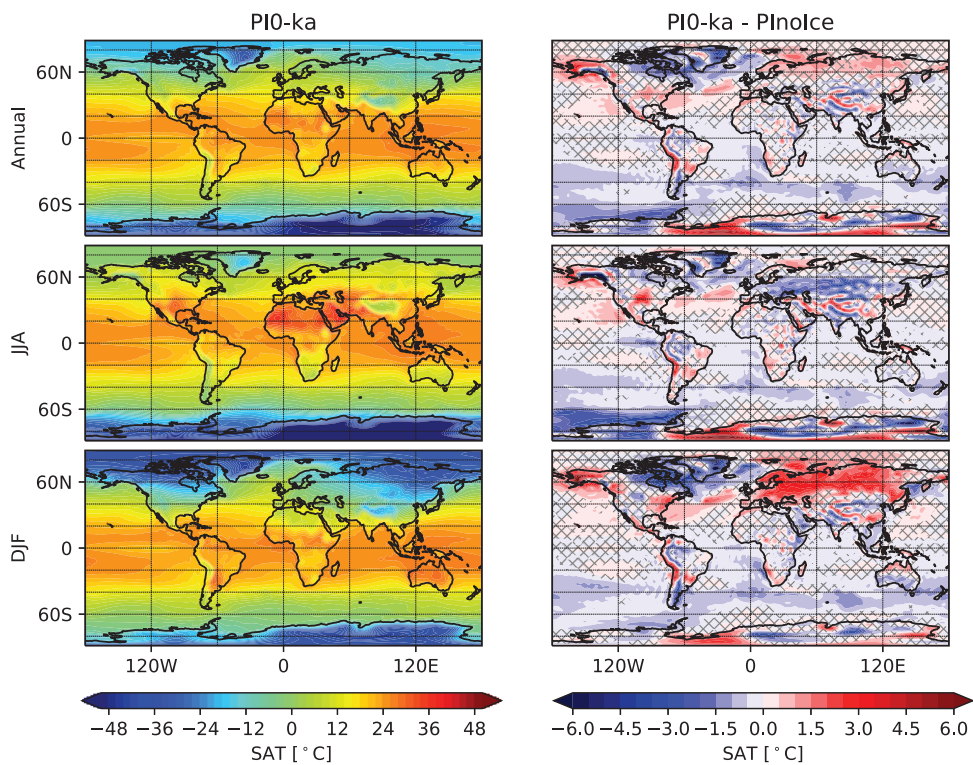


Figure 6.3: The simulated annual mean (Annual), summer (JJA), winter (DJF) surface air temperature (SAT) pattern for experiment PIo-ka, and the difference between PIo-ka and PInoIce. The hatched area did not pass the 0.05 significant level.

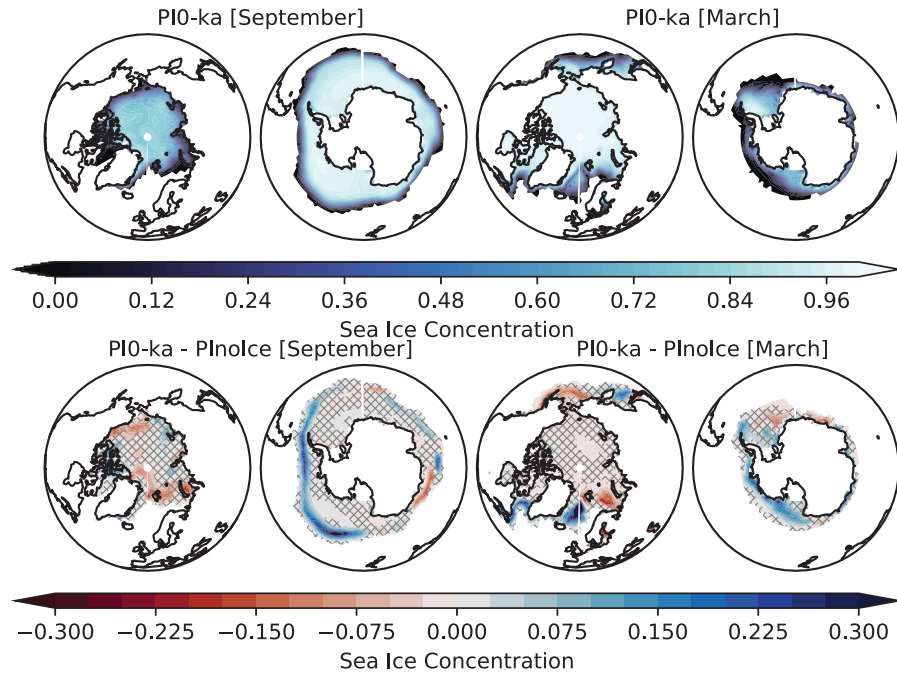


Figure 6.4: The simulated sea ice concentration for experiment Plo-ka in September and March, and the difference between Plo-ka and PInoIce. The hatched area did not pass the 0.05 significant level.

slightly more precipitation is simulated over Europe and the northern Indian Ocean in Plo-ka (not shown).

The simulated Northern Hemisphere ice sheet volume in experiment Plo-ka is ~ 11 m SLE. Comparing to the present day ice sheet configuration (Fig. 6.5, PInoIce, ~ 7 m SLE), the simulated Greenland ice sheet is more extended, but flatter. This is consistent with the simulated surface air temperature pattern, where there are negative anomalies over Greenland Ice Sheet margins and positive anomalies over the central area. In addition, Cordilleran Ice Sheet is built up over Coast Mountains. Small ice caps are also simulated in the Arctic Archipelago.

6.4 THE MIS 13 CLIMATE WITHOUT INTERACTIVE ICE SHEETS

Several studies have been conducted to examine the MIS 13 climate using climate models with different complexity and prescribed ice sheet configuration (Muri et al., 2012, 2013; Yin et al., 2009; Yin et al., 2008). In this section, we evaluate the performance of AWI-CM climate model during MIS 13 (at 506 kyr BP) and compare the results with previous literature. We compare the simulated results from experiment 506noIce for MIS 13.13 climate to the PI scenario from experiment PInoIce.

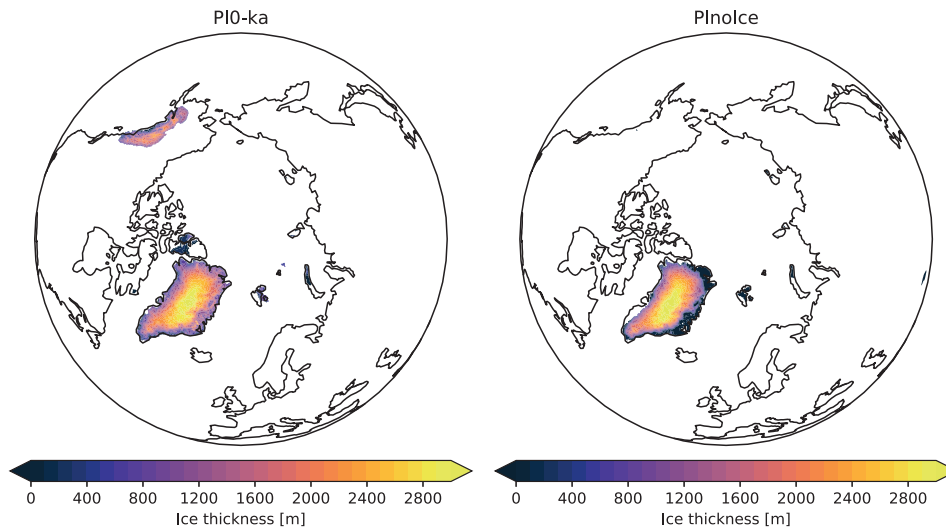


Figure 6.5: The simulated ice thickness for experiment P10-ka and P1noIce.

The insolation change at 506 kyr BP with respect to **PI** is shown in Figure 6.6. The global mean surface air temperature for experiment 506noIce is 11.92 °C, around 1.04 °C colder than preindustrial condition (P1noIce). This is probably due to the lower greenhouse gas value (240 ppm CO₂). Larger seasonality is shown in the simulated pattern. The summer temperature in the Northern Hemisphere mid-latitudes is 6–8 °C warmer than **PI**, while the winter temperature is colder than **PI** almost over the whole globe (Fig. 6.7). This phenomenon can be interpreted by the change of the orbital forcing. Although the obliquity values at 506 kyr BP and **PI** are similar, the precessional angles are at opposite phases. The Northern Hemisphere summer at 506 kyr BP was at perihelion, while winter was at aphelion. This could strengthen the insolation of Northern Hemisphere in summer and weaken the insolation in winter, resulting in larger seasonality. As a result, the land-ocean thermal contrast over the Northern Hemisphere continents is strengthened, which can cause stronger summer monsoons and a shift of Intertropical Convergence Zone. As shown in Fig. 6.8, more precipitation is simulated over China, India and North Africa in summer, indicating stronger East Asian, Indian and North African summer monsoons. This is consistent with previous modelling results with **EMICs** or **GCMs** (Muri et al., 2012, 2013; Yin et al., 2009; Yin et al., 2008), and also matches geological evidence (e.g. Yin and Guo, 2008).

In response to the colder Southern Hemisphere, the simulated sea ice especially around eastern Antarctica is much more northward extended (Fig. 6.9). The sea ice concentration around western Antarctica increases in March, while it slightly decreases in September, which might be related to the change of Antarctic Circumpolar Current. In the Arctic, the sea ice concentration increases especially over Greenland Sea and Bering Sea in March. However, there is no significant

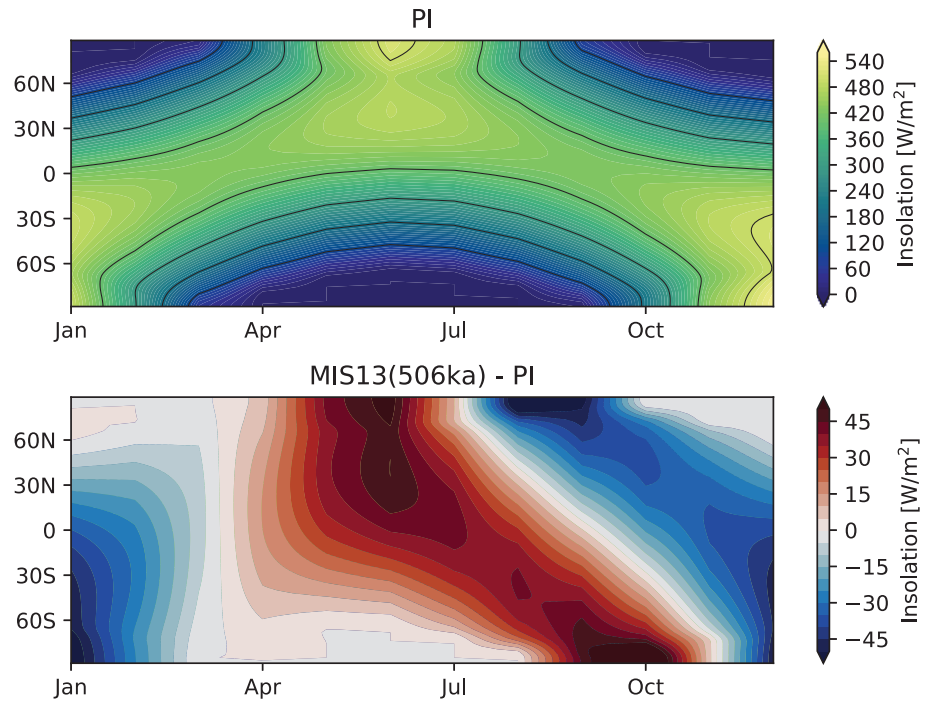


Figure 6.6: The insolation at PI and the difference between 506 kyr BP and PI.

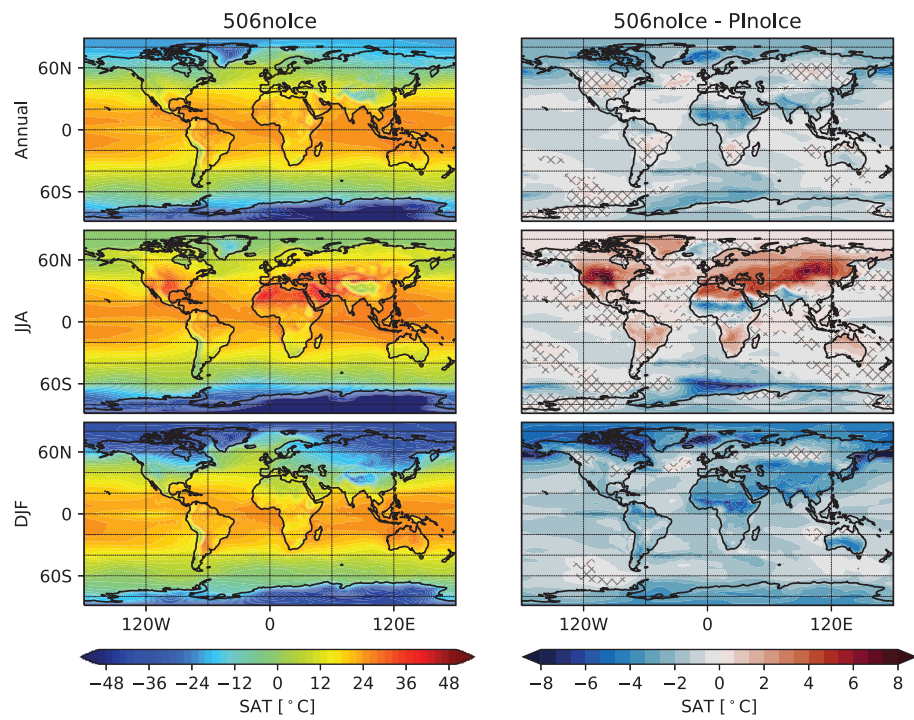


Figure 6.7: Similar as Fig. 6.3, but for experiment 506noIce, and the difference between 506noIce and PI noIce.

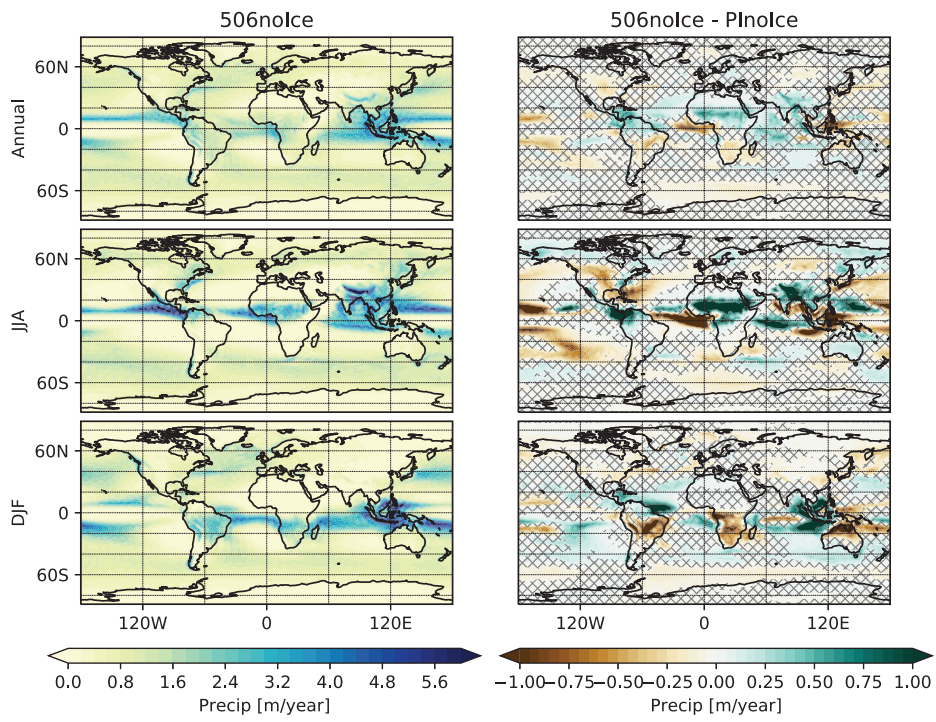


Figure 6.8: The simulated annual mean (Annual), summer (JJA), winter (DJF) precipitation (Precip) pattern for experiment 506noIce, and the difference between 506noIce and PInoIce. The hatched area did not pass the 0.05 significant level.

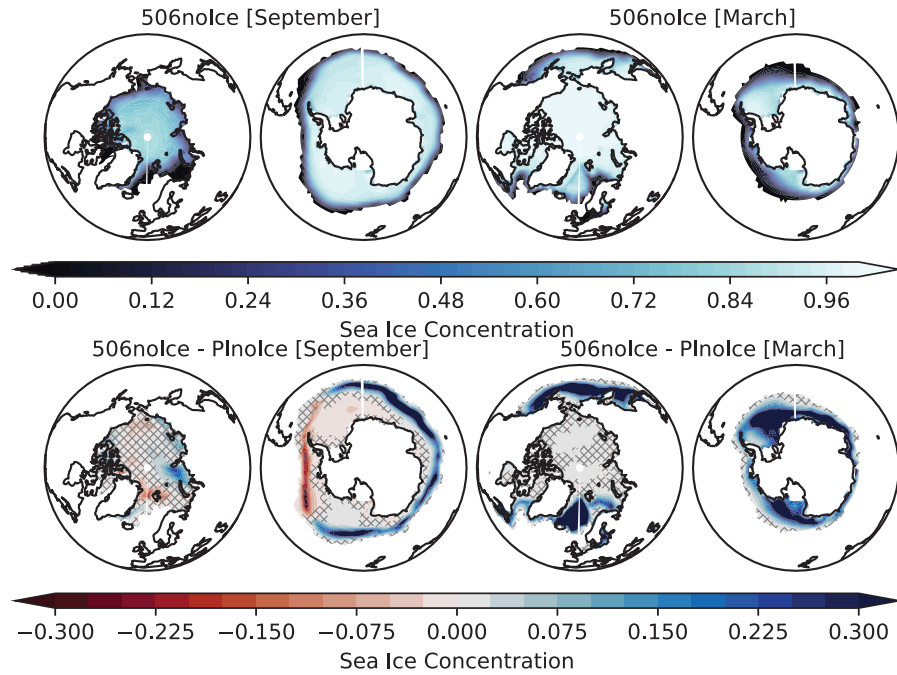


Figure 6.9: Similar as Fig. 6.4, but for experiment 506noIce, and the difference between 506noIce and PI noIce.

change in September. The simulated sea ice concentration patterns are also similar to those simulated by HadCM3 (Muri et al., 2013).

6.5 MIS 13 CLIMATE WITH INTERACTIVE ICE SHEETS

6.5.1 The 495 ka Climate

The boreal summer insolation at 65°N at 495 kyr BP is similar to PI, but with a slightly higher obliquity and larger eccentricity (Fig. 6.2), as well as lower greenhouse gases values. The simulated surface air temperature at 495 kyr BP (11.88°C) is globally colder than at PI, especially during summer (Fig. 6.10). This is probably due to the lower greenhouse gases values. There is no significant change in precipitation except the tropical regions (not shown). The simulated sea ice concentration increases in September especially in Southern Hemisphere, while in March there is no significant change except an increase in the Greenland Sea (Fig. 6.11). The simulated Northern Hemisphere ice sheets volume is ~ 25 m SLE, with more ice simulated in Ellesmere Island, Svalbard, Severny Island, Tibet, as well as a much thicker and more extended Cordilleran Ice Sheet (Fig. 6.12b).

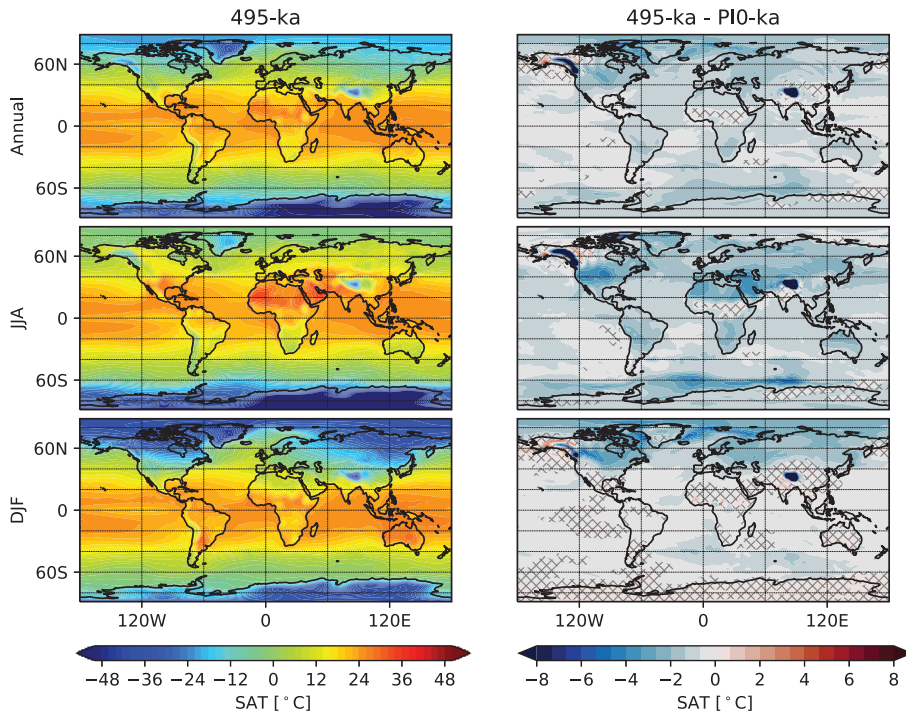


Figure 6.10: Similar as Fig. 6.3 for surface air temperature (SAT), but for experiment 495-ka, and the difference between 495-ka and PI0-ka.

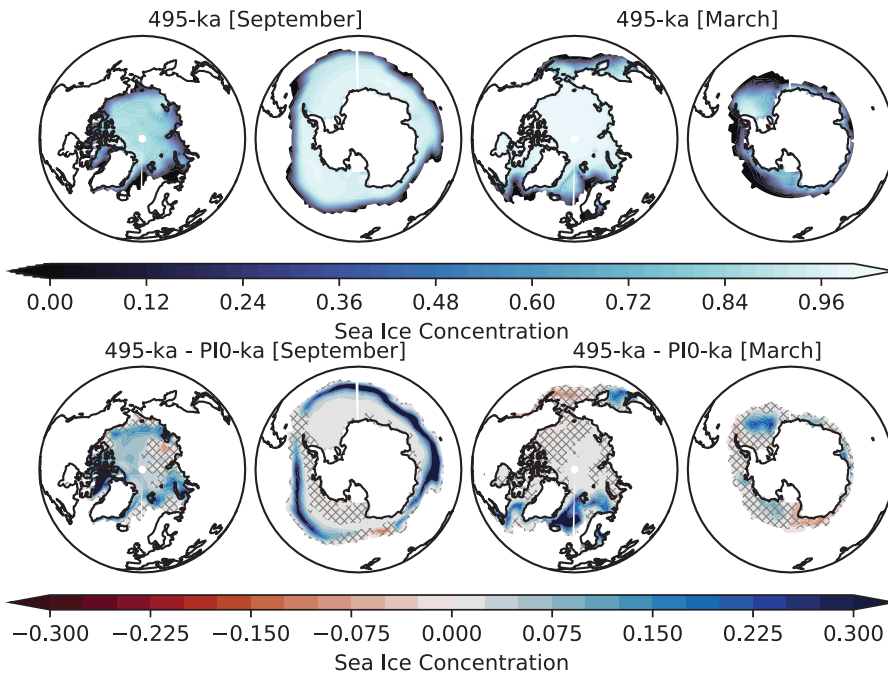


Figure 6.11: Similar as Fig. 6.4 for sea ice concentration, but for experiment 495-ka, and the difference between 495-ka and PI0-ka.

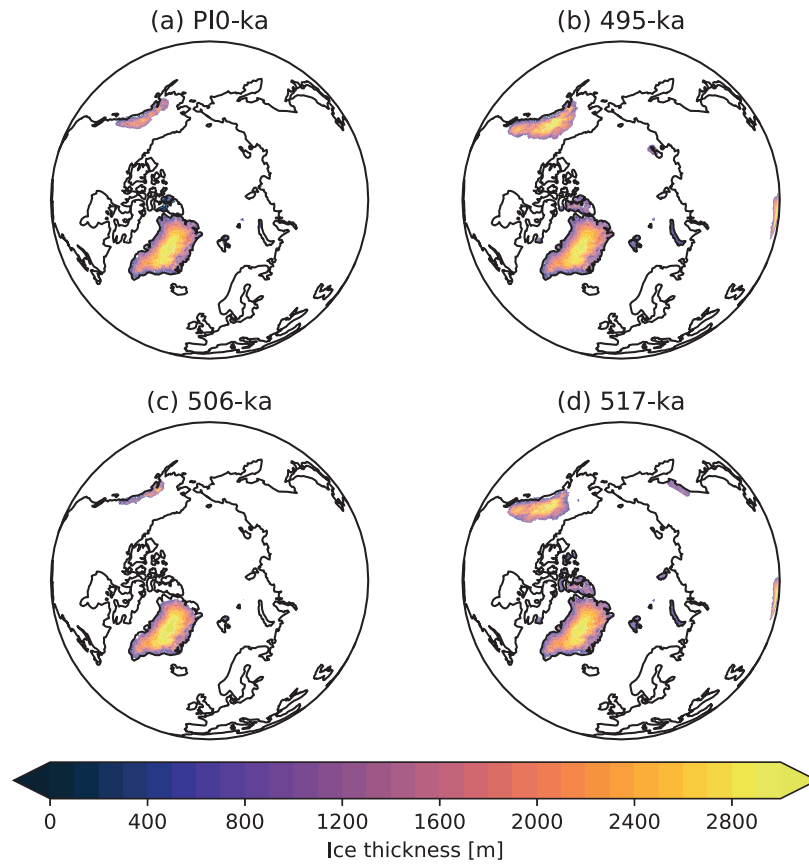


Figure 6.12: The simulated ice thickness for experiment (a) 10-ka, (b) 495-ka, (c) 506-ka, (d) 517-ka.

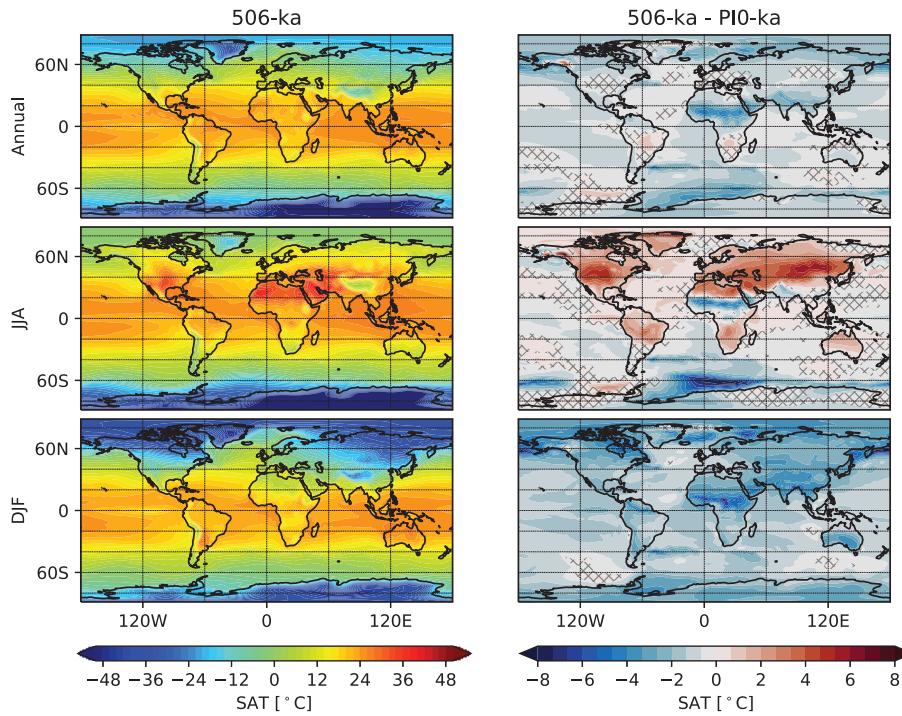


Figure 6.13: Similar as Fig. 6.3 for surface air temperature (SAT), but for experiment 506-ka, and the difference between 506-ka and PI0-ka.

6.5.2 The 506 ka Climate

The distribution of the surface air temperature (Fig. 6.13), precipitation and sea ice concentration (Fig. 6.14) for experiment 506-ka with interactive ice sheets is similar as the one without interactive ice sheets (experiment 506noIce, Fig. 6.7, 6.8, 6.9). The global mean surface air temperature is $0.02\text{ }^{\circ}\text{C}$ colder than 506noIce. The seasonality is much larger than that at PI especially over Northern Hemisphere mid-latitude continents. Since the ice sheets are mainly influenced by the summer temperature, the simulated ice sheet volume is $\sim 10\text{ m SLE}$. It is less than the PI configuration, where smaller Cordilleran Ice Sheet is simulated (Fig. 6.12c).

6.5.3 The 517 ka Climate

The obliquity at 517 kyr BP is the lowest during MIS 13, and the boreal summer is at aphelion. The global mean surface air temperature is the lowest among all the experiments. The temperature differences between 517-ka and PI can be low to $-8\text{ }^{\circ}\text{C}$ in winter for both hemispheres (Fig. 6.15). The Arctic sea ice concentration increases significantly in the Arctic ocean in September, and in the North Atlantic in March (Fig. 6.16). For Antarctic sea ice, the sea ice concentration increases in

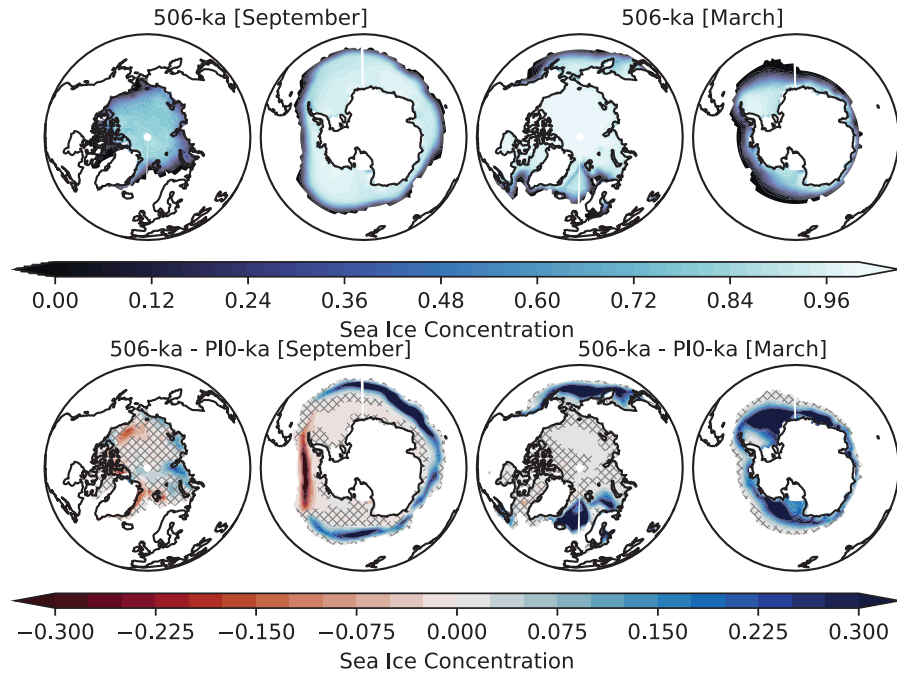


Figure 6.14: Similar as Fig. 6.4 for sea ice concentration, but for experiment 506-ka, and the difference between 506-ka and PI0-ka.

eastern Antarctica in September, and increases all around the Antarctic continent in March than at PI. More ice sheets are simulated in Arctic islands, Tibet and Coast Mountains in experiment 517-ka in response to a colder climate than PI (Fig. 6.12d). There is no significant change in precipitation except in the tropical regions (not shown).

6.6 DISCUSSIONS

6.6.1 *The Effect of Precession*

Figure 6.17 (upper panel) illustrates the insolation difference between 506 kyr BP (\sim MIS 13.13) and 495 kyr BP (\sim MIS 13.12). The obliquity at 506 kyr BP is close to that at 495 kyr BP, but the precessional angles at these two time slices are at opposite phases. As discussed before, boreal summer at 506 kyr BP is at perihelion. This results in a significant increase in Northern Hemisphere summer insolation, and reduction in Southern Hemisphere summer insolation. The surface air temperature at 506 kyr BP increases up to 8 °C over mid-latitude continents in summer, while it decreases especially in Antarctica and Northern Hemisphere lower latitudes in winter (Fig. 6.18, left panel). Correspondingly, less (more) sea ice forms in summer (winter) than at 495 kyr BP (Fig. 6.19, left panel). Since Northern Hemisphere ice

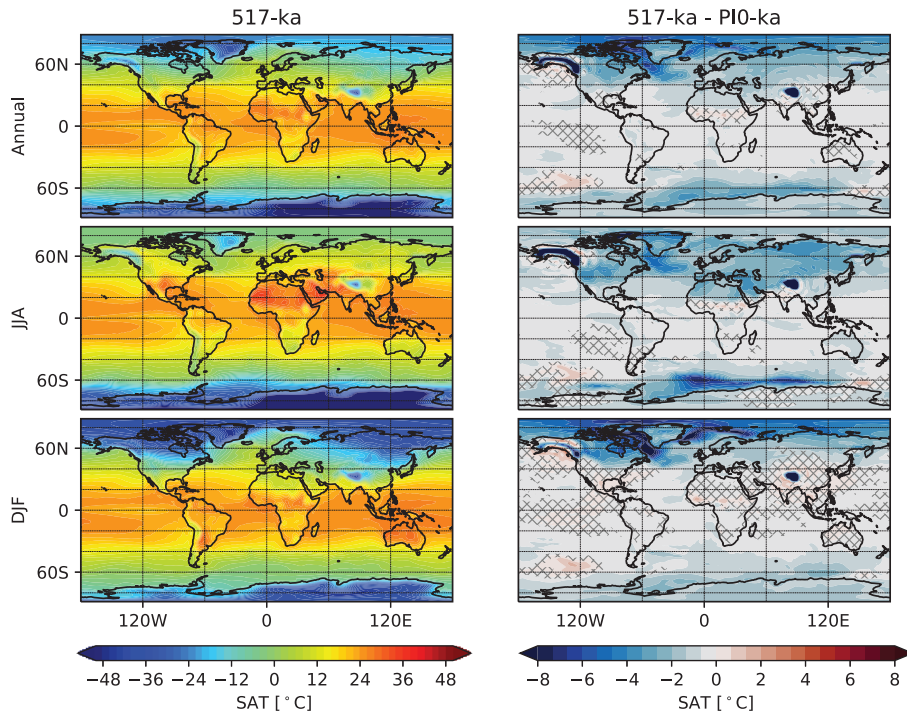


Figure 6.15: Similar as Fig. 6.3 for surface air temperature (SAT), but for experiment 517-ka, and the difference between 517-ka and PI0-ka.

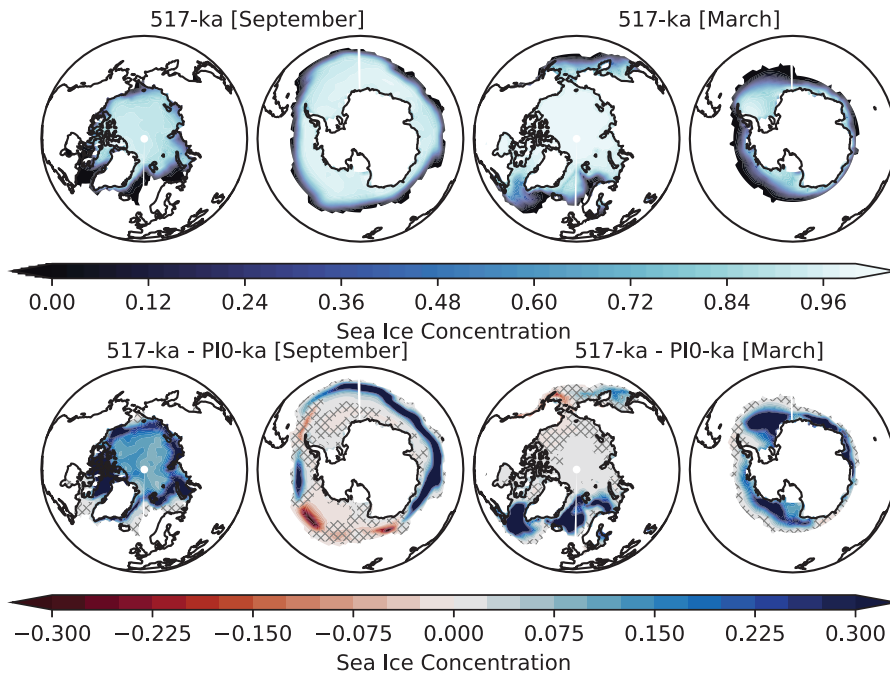


Figure 6.16: Similar as Fig. 6.4 for sea ice concentration, but for experiment 517-ka, and the difference between 517-ka and PI0-ka.

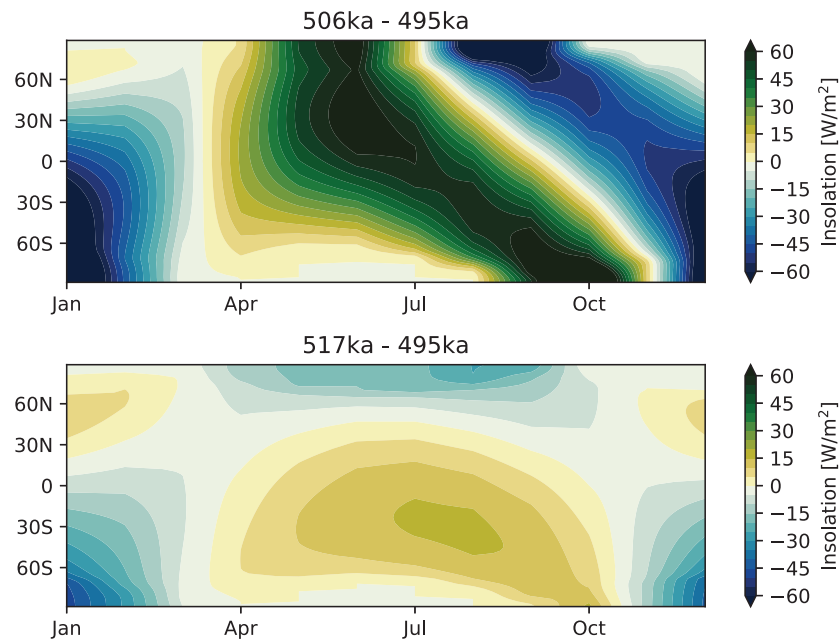


Figure 6.17: Insolation difference between 506 and 495 kyr BP (506-ka - 495-ka), and 517 and 495 kyr BP (517-ka - 495-ka).

sheets are mainly influenced by summer temperature, the ice sheet volume tends to decrease (Fig. 6.12c).

6.6.2 The Effect of Obliquity

The boreal summer for 517 kyr BP (\sim MIS 13.2) and 495 kyr BP (\sim MIS 13.12) are both at aphelion, while the obliquity angles are at the lowest and the highest respectively. The lower obliquity causes less insolation received at high latitude in summer, and more insolation received at low latitude from April to October (Fig. 6.17, lower panel). As a result, lower surface air temperature is simulated at polar regions almost all the year round (Fig. 6.18, right panel), as well as a higher simulated sea ice concentration (except western Antarctica in September, Fig. 6.19). This causes a substantial increase of Northern Hemisphere ice sheets (Fig. 6.12d) in polar regions.

6.6.3 The MIS 13 Ice Sheets

Yin et al. (2009) assume that there is a linear relationship between the benthic $\delta^{18}\text{O}$ and the total ice volume on the Earth (see equation 6.2). With this assumption, the excess ice volume (ΔV , referenced to present Greenland and Antarctic Ice Sheets) during MIS 13.1 varies from 17 m to 45 m SLE based on different benthic $\delta^{18}\text{O}$ reconstruction (Lisiecki and Raymo, 2005; Shackleton, 2000). In their study, they assume that

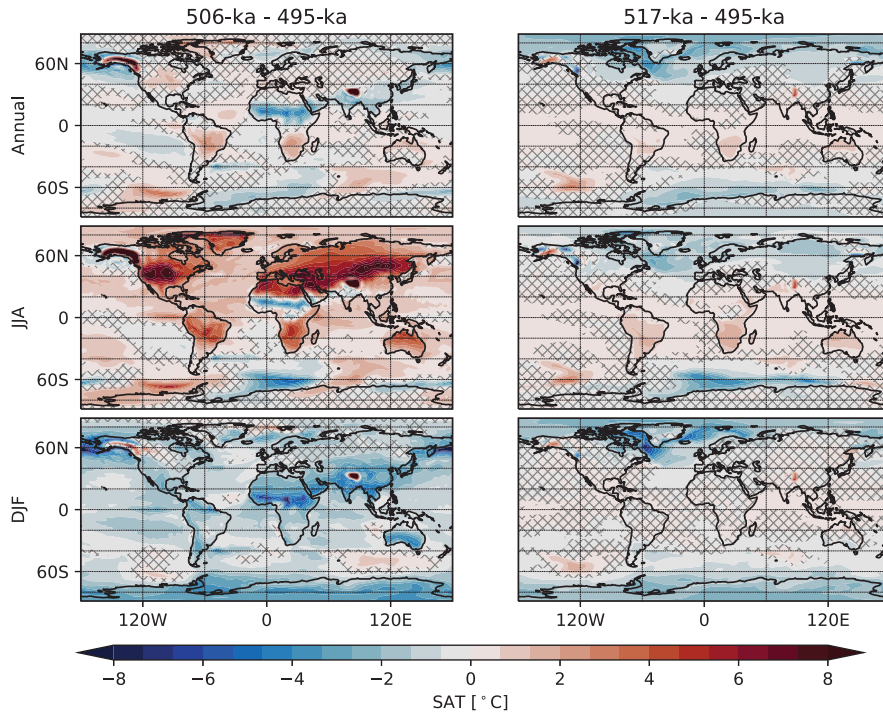


Figure 6.18: The surface air temperature (SAT) differences between experiment 506-ka and 495-ka (506-ka - 495-ka, left panel), and between experiment 517-ka and 495-ka (517-ka - 495-ka, right panel).

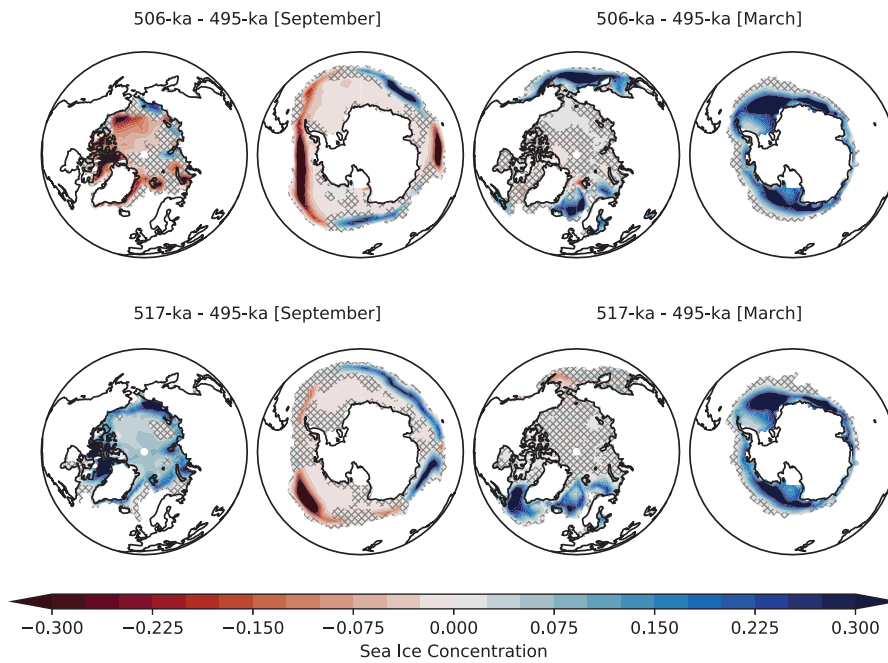


Figure 6.19: Similar as Fig. 6.18, but for sea ice concentration.

the excess ice is located in North America and Eurasia as reconstructed since the LGM. In our equilibrium simulations, the excess ice sheet volume (ΔV , see equation 6.1) for 495-ka is ~ 14 m SLE with respect to PIo-ka. The Cordilleran Ice Sheet increases significantly, as well as Tibet, which is probably due to the higher bedrock elevation. Besides, small ice sheets are also built up on the Arctic islands (Fig. 6.12b), probably in response to lower values of greenhouse gases.

$$\begin{aligned}\Delta V(t) &= V(t) - V(\text{PI}) & (6.1) \\ &= \frac{V(\text{LGM}) - V(\text{PI})}{\delta^{18}\text{O}(\text{LGM}) - \delta^{18}\text{O}(\text{PI})} \cdot [\delta^{18}\text{O}(t) - \delta^{18}\text{O}(\text{PI})] & (6.2)\end{aligned}$$

The benthic $\delta^{18}\text{O}$ reaches a minimum during MIS 13.2 with 4.25 per mil in Lisiecki and Raymo (2005), possibly with up to ~ 70 m SLE excess ice sheets. In our simulation, around 16.5 m SLE excess ice is simulated at 517 kyr BP in response to a lower obliquity. The ice sheets grow mainly over Coast Mountains, Tibet and islands in polar regions. However, less equilibrium ice volume than PI is simulated during MIS 13.13 (506-ka).

Ice sheets, as a slow climate component, require tens of thousand years to adapt to external changes. In reality, the Earth system was forced by transient orbital change. It is unlikely that the ice sheets reached equilibrium states, and probably still had memory from earlier periods. This could be one of the reason for the mismatch between the deduction from benthic $\delta^{18}\text{O}$ data and the model simulations. More importantly, multi-stability is found in simulated ice sheets when orbital forcing varies from cold to warm phase or in reverse, especially with lower CO_2 values (Calov and Ganopolski, 2005). In our simulations, we only initiated from an interglacial state due to the limitations of computing resources. However, initiating from a glacial state might result to different ice sheet equilibrium configurations. Lastly, the linkage between the benthic $\delta^{18}\text{O}$ and ice volume might be nonlinear, where deep ocean temperature also plays a role (Mix and Ruddiman, 1984). This might lead to a different estimation of the MIS 13 ice sheet volume.

However, with our equilibrium simulations, we gain insights into what the effects of different orbital configurations on climate change and the ice sheet evolution are. We deduce the possible regions which are favorable for ice sheet buildup during a glacial inception.

6.7 CONCLUSIONS

In this chapter, we investigated climate conditions with three typical orbital configurations during MIS 13 using a coupled ice sheet-climate model (at 495 kyr BP, 506 kyr BP and 517 kyr BP). The boreal summer insolation at 65°N at 495 kyr BP is similar to PI condition, but with

lower greenhouse gas values. This causes more ice sheet buildup over polar islands and high elevation mountains. The boreal summer at 506 kyr BP was at perihelion, while for the other two time slices it was at aphelion. The obliquity at 517 kyr BP was the lowest, while was the highest at 495 kyr BP. When boreal summer is at perihelion, the seasonal cycle is enlarged. This leads to a much warmer Northern Hemisphere summer and smaller equilibrium ice sheets. Lower obliquity causes cooling over the polar regions, and is likely favorable for ice sheet buildup around the polar areas and mountains with higher elevations.

In this study, the Cordilleran Ice Sheet develops at the same pace as the summer insolation change at 65 °N during MIS 13. The Cordilleran Ice Sheet is likely more sensitive and has faster response to insolation change than the Laurentide Ice Sheet, Greenland Ice Sheet or Eurasian ice sheets. It indicates that the developing processes of different Northern Hemisphere ice sheets may be different within the Earth system, in terms of interactions with the atmosphere and the ocean under orbital timescales.

The multi-stability of the ice sheets under the same climate forcing should also be considered. Here we only initiate the coupled model from an interglacial state, due to the limitation of the computational resources. However, initiating the model from a glacial state should be conducted in the future. In addition, transient simulations can also be applied for simulating the long duration MIS 13 climate.

SUMMARY AND OUTLOOK

In this thesis, Northern Hemisphere ice sheet evolution during the late Pleistocene is investigated under different background climate conditions, by using a standalone ice sheet model or a coupled ice sheet-climate model. The influence from the atmosphere is the main focus, since Northern Hemisphere ice sheets are primarily land-based. The main conclusions in response to the specific questions in Chapter 1 are as follows:

1. **Was the Northern Hemisphere ice sheet evolution solely consistent with a linear combination of a glacial and interglacial climate state during the last glacial cycle?**

Northern Hemisphere ice sheet evolution during the last glacial cycle is simulated with a first-order approximation of climate forcing (i.e. glacial index method with two extreme climates). Similar to previous studies, the simulated ice sheets match with the general distribution of the geological reconstructions. However, the nonlinear processes cannot be ignored. They likely account for the mismatches between modelling and reconstructions.

2. **How are the effects of upper boundary conditions on Northern Hemisphere ice sheet modelling?**

Atmospheric forcing for the ice sheets is found to be important for ice sheet modelling. Forcing uncertainties have large impact on the simulated ice sheets. Therefore, additional constraints on climate output especially the summer surface air temperature are essential for simulating glacial-interglacial Northern Hemisphere ice sheets.

3. **How are the effects of climate variability on Northern Hemisphere ice sheet mean state?**

In terms of higher frequency climate variability, larger amplitude noise can lead to reduced simulated growth of Northern Hemisphere ice sheets. The nonlinear response of the surface mass balance to temperature are likely the cause for this phenomenon. It results in asymmetric in ice sheet buildup and retreat processes. From this perspective, we propose that DO events may help maintain an intermediate ice sheet state during MIS 4 and 3.

4. **How are the effects of orbital change on Northern Hemisphere ice sheet evolution during Marine Isotope Stage 13?**

The climate of a cold interglacial, MIS 13, is investigated using a coupled ice sheet-climate model with different orbital configurations. The most sensitive areas for ice sheet buildup in response to lower greenhouse gas values are over polar islands and high elevation mountains, e.g. the Cordilleran Ice sheet. Boreal summer at perihelion results in a significant warming during MIS 13 compared to PI especially over Northern Hemisphere mid- and high-latitude continents. This results in a reduction of the simulated ice sheets. Lower obliquity induces cooling over the polar regions, and is therefore favorable for ice sheet growth within these areas.

OUTLOOK

For the ice sheet sensitivity to climate forcing, an alternative ablation scheme to PDD, surface energy balance, could be used for further investigation. Recent work has highlighted the role of ocean forcing in driving glacial ice sheet variability, especially for marine-based ice sheets, for example the Barents-Kara Ice Sheet. However, in our standalone ice sheet simulation, we fixed the ocean forcing and did not incorporate this potential source of climate-driven ice sheet change. Further studies related to the ocean forcing should be included in the future. In addition, better constraints on the ice-substrate interface could be included in the ice sheet modelling.

Using a coupled climate-ice sheet model, we simulated the equilibrium climate state of MIS 13 with different orbital configurations. The simulated ice sheet volume is smaller than that deduced from the benthic $\delta^{18}\text{O}$ records. One possible explanation could be the multi-stability of the ice sheets under the same background condition. In this thesis, we only initiate the coupled model from an interglacial state, due to the limitation of the computational resources. In the future, initiating the model from a glacial state should be conducted for testing the multi-stability. Besides, transient simulations can also be applied for simulating the long duration MIS 13 climate.

REFERENCES

- Abe-Ouchi, A., T. Segawa, and F. Saito (2007). "Climatic Conditions for modelling the Northern Hemisphere ice sheets throughout the ice age cycle." In: *Climate of the Past* 3.3, pp. 423–438. DOI: [10.5194/cp-3-423-2007](https://doi.org/10.5194/cp-3-423-2007). URL: <https://www.clim-past.net/3/423/2007/>.
- Abe-Ouchi, A. et al. (2015). "Ice-sheet configuration in the CMIP5/PMIP3 Last Glacial Maximum experiments." In: *Geoscientific Model Development* 8.11, pp. 3621–3637. DOI: [10.5194/gmd-8-3621-2015](https://doi.org/10.5194/gmd-8-3621-2015). URL: <https://www.geosci-model-dev.net/8/3621/2015/>.
- Abe-Ouchi, Ayako, Fuyuki Saito, Kenji Kawamura, Maureen E Raymo, Jun'ichi Okuno, Kunio Takahashi, and Heinz Blatter (2013). "Insolation-driven 100,000-year glacial cycles and hysteresis of ice-sheet volume." In: *Nature* 500.7461, p. 190.
- Adler, Robert F et al. (2003). "The version-2 global precipitation climatology project (GPCP) monthly precipitation analysis (1979–present)." In: *Journal of Hydrometeorology* 4.6, pp. 1147–1167.
- Ahn, Jinho and Edward J Brook (2008). "Atmospheric CO₂ and climate on millennial time scales during the last glacial period." In: *Science* 322.5898, pp. 83–85.
- Albrecht, T., M. Martin, M. Haseloff, R. Winkelmann, and A. Levermann (2011). "Parameterization for subgrid-scale motion of ice-shelf calving fronts." In: *The Cryosphere* 5.1, pp. 35–44. DOI: [10.5194/tc-5-35-2011](https://doi.org/10.5194/tc-5-35-2011). URL: <https://www.the-cryosphere.net/5/35/2011/>.
- Alley, RB, S Anandakrishnan, and P Jung (2001). "Stochastic resonance in the North Atlantic." In: *Paleoceanography and Paleoclimatology* 16.2, pp. 190–198.
- Amante, C and BW Eakins (2009). *ETOPO1 1 Arc-minute global relief model: Procedures, data sources*. Tech. rep. and analysis, Tech. Rept. NESDIS NGDC-24, National Geophysical Data Center, National Oceanic and Atmospheric Administration (NOAA), Boulder, Colorado.
- American Meteorological Society (cited 2019). *Continental glacier*. URL: <http://glossary.ametsoc.org/wiki/continentalglacier>.
- Andersen, Katrine K, N Azuma, J-M Barnola, Matthias Bigler, P Biscaye, N Caillon, J Chappellaz, Henrik Brink Clausen, Dorte Dahl-Jensen, stus Fischer, et al. (2004). "High-resolution record of Northern Hemisphere climate extending into the last interglacial period." In: *Nature* 431.7005, pp. 147–151.
- Andres, Heather J and WR Peltier (2013). "Examining internal and external contributors to Greenland climate variability using CCSM3." In: *Journal of Climate* 26.24, pp. 9745–9773.

- Aschwanden, A., G. Aðalgeirsdóttir, and C. Khroulev (2013). "Hindcasting to measure ice sheet model sensitivity to initial states." In: *The Cryosphere* 7.4, pp. 1083–1093. DOI: [10.5194/tc-7-1083-2013](https://doi.org/10.5194/tc-7-1083-2013). URL: <https://www.the-cryosphere.net/7/1083/2013/>.
- Aschwanden, Andy, Ed Bueler, Constantine Khroulev, and Heinz Blatter (2012). "An enthalpy formulation for glaciers and ice sheets." In: *Journal of Glaciology* 58.209, pp. 441–457. DOI: [10.3189/2012JoG11J088](https://doi.org/10.3189/2012JoG11J088).
- Austermann, Jacqueline, Jerry X Mitrovica, Konstantin Latychev, and Glenn A Milne (2013). "Barbados-based estimate of ice volume at Last Glacial Maximum affected by subducted plate." In: *Nature Geoscience* 6.7, p. 553.
- Banderas, Rubén, Jorge Alvarez-Solas, Alexander Robinson, and Marisa Montoya (2018). "A new approach for simulating the paleo-evolution of the Northern Hemisphere ice sheets." In: *Geoscientific Model Development* 11.6, pp. 2299–2314.
- Bard, Edouard, Bruno Hamelin, and Doriane Delanghe-Sabatier (2010). "Deglacial Meltwater Pulse 1B and Younger Dryas sea levels revisited with boreholes at Tahiti." In: *Science* 327.5970, pp. 1235–1237.
- Barker, Stephen, Gregor Knorr, R. Lawrence Edwards, Frédéric Parrenin, Aaron E. Putnam, Luke C. Skinner, Eric Wolff, and Martin Ziegler (2011). "800,000 Years of Abrupt Climate Variability." In: *Science* 334.6054, pp. 347–351. ISSN: 0036-8075. DOI: [10.1126/science.1203580](https://doi.org/10.1126/science.1203580).
- Bassis, Jeremy N, Sierra V Petersen, and L Mac Cathles (2017). "Heinrich events triggered by ocean forcing and modulated by isostatic adjustment." In: *Nature* 542.7641, p. 332.
- Bauer, E. and A. Ganopolski (2017). "Comparison of surface mass balance of ice sheets simulated by positive-degree-day method and energy balance approach." In: *Climate of the Past* 13.7, pp. 819–832. DOI: [10.5194/cp-13-819-2017](https://doi.org/10.5194/cp-13-819-2017). URL: <https://www.clim-past.net/13/819/2017/>.
- Beckmann, A and Hugues Goosse (2003). "A parameterization of ice shelf–ocean interaction for climate models." In: *Ocean modelling* 5.2, pp. 157–170.
- Benzi, Roberto, Giorgio Parisi, Alfonso Sutera, and Angelo Vulpiani (1982). "Stochastic resonance in climatic change." In: *Tellus* 34.1, pp. 10–16.
- Berg, Willem Jan Van de, Michiel Van Den Broeke, Janneke Ettema, Erik Van Meijgaard, and Frank Kaspar (2011). "Significant contribution of insolation to Eemian melting of the Greenland ice sheet." In: *Nature Geoscience* 4.10, p. 679.
- Berger, AndréL (1978). "Long-term variations of daily insolation and Quaternary climatic changes." In: *Journal of the Atmospheric Sciences* 35.12, pp. 2362–2367.

- Bond, Gerard C and Rusty Lotti (1995). "Iceberg discharges into the North Atlantic on millennial time scales during the last glaciation." In: *Science* 267.5200, pp. 1005–1010.
- Bond, Gerard C, Wallace Broecker, Sigfus Johnsen, Jerry McManus, Laurent Labeyrie, Jean Jouzel, and Georges Bonani (1993). "Correlations between climate records from North Atlantic sediments and Greenland ice." In: *Nature* 365.6442, p. 143.
- Braconnot, Pascale, Sandy P Harrison, Masa Kageyama, Patrick J Bartlein, Valerie Masson-Delmotte, Ayako Abe-Ouchi, Bette Otto-Bliesner, and Yan Zhao (2012). "Evaluation of climate models using palaeoclimatic data." In: *Nature Climate Change* 2.6, pp. 417–424.
- Brady, Esther C, Bette L Otto-Bliesner, Jennifer E Kay, and Nan Rosenbloom (2013). "Sensitivity to glacial forcing in the CCSM4." In: *Journal of Climate* 26.6, pp. 1901–1925.
- Broecker, Wallace S (1994). "Massive iceberg discharges as triggers for global climate change." In: *Nature* 372.6505, p. 421.
- Bryson, Reid A., Wayne M. Wendland, Jack D. Ives, and John T. Andrews (1969). "Radiocarbon Isochrones on the Disintegration of the Laurentide Ice Sheet." In: *Arctic and Alpine Research* 1.1, pp. 1–13. DOI: [10.1080/00040851.1969.12003535](https://doi.org/10.1080/00040851.1969.12003535). eprint: <https://www.tandfonline.com/doi/pdf/10.1080/00040851.1969.12003535>. URL: <https://www.tandfonline.com/doi/abs/10.1080/00040851.1969.12003535>.
- Budich, Reinhard G, Marco A Giorgetta, Johann H Jungclaus, René Redler, and Christian H Reick (2010). "The MPI-M Millennium Earth System Model: an assembling guide for the COSMOS configuration." In:
- Bueler, ED, Craig S Lingle, and Jed Brown (2007). "Fast computation of a viscoelastic deformable Earth model for ice-sheet simulations." In: *Annals of Glaciology* 46.1, pp. 97–105.
- Bueler, Ed and Jed Brown (2009). "Shallow shelf approximation as a "sliding law" in a thermomechanically coupled ice sheet model." In: *Journal of Geophysical Research: Solid Earth* 114, pp. 1–21. DOI: [10.1029/2008JF001179](https://doi.org/10.1029/2008JF001179).
- Buizert, Christo, Vasileios Gkinis, Jeffrey P Severinghaus, Feng He, Benoit S Lecavalier, Philippe Kindler, Markus Leuenberger, Anders E Carlson, Bo Vinther, Valérie Masson-Delmotte, et al. (2014). "Greenland temperature response to climate forcing during the last deglaciation." In: *Science* 345.6201, pp. 1177–1180.
- Calov, Reinhard and Andrey Ganopolski (2005). "Multistability and hysteresis in the climate-cryosphere system under orbital forcing." In: *Geophysical research letters* 32.21.
- Calov, Reinhard and Ralf Greve (2005). "A semi-analytical solution for the positive degree-day model with stochastic temperature variations." In: *Journal of Glaciology* 51.172, pp. 173–175.

- Carlson, Anders E. and Peter U. Clark (2012). "Ice sheet sources of sea level rise and freshwater discharge during the last deglaciation." In: *Reviews of Geophysics* 50.4. DOI: [10.1029/2011RG000371](https://doi.org/10.1029/2011RG000371). eprint: <https://agupubs.onlinelibrary.wiley.com/doi/pdf/10.1029/2011RG000371>. URL: <https://agupubs.onlinelibrary.wiley.com/doi/abs/10.1029/2011RG000371>.
- Carlson, Anders E, Lev Tarasov, and Tamara Pico (2018). "Rapid Laurentide ice-sheet advance towards southern last glacial maximum limit during marine isotope stage 3." In: *Quaternary Science Reviews* 196, pp. 118–123.
- Cessi, Paola (1994). "A Simple Box Model of Stochastically Forced Thermohaline Flow." In: *Journal of Physical Oceanography* 24.9, pp. 1911–1920. DOI: [10.1175/1520-0485\(1994\)024<1911:ASBMOS>2.0.CO;2](https://doi.org/10.1175/1520-0485(1994)024<1911:ASBMOS>2.0.CO;2).
- Chappell, John (2002). "Sea level changes forced ice breakouts in the Last Glacial cycle: new results from coral terraces." In: *Quaternary Science Reviews* 21.10, pp. 1229–1240.
- Charbit, S., C. Ritz, G. Philippon, V. Peyaud, and M. Kageyama (2007). "Numerical reconstructions of the Northern Hemisphere ice sheets through the last glacial-interglacial cycle." In: *Climate of the Past* 3.1, pp. 15–37. DOI: [10.5194/cp-3-15-2007](https://doi.org/10.5194/cp-3-15-2007). URL: <https://www.clim-past.net/3/15/2007/>.
- Charbit, Sylvie, Catherine Ritz, and Gilles Ramstein (2002). "Simulations of Northern Hemisphere ice-sheet retreat:: sensitivity to physical mechanisms involved during the Last Deglaciation." In: *Quaternary Science Reviews* 21.1, pp. 243–265.
- Charbit, Sylvie, Masa Kageyama, Didier Roche, Catherine Ritz, and Gilles Ramstein (2005). "Investigating the mechanisms leading to the deglaciation of past continental Northern Hemisphere ice sheets with the CLIMBER–GREMLINS coupled model." In: *Global and Planetary Change* 48.4, pp. 253–273.
- Clark, Peter U, Richard B Alley, and David Pollard (1999). "Northern Hemisphere ice-sheet influences on global climate change." In: *Science* 286.5442, pp. 1104–1111.
- Clark, Peter U., Shawn J. Marshall, Garry K. C. Clarke, Steven W. Hostetler, Joseph M. Licciardi, and James T. Teller (2001). "Freshwater Forcing of Abrupt Climate Change During the Last Glaciation." In: *Science* 293.5528, pp. 283–287. ISSN: 0036-8075. DOI: [10.1126/science.1062517](https://doi.org/10.1126/science.1062517).
- Clark, Peter U, Arthur S Dyke, Jeremy D Shakun, Anders E Carlson, Jorie Clark, Barbara Wohlfarth, Jerry X Mitrovica, Steven W Hostetler, and A Marshall McCabe (2009). "The Last Glacial Maximum." In: *Science* 325.5941, pp. 710–714.
- Clarke, Garry KC (2005). "Subglacial processes." In: *Annu. Rev. Earth Planet. Sci.* 33, pp. 247–276.
- Claussen, M. et al. (2002). "Earth system models of intermediate complexity: closing the gap in the spectrum of climate system mod-

- els." In: *Climate Dynamics* 18.7, pp. 579–586. ISSN: 1432-0894. DOI: [10.1007/s00382-001-0200-1](https://doi.org/10.1007/s00382-001-0200-1). URL: <https://doi.org/10.1007/s00382-001-0200-1>.
- Colgan, William, Aleah Sommers, Harihar Rajaram, Waleed Abdalati, and Joel Frahm (2015). "Considering thermal-viscous collapse of the Greenland ice sheet." In: *Earth's Future* 3.7, pp. 252–267. DOI: [10.1002/2015EF000301](https://doi.org/10.1002/2015EF000301). eprint: <https://agupubs.onlinelibrary.wiley.com/doi/pdf/10.1002/2015EF000301>. URL: <https://agupubs.onlinelibrary.wiley.com/doi/abs/10.1002/2015EF000301>.
- Cuffey, Kurt M and William Stanley Bryce Paterson (2010). *The physics of glaciers*. Academic Press.
- Cuzzone, Joshua K, Peter U Clark, Anders E Carlson, David J Ullman, Vincent R Rinterknecht, Glenn A Milne, Juha-Pekka Lunkka, Barbara Wohlfarth, Shaun A Marcott, and Marc Caffee (2016). "Final deglaciation of the Scandinavian Ice Sheet and implications for the Holocene global sea-level budget." In: *Earth and Planetary Science Letters* 448, pp. 34–41.
- Dällenbach, A, T Blunier, J Flückiger, B Stauffer, J Chappellaz, and D Raynaud (2000). "Changes in the atmospheric CH₄ gradient between Greenland and Antarctica during the Last Glacial and the transition to the Holocene." In: *Geophysical Research Letters* 27.7, pp. 1005–1008.
- Dalton, April S, Sarah A Finkelstein, Peter J Barnett, and Steven L Forman (2016). "Constraining the Late Pleistocene history of the Laurentide Ice Sheet by dating the Missinaibi Formation, Hudson Bay Lowlands, Canada." In: *Quaternary Science Reviews* 146, pp. 288–299.
- Dalton, April S, Sarah A Finkelstein, Steven L Forman, Peter J Barnett, Tamara Pico, and Jerry X Mitrovica (2019). "Was the Laurentide Ice Sheet significantly reduced during Marine Isotope Stage 3?" In: *Geology* 47.2, pp. 111–114.
- Danilov, Sergey, Gennady Kivman, and Jens Schröter (2004). "A finite-element ocean model: principles and evaluation." In: *Ocean Modelling* 6.2, pp. 125–150.
- Dansgaard, W et al. (1993). "Evidence for general instability of past climate from a 250-kyr ice-core record." In: *Nature* 364.6434, pp. 218–220. ISSN: 1476-4687. DOI: [10.1038/364218a0](https://doi.org/10.1038/364218a0). URL: <https://doi.org/10.1038/364218a0>.
- Davies, J Huw (2013). "Global map of solid Earth surface heat flow." In: *Geochemistry, Geophysics, Geosystems* 14.10, pp. 4608–4622.
- Dima, M, G Lohman, and G Knorr (2018). "North Atlantic versus Global Control on Dansgaard-Oeschger Events." In: *Geophysical Research Letters*.
- Ditlevsen, Peter D, Katrine Krogh Andersen, and Anders Svensson (2007). "The DO-climate events are probably noise induced: statistical investigation of the claimed 1470 years cycle." In: *Climate of the Past* 3.1, pp. 129–134.

- Dolan, A. M. et al. (2015). "Using results from the PlioMIP ensemble to investigate the Greenland Ice Sheet during the mid-Pliocene Warm Period." In: *Climate of the Past* 11.3, pp. 403–424. DOI: [10.5194/cp-11-403-2015](https://doi.org/10.5194/cp-11-403-2015). URL: <https://www.clim-past.net/11/403/2015/>.
- Dyke, Arthur S (2004). "An outline of North American deglaciation with emphasis on central and northern Canada." In: *Developments in Quaternary Sciences* 2, pp. 373–424.
- Dyke, Arthur and Victor Prest (1987). "Late Wisconsinan and Holocene History of the Laurentide Ice Sheet." In: *Géographie physique et Quaternaire* 41.2, pp. 237–263. DOI: <https://doi.org/10.7202/032681ar>.
- EPICA Community Members (2006). "One-to-one coupling of glacial climate variability in Greenland and Antarctica." In: *Nature* 444.7116, pp. 195–199.
- Fettweis, X. (2007). "Reconstruction of the 1979–2006 Greenland ice sheet surface mass balance using the regional climate model MAR." In: *The Cryosphere* 1.1, pp. 21–40. DOI: [10.5194/tc-1-21-2007](https://doi.org/10.5194/tc-1-21-2007). URL: <https://www.the-cryosphere.net/1/21/2007/>.
- Fischer, N. and J. H. Jungclauss (2011). "Evolution of the seasonal temperature cycle in a transient Holocene simulation: orbital forcing and sea-ice." In: *Climate of the Past* 7.4, pp. 1139–1148. DOI: [10.5194/cp-7-1139-2011](https://doi.org/10.5194/cp-7-1139-2011). URL: <https://www.clim-past.net/7/1139/2011/>.
- Flückiger, J., A. Dällenbach, T. Blunier, B. Stauffer, T. F. Stocker, D. Raynaud, and J.-M. Barnola (1999). "Variations in Atmospheric N₂O Concentration During Abrupt Climatic Changes." In: *Science* 285.5425, pp. 227–230. ISSN: 0036-8075. DOI: [10.1126/science.285.5425.227](https://doi.org/10.1126/science.285.5425.227). URL: <http://science.sciencemag.org/content/285/5425/227>.
- Frieler, Katja, Peter U Clark, Feng He, Christo Buizert, Ronja Reese, Stefan RM Ligtenberg, Michiel R Van Den Broeke, Ricarda Winkelmann, and Anders Levermann (2015). "Consistent evidence of increasing Antarctic accumulation with warming." In: *Nature Climate Change* 5.4, p. 348.
- Fyke, J. G., A. J. Weaver, D. Pollard, M. Eby, L. Carter, and A. Mackintosh (2011). "A new coupled ice sheet/climate model: description and sensitivity to model physics under Eemian, Last Glacial Maximum, late Holocene and modern climate conditions." In: *Geoscientific Model Development* 4.1, pp. 117–136. DOI: [10.5194/gmd-4-117-2011](https://doi.org/10.5194/gmd-4-117-2011). URL: <https://www.geosci-model-dev.net/4/117/2011/>.
- Fyke, Jeremy, Michael Eby, Andrew Mackintosh, and Andrew Weaver (2014). "Impact of climate sensitivity and polar amplification on projections of Greenland Ice Sheet loss." In: *Climate Dynamics* 43.7, pp. 2249–2260. ISSN: 1432-0894. DOI: [10.1007/s00382-014-2050-7](https://doi.org/10.1007/s00382-014-2050-7). URL: <https://doi.org/10.1007/s00382-014-2050-7>.
- Gallée, H., J. P. Van Ypersele, T. Fichefet, I. Marsiat, C. Tricot, and A. Berger (1992). "Simulation of the last glacial cycle by a coupled, sec-

- torially averaged climate-ice sheet model: 2. Response to insolation and CO₂ variations." In: *Journal of Geophysical Research: Atmospheres* 97.D14, pp. 15713–15740. DOI: [10.1029/92JD01256](https://doi.org/10.1029/92JD01256). eprint: <https://agupubs.onlinelibrary.wiley.com/doi/pdf/10.1029/92JD01256>. URL: <https://agupubs.onlinelibrary.wiley.com/doi/abs/10.1029/92JD01256>.
- Ganopolski, A., R. Calov, and M. Claussen (2010). "Simulation of the last glacial cycle with a coupled climate ice-sheet model of intermediate complexity." In: *Climate of the Past* 6.2, pp. 229–244. DOI: [10.5194/cp-6-229-2010](https://doi.org/10.5194/cp-6-229-2010). URL: <https://www.clim-past.net/6/229/2010/>.
- Ganopolski, Andrey and Stefan Rahmstorf (2001). "Rapid changes of glacial climate simulated in a coupled climate model." In: *Nature* 409.6817, p. 153.
- (2002). "Abrupt glacial climate changes due to stochastic resonance." In: *Physical Review Letters* 88.3, p. 038501.
- Giorgetta, Marco A. et al. (2013). "Climate and carbon cycle changes from 1850 to 2100 in MPI-ESM simulations for the Coupled Model Intercomparison Project phase 5." In: *Journal of Advances in Modeling Earth Systems* 5.3, pp. 572–597. ISSN: 1942-2466. DOI: [10.1002/jame.20038](https://doi.org/10.1002/jame.20038). URL: <http://dx.doi.org/10.1002/jame.20038>.
- Glen, JW (1952). "Experiments on the deformation of ice." In: *Journal of Glaciology* 2.12, pp. 111–114.
- Gong, Xun, Gregor Knorr, Gerrit Lohmann, and Xu Zhang (2013). "Dependence of abrupt Atlantic meridional ocean circulation changes on climate background states." In: *Geophysical Research Letters* 40.14, pp. 3698–3704. DOI: [10.1002/grl.50701](https://doi.org/10.1002/grl.50701). eprint: <https://agupubs.onlinelibrary.wiley.com/doi/pdf/10.1002/grl.50701>. URL: <https://agupubs.onlinelibrary.wiley.com/doi/abs/10.1002/grl.50701>.
- Gowan, E. J., L. Niu, G. Knorr, and G. Lohmann (2019). "Geology datasets in North America, Greenland and surrounding areas for use with ice sheet models." In: *Earth System Science Data* 11.1, pp. 375–391. DOI: [10.5194/essd-11-375-2019](https://doi.org/10.5194/essd-11-375-2019). URL: <https://www.earth-syst-sci-data.net/11/375/2019/>.
- Gowan, Evan J, Paul Tregoning, Anthony Purcell, Jean-Philippe Montillet, and Simon McClusky (2016). "A model of the western Laurentide Ice Sheet, using observations of glacial isostatic adjustment." In: *Quaternary Science Reviews* 139, pp. 1–16.
- Greve, Ralf, Karl-Heinz Wyrwoll, and Anton Eisenhauer (1999). "Deglaciation of the Northern Hemisphere at the onset of the Eemian and Holocene." In: *Annals of Glaciology* 28.1, pp. 1–8.
- Hays, J. D., John Imbrie, and N. J. Shackleton (1976). "Variations in the Earth's Orbit: Pacemaker of the Ice Ages." In: *Science* 194.4270, pp. 1121–1132. ISSN: 0036-8075. DOI: [10.1126/science.194.4270.1121](https://doi.org/10.1126/science.194.4270.1121). eprint: <http://science.sciencemag.org/content/194/4270/>

- 1121.full.pdf. URL: <http://science.sciencemag.org/content/194/4270/1121>.
- Hönisch, Bärbel, N Gary Hemming, David Archer, Mark Siddall, and Jerry F McManus (2009). "Atmospheric carbon dioxide concentration across the mid-Pleistocene transition." In: *Science* 324.5934, pp. 1551–1554.
- Huber, Christof, Markus Leuenberger, Renato Spahni, Jacqueline Flückiger, Jakob Schwander, Thomas F Stocker, Sigfus Johnsen, Amaelle Landais, and Jean Jouzel (2006). "Isotope calibrated Greenland temperature record over Marine Isotope Stage 3 and its relation to CH₄." In: *Earth and Planetary Science Letters* 243.3-4, pp. 504–519.
- Hughes, Anna LC, Richard Gyllencreutz, Øystein S Lohne, Jan Mangerud, and John Inge Svendsen (2016). "The last Eurasian ice sheets—a chronological database and time-slice reconstruction, DATED-1." In: *Boreas* 45.1, pp. 1–45.
- Huybers, Peter (2011). "Combined obliquity and precession pacing of late Pleistocene deglaciations." In: *Nature* 480.7376, pp. 229–232.
- Huybers, Peter and Carl Wunsch (2005). "Obliquity pacing of the late Pleistocene glacial terminations." In: *Nature* 434.7032, pp. 491–494.
- Huybrechts, Philippe (2002). "Sea-level changes at the LGM from ice-dynamic reconstructions of the Greenland and Antarctic ice sheets during the glacial cycles." In: *Quaternary Science Reviews* 21.1-3, pp. 203–231.
- Imbrie, J. et al. (1993). "On the structure and origin of major glaciation cycles 2. The 100,000-year cycle." In: *Paleoceanography* 8.6, pp. 699–735. ISSN: 1944-9186. DOI: [10.1029/93PA02751](https://doi.org/10.1029/93PA02751). URL: <http://dx.doi.org/10.1029/93PA02751>.
- Jouzel, Jean, Valérie Masson-Delmotte, Olivier Cattani, Gabrielle Dreyfus, Sonia Falourd, Georg Hoffmann, Bénédicte Minster, J Nouet, Jean-Marc Barnola, Jérôme Chappellaz, et al. (2007). "Orbital and millennial Antarctic climate variability over the past 800,000 years." In: *science* 317.5839, pp. 793–796.
- Jungclauss, J. H. et al. (2010). "Climate and carbon-cycle variability over the last millennium." In: *Climate of the Past* 6.5, pp. 723–737. DOI: [10.5194/cp-6-723-2010](https://doi.org/10.5194/cp-6-723-2010). URL: <https://www.clim-past.net/6/723/2010/>.
- Jungclauss, JH, Nils Fischer, Helmuth Haak, K Lohmann, J Marotzke, D Matei, U Mikolajewicz, D Notz, and JS Storch (2013). "Characteristics of the ocean simulations in the Max Planck Institute Ocean Model (MPIOM) the ocean component of the MPI-Earth system model." In: *Journal of Advances in Modeling Earth Systems* 5.2, pp. 422–446.
- Kageyama, Masa et al. (2013a). "Mid-Holocene and Last Glacial Maximum climate simulations with the IPSL model—part I: comparing IPSL_CM5A to IPSL_CM4." In: *Climate Dynamics* 40.9, pp. 2447–2468. ISSN: 1432-0894. DOI: [10.1007/s00382-012-1488-8](https://doi.org/10.1007/s00382-012-1488-8). URL: <https://doi.org/10.1007/s00382-012-1488-8>.

- Kageyama, Masa et al. (2013b). "Mid-Holocene and Last Glacial Maximum climate simulations with the IPSL model: part II: model-data comparisons." In: *Climate Dynamics* 40.9, pp. 2469–2495. ISSN: 1432-0894. DOI: [10.1007/s00382-012-1499-5](https://doi.org/10.1007/s00382-012-1499-5). URL: <https://doi.org/10.1007/s00382-012-1499-5>.
- Kalnay, Eugenia et al. (1996). "The NCEP/NCAR 40-year reanalysis project." In: *Bulletin of the American Meteorological Society* 77.3, pp. 437–471.
- Kleman, Johan, Krister Jansson, Hernán De Angelis, Arjen P Stroeven, Clas Hättestrand, Göran Alm, and Neil Glasser (2010). "North American Ice Sheet build-up during the last glacial cycle, 115–21kyr." In: *Quaternary Science Reviews* 29.17, pp. 2036–2051.
- Knorr, G., M. Butzin, A. Micheels, and G. Lohmann (2011). "A warm Miocene climate at low atmospheric CO₂ levels." In: *Geophysical Research Letters* 38.20. DOI: [10.1029/2011GL048873](https://doi.org/10.1029/2011GL048873). eprint: <https://agupubs.onlinelibrary.wiley.com/doi/pdf/10.1029/2011GL048873>. URL: <https://agupubs.onlinelibrary.wiley.com/doi/abs/10.1029/2011GL048873>.
- Knorr, Gregor and Gerrit Lohmann (2014). "Climate warming during Antarctic ice sheet expansion at the Middle Miocene transition." In: *Nature Geoscience* 7.5, p. 376.
- Krebs-Kanzow, Uta, Paul Gierz, and Gerrit Lohmann (2018a). "Brief communication: An ice surface melt scheme including the diurnal cycle of solar radiation." In: *The Cryosphere* 12.12, pp. 3923–3930.
- (2018b). "Estimating Greenland surface melt is hampered by melt induced dampening of temperature variability." In: *Journal of Glaciology* 64.244, pp. 227–235.
- Lambeck, Kurt and John Chappell (2001). "Sea level change through the last glacial cycle." In: *Science* 292.5517, pp. 679–686.
- Lambeck, Kurt, H el ene Rouby, Anthony Purcell, Yiyi Sun, and Malcolm Sambridge (2014). "Sea level and global ice volumes from the Last Glacial Maximum to the Holocene." In: *Proceedings of the National Academy of Sciences* 111.43, pp. 15296–15303.
- Levermann, A., T. Albrecht, R. Winkelmann, M. A. Martin, M. Haseloff, and I. Joughin (2012). "Kinematic first-order calving law implies potential for abrupt ice-shelf retreat." In: *The Cryosphere* 6.2, pp. 273–286. DOI: [10.5194/tc-6-273-2012](https://doi.org/10.5194/tc-6-273-2012). URL: <https://www.the-cryosphere.net/6/273/2012/>.
- Liakka, Johan, Johan Nilsson, and Marcus L ofverstr om (2012). "Interactions between stationary waves and ice sheets: linear versus non-linear atmospheric response." In: *Climate Dynamics* 38.5, pp. 1249–1262. ISSN: 1432-0894. DOI: [10.1007/s00382-011-1004-6](https://doi.org/10.1007/s00382-011-1004-6). URL: <https://doi.org/10.1007/s00382-011-1004-6>.
- Lingle, Craig S and James A Clark (1985). "A numerical model of interactions between a marine ice sheet and the solid earth: Application

- to a West Antarctic ice stream." In: *Journal of Geophysical Research: Oceans* 90.C1, pp. 1100–1114.
- Lisiecki, Lorraine E (2010). "Links between eccentricity forcing and the 100,000-year glacial cycle." In: *Nature Geoscience* 3.5, pp. 349–352.
- Lisiecki, Lorraine E and Maureen E Raymo (2005). "A Pliocene-Pleistocene stack of 57 globally distributed benthic $\delta^{18}\text{O}$ records." In: *Paleoceanography* 20.1.
- Lliboutry, L and P Duval (1985). "Various isotropic and anisotropic ices found in glaciers and polar ice caps and their corresponding rheologies." In: *Annales geophysicae*. Vol. 3. 2. Gauthier-Villars, pp. 207–224.
- Löfverström, Marcus, Rodrigo Caballero, Johan Nilsson, and Johan Kleman (2014). "Evolution of the large-scale atmospheric circulation in response to changing ice sheets over the last glacial cycle." In: *Climate of the Past* 10.4, pp. 1453–1471. DOI: [10.5194/cp-10-1453-2014](https://doi.org/10.5194/cp-10-1453-2014). URL: <https://www.clim-past.net/10/1453/2014/>.
- Löfverström, Marcus, Johan Liakka, and Johan Kleman (2015). "The North American Cordillera—An impediment to growing the continent-wide Laurentide ice sheet." In: *Journal of Climate* 28.23, pp. 9433–9450.
- Loulergue, Laetitia, Adrian Schilt, Renato Spahni, Valérie Masson-Delmotte, Thomas Blunier, Bénédicte Lemieux, Jean-Marc Barnola, Dominique Raynaud, Thomas F Stocker, and Jérôme Chappellaz (2008). "Orbital and millennial-scale features of atmospheric CH₄ over the past 800,000 years." In: *Nature* 453.7193, p. 383.
- Man, Wenmin, Tianjun Zhou, and Johann H Jungclaus (2014). "Effects of large volcanic eruptions on global summer climate and East Asian monsoon changes during the last millennium: Analysis of MPI-ESM simulations." In: *Journal of Climate* 27.19, pp. 7394–7409.
- Margold, Martin, Chris R Stokes, and Chris D Clark (2015). "Ice streams in the Laurentide Ice Sheet: Identification, characteristics and comparison to modern ice sheets." In: *Earth-Science Reviews* 143, pp. 117–146.
- Marshall, Shawn J, Lev Tarasov, Garry KC Clarke, and W Richard Peltier (2000). "Glaciological reconstruction of the Laurentide Ice Sheet: physical processes and modelling challenges." In: *Canadian Journal of Earth Sciences* 37.5, pp. 769–793.
- Marshall, Shawn J, Thomas S James, and Garry KC Clarke (2002). "North American ice sheet reconstructions at the Last Glacial Maximum." In: *Quaternary Science Reviews* 21.1, pp. 175–192.
- Martin, M. A., R. Winkelmann, M. Haseloff, T. Albrecht, E. Bueller, C. Khroulev, and A. Levermann (2011). "The Potsdam Parallel Ice Sheet Model (PISM-PIK)—Part 2: Dynamic equilibrium simulation of the Antarctic ice sheet." In: *The Cryosphere* 5.3, pp. 727–740. DOI: [10.5194/tc-5-727-2011](https://doi.org/10.5194/tc-5-727-2011). URL: <https://www.the-cryosphere.net/5/727/2011/>.

- Meinshausen, M, SJ Smith, K Calvin, JS Daniel, MLT Kainuma, JF Lamarque, K Matsumoto, SA Montzka, S Raper, K Riahi, et al. (2011). "The Paleoclimate Modeling Intercomparison Project contribution to CMIP5." In: *CLIVAR Exchanges No. 56* 16.2, p. 15.
- Mikkelsen, T. B., A. Grinsted, and Peter D Ditlevsen (2018). "Influence of temperature fluctuations on equilibrium ice sheet volume." In: *The Cryosphere* 12.1, pp. 39–47. DOI: [10.5194/tc-12-39-2018](https://doi.org/10.5194/tc-12-39-2018). URL: <https://www.the-cryosphere.net/12/39/2018/>.
- Milankovitch, M. (1941). *Kanon der Erdbestrahlung und seine Anwendung auf das Eiszeitproblem*. Königlich Serbische Akademie. URL: <https://books.google.de/books?id=JbfZjgEACAAJ>.
- Mix, Alan C and William F Ruddiman (1984). "Oxygen-Isotope Analyses and Pleistocene Ice Volumes 1." In: *Quaternary Research* 21.1, pp. 1–20.
- Monnin, Eric, Andreas Indermühle, André Dällenbach, Jacqueline Flückiger, Bernhard Stauffer, Thomas F. Stocker, Dominique Raynaud, and Jean-Marc Barnola (2001). "Atmospheric CO₂ Concentrations over the Last Glacial Termination." In: *Science* 291.5501, pp. 112–114. ISSN: 0036-8075. DOI: [10.1126/science.291.5501.112](https://doi.org/10.1126/science.291.5501.112). eprint: <http://science.sciencemag.org/content/291/5501/112.full.pdf>. URL: <http://science.sciencemag.org/content/291/5501/112>.
- Mote, Thomas L. (2003). "Estimation of runoff rates, mass balance, and elevation changes on the Greenland ice sheet from passive microwave observations." In: *Journal of Geophysical Research: Atmospheres* 108.D2. DOI: [10.1029/2001JD002032](https://doi.org/10.1029/2001JD002032). eprint: <https://agupubs.onlinelibrary.wiley.com/doi/pdf/10.1029/2001JD002032>. URL: <https://agupubs.onlinelibrary.wiley.com/doi/abs/10.1029/2001JD002032>.
- Muri, Helene, André Berger, Qiuzhen Yin, Aurore Voldoire, David Salas Y Mélia, and Suchithra Sundaram (2012). "SST and ice sheet impacts on the MIS-13 climate." In: *Climate dynamics* 39.7-8, pp. 1739–1761.
- Muri, Helene, André Berger, Qiuzhen Yin, Mehdi Pasha Karami, and Pierre-Yves Barriat (2013). "The climate of the MIS-13 interglacial according to HadCM3." In: *Journal of Climate* 26.23, pp. 9696–9712.
- Niessen, Frank, Jong Kuk Hong, Anne Hegewald, Jens Matthiessen, Rüdiger Stein, Hyoungjun Kim, Sookwan Kim, Laura Jensen, Wilfried Jokat, Seung-Il Nam, et al. (2013). "Repeated Pleistocene glaciation of the East Siberian continental margin." In: *Nature Geoscience* 6.10, p. 842.
- Niu, L., G. Lohmann, and E. J. Gowan (2019a). "Climate Noise Influences Ice Sheet Mean State." In: *Geophysical Research Letters* 46. DOI: [10.1029/2019GL083717](https://doi.org/10.1029/2019GL083717).
- Niu, L., G. Lohmann, S. Hinck, E. J. Gowan, and U. Krebs-Kanzow (2019b). "The sensitivity of Northern Hemisphere ice sheets to atmo-

- spheric forcing during the last glacial cycle using PMIP₃ models." In: *Journal of Glaciology* 65.252, pp. 645–661. DOI: [10.1017/jog.2019.42](https://doi.org/10.1017/jog.2019.42).
- Niu, L., P. Gierz, E. J. Gowan, and G. Lohmann (in prep). "Instability of the Cordilleran Ice Sheet under different orbital forcing." In: *To be submitted*.
- Nye, John F (1953). "The flow law of ice from measurements in glacier tunnels, laboratory experiments and the Jungfraufirn borehole experiment." In: *Proceedings of the Royal Society of London A: Mathematical, Physical and Engineering Sciences*. Vol. 219. 1139. The Royal Society, pp. 477–489.
- Ohgaito, R., T. Sueyoshi, A. Abe-Ouchi, T. Hajima, S. Watanabe, H.-J. Kim, A. Yamamoto, and M. Kawamiya (2013). "Can an Earth System Model simulate better climate change at mid-Holocene than an AOGCM? A comparison study of MIROC-ESM and MIROC₃." In: *Climate of the Past* 9.4, pp. 1519–1542. DOI: [10.5194/cp-9-1519-2013](https://doi.org/10.5194/cp-9-1519-2013). URL: <https://www.clim-past.net/9/1519/2013/>.
- Paterson, WSB (1994). *The Physics of Glaciers*. Butterworth-Heinemann.
- Paterson, WSB and WF Budd (1982). "Flow parameters for ice sheet modeling." In: *Cold Regions Science and Technology* 6.2, pp. 175–177.
- Pausata, Francesco SR and Marcus Löffverström (2015). "On the enigmatic similarity in Greenland $\delta^{18}\text{O}$ between the Oldest and Younger Dryas." In: *Geophysical Research Letters* 42.23, pp. 10–470.
- Petersen, S. V., D. P. Schrag, and P. U. Clark (2013). "A new mechanism for Dansgaard-Oeschger cycles." In: *Paleoceanography* 28.1, pp. 24–30. DOI: [10.1029/2012PA002364](https://doi.org/10.1029/2012PA002364).
- Pollard, David (2000). "Comparisons of ice-sheet surface mass budgets from Paleoclimate Modeling Intercomparison Project (PMIP) simulations." In: *Global and Planetary Change* 24.2, pp. 79–106. ISSN: 0921-8181. DOI: [https://doi.org/10.1016/S0921-8181\(99\)00071-5](https://doi.org/10.1016/S0921-8181(99)00071-5). URL: <http://www.sciencedirect.com/science/article/pii/S0921818199000715>.
- (2010). "A retrospective look at coupled ice sheet–climate modeling." In: *Climatic Change* 100.1, pp. 173–194. ISSN: 1573-1480. DOI: [10.1007/s10584-010-9830-9](https://doi.org/10.1007/s10584-010-9830-9). URL: <https://doi.org/10.1007/s10584-010-9830-9>.
- Porter, Stephen C (2001). "Chinese loess record of monsoon climate during the last glacial–interglacial cycle." In: *Earth-Science Reviews* 54.1-3, pp. 115–128.
- Prest, Victor Kent. (1968). *Nomenclature of moraines and ice-flow features as applied to the glacial map of Canada [by] V.K. Prest*. English. Dept. of Energy, Mines and Resources [Ottawa], v, 32 p.
- Rackow, T., H. F. Goessling, T. Jung, D. Sidorenko, T. Semmler, D. Barbi, and D. Handorf (2018). "Towards multi-resolution global climate modeling with ECHAM6-FESOM. Part II: climate variability." In: *Climate Dynamics* 50.7, pp. 2369–2394. ISSN: 1432-0894. DOI: [10.1007/](https://doi.org/10.1007/)

- s00382-016-3192-6. URL: <https://doi.org/10.1007/s00382-016-3192-6>.
- Raddatz, TJ, CH Reick, W Knorr, Jens Kattge, E Roeckner, Reiner Schnur, K-G Schnitzler, P Wetzels, and J Jungclaus (2007). "Will the tropical land biosphere dominate the climate-carbon cycle feedback during the twenty-first century?" In: *Climate Dynamics* 29.6, pp. 565–574.
- Rahmstorf, Stefan (1995). "Multiple convection patterns and thermohaline flow in an idealized OGCM." In: *Journal of Climate* 8.12, pp. 3028–3039.
- Reeh, Niels (1989). "Parameterization of melt rate and surface temperature on the Greenland ice sheet." In: *Polarforschung* 59.3, pp. 113–128.
- Rehfeld, Kira, Thomas Münch, Sze Ling Ho, and Thomas Laepple (2018). "Global patterns of declining temperature variability from the Last Glacial Maximum to the Holocene." In: *Nature* 554.7692, p. 356.
- Reusche, Melissa M., Shaun A. Marcott, Elizabeth G. Ceperley, Aaron M. Barth, Edward J. Brook, Alan C. Mix, and Marc W. Caffee (2018). "Early to late Holocene surface exposure ages from two marine-terminating outlet Glaciers in northwest Greenland." In: *Geophysical Research Letters* 45.14, pp. 7028–7039. DOI: [10.1029/2018GL078266](https://doi.org/10.1029/2018GL078266).
- Ritz, Catherine (1997). *EISMINT Intercomparison Experiment: Comparison of existing Greenland models*. URL: <http://homepages.vub.ac.be/~phuybrec/eismint/greenland.html>.
- Robinson, A. and H. Goelzer (2014). "The importance of insolation changes for paleo ice sheet modeling." In: *The Cryosphere* 8.4, pp. 1419–1428. DOI: [10.5194/tc-8-1419-2014](https://doi.org/10.5194/tc-8-1419-2014). URL: <https://www.the-cryosphere.net/8/1419/2014/>.
- Rodgers, Keith B, Sylvie Charbit, Masa Kageyama, Gwenaëlle Philippon, Gilles Ramstein, Catherine Ritz, Jeffrey H Yin, Gerrit Lohmann, Stephan J Lorenz, and Myriam Khodri (2004). "Sensitivity of Northern Hemispheric continental ice sheets to tropical SST during deglaciation." In: *Geophysical Research Letters* 31.2.
- Roe, Gerard H and Richard S Lindzen (2001). "The mutual interaction between continental-scale ice sheets and atmospheric stationary waves." In: *Journal of Climate* 14.7, pp. 1450–1465.
- Roeckner, Erich, G Bäuml, L Bonaventura, Renate Brokopf, Monika Esch, Marco Giorgetta, Stefan Hagemann, Ingo Kirchner, Luis Kornblueh, Elisa Manzini, et al. (2003). "The atmospheric general circulation model ECHAM5. PART I: Model description." In:
- Roeckner, Erich, Renate Brokopf, Monika Esch, Marko Giorgetta, Stefan Hagemann, Luis Kornblueh, Elisa Manzini, Ulrich Schlese, and Uwe Schulzweida (2004). "The atmospheric general circulation model ECHAM5 Part II: Sensitivity of simulated climate to horizontal and vertical resolution." In:

- Rohling, EJ, Gavin L Foster, KM Grant, Gianluca Marino, AP Roberts, Mark E Tamisiea, and Frances Williams (2014). "Sea-level and deep-sea-temperature variability over the past 5.3 million years." In: *Nature* 508.7497, pp. 477–482.
- Ruddiman, William F (2001). *Earth's Climate: past and future*. Macmillan.
- Schaefer, Joerg M, Aaron E Putnam, George H Denton, Michael R Kaplan, Sean Birkel, Alice M Doughty, Sam Kelley, David JA Barrell, Robert C Finkel, Gisela Winckler, et al. (2015). "The southern glacial maximum 65,000 years ago and its unfinished termination." In: *Quaternary Science Reviews* 114, pp. 52–60.
- Schmidt, Gavin A, Max Kelley, Larissa Nazarenko, Reto Ruedy, Gary L Russell, Igor Aleinov, Mike Bauer, Susanne E Bauer, Maharaj K Bhat, Rainer Bleck, et al. (2014). "Configuration and assessment of the GISS ModelE2 contributions to the CMIP5 archive." In: *Journal of Advances in Modeling Earth Systems* 6.1, pp. 141–184.
- Schoof, Christian (2006). "A variational approach to ice stream flow." In: *Journal of Fluid Mechanics* 556, pp. 227–251.
- Schulz, Michael (2002). "On the 1470-year pacing of Dansgaard-Oeschger warm events." In: *Paleoceanography* 17.2, pp. 4–1.
- Seguinot, Julien, Irina Rogozhina, Arjen P Stroeven, Martin Margold, and Johan Kleman (2016). "Numerical simulations of the Cordilleran ice sheet through the last glacial cycle." In: *Cryosphere* 10.2.
- Shackleton, Nicholas J (2000). "The 100,000-year ice-age cycle identified and found to lag temperature, carbon dioxide, and orbital eccentricity." In: *Science* 289.5486, pp. 1897–1902.
- Shao, Zhi-Gang and Peter D Ditlevsen (2016). "Contrasting scaling properties of interglacial and glacial climates." In: *Nature communications* 7, p. 10951.
- Siddall, M., E. J. Rohling, W. G. Thompson, and C. Waelbroeck (2008). "Marine Isotope Stage 3 sea level fluctuations: Data synthesis and new outlook." In: *Reviews of Geophysics* 46.4. DOI: [10.1029/2007RG000226](https://doi.org/10.1029/2007RG000226). eprint: <https://agupubs.onlinelibrary.wiley.com/doi/pdf/10.1029/2007RG000226>. URL: <https://agupubs.onlinelibrary.wiley.com/doi/abs/10.1029/2007RG000226>.
- Sidorenko, D. et al. (2015). "Towards multi-resolution global climate modeling with ECHAM6–FESOM. Part I: model formulation and mean climate." In: *Climate Dynamics* 44.3, pp. 757–780. ISSN: 1432-0894. DOI: [10.1007/s00382-014-2290-6](https://doi.org/10.1007/s00382-014-2290-6). URL: <https://doi.org/10.1007/s00382-014-2290-6>.
- Siegenthaler, Urs, Thomas F Stocker, Eric Monnin, Dieter Lüthi, Jakob Schwander, Bernhard Stauffer, Dominique Raynaud, Jean-Marc Barnola, Hubertus Fischer, Valérie Masson-Delmotte, et al. (2005). "Stable carbon cycle–climate relationship during the late Pleistocene." In: *Science* 310.5752, pp. 1313–1317.

- Spahni, Renato, Jérôme Chappellaz, Thomas F Stocker, Laetitia Loulergue, Gregor Hausammann, Kenji Kawamura, Jacqueline Flückiger, Jakob Schwander, Dominique Raynaud, Valérie Masson-Delmotte, et al. (2005). "Atmospheric methane and nitrous oxide of the late Pleistocene from Antarctic ice cores." In: *Science* 310.5752, pp. 1317–1321.
- Stepanek, C. and G. Lohmann (2012). "Modelling mid-Pliocene climate with COSMOS." In: *Geoscientific Model Development* 5.5, pp. 1221–1243. DOI: [10.5194/gmd-5-1221-2012](https://doi.org/10.5194/gmd-5-1221-2012). URL: <https://www.geosci-model-dev.net/5/1221/2012/>.
- Stevens, Bjorn et al. (2013). "Atmospheric component of the MPI-M Earth System Model: ECHAM6." In: *Journal of Advances in Modeling Earth Systems* 5.2, pp. 146–172. DOI: [10.1002/jame.20015](https://doi.org/10.1002/jame.20015). eprint: <https://agupubs.onlinelibrary.wiley.com/doi/pdf/10.1002/jame.20015>. URL: <https://agupubs.onlinelibrary.wiley.com/doi/abs/10.1002/jame.20015>.
- Stokes, Chris R, Lev Tarasov, and Arthur S Dyke (2012). "Dynamics of the North American Ice Sheet Complex during its inception and build-up to the Last Glacial Maximum." In: *Quaternary Science Reviews* 50, pp. 86–104.
- Stommel, Henry (1961). "Thermohaline convection with two stable regimes of flow." In: *Tellus* 13.2, pp. 224–230.
- Sueyoshi, T. et al. (2013). "Set-up of the PMIP₃ paleoclimate experiments conducted using an Earth system model, MIROC-ESM." In: *Geoscientific Model Development* 6.3, pp. 819–836. DOI: [10.5194/gmd-6-819-2013](https://doi.org/10.5194/gmd-6-819-2013). URL: <https://www.geosci-model-dev.net/6/819/2013/>.
- Svendsen, John Inge, Helena Alexanderson, Valery I Astakhov, Igor Demidov, Julian A Dowdeswell, Svend Funder, Valery Gataullin, Mona Henriksen, Christian Hjort, Michael Houmark-Nielsen, et al. (2004). "Late Quaternary ice sheet history of northern Eurasia." In: *Quaternary Science Reviews* 23.11, pp. 1229–1271.
- Tarasov, L. and W. Richard Peltier (2004). "A geophysically constrained large ensemble analysis of the deglacial history of the North American ice-sheet complex." In: *Quaternary Science Reviews* 23.3, pp. 359–388. ISSN: 0277-3791. DOI: <https://doi.org/10.1016/j.quascirev.2003.08.004>. URL: <http://www.sciencedirect.com/science/article/pii/S0277379103002774>.
- The PISM authors (2016). *PISM, a Parallel Ice Sheet Model*. URL: <http://www.pism-docs.org>.
- Tian, Z. and D. Jiang (2013). "Mid-Holocene ocean and vegetation feedbacks over East Asia." In: *Climate of the Past* 9.5, pp. 2153–2171. DOI: [10.5194/cp-9-2153-2013](https://doi.org/10.5194/cp-9-2153-2013). URL: <https://www.clim-past.net/9/2153/2013/>.

- Timmermann, Axel and Gerrit Lohmann (2000). "Noise-induced transitions in a simplified model of the thermohaline circulation." In: *Journal of Physical Oceanography* 30.8, pp. 1891–1900.
- Tulaczyk, Slawek, W Barclay Kamb, and Hermann F Engelhardt (2000a). "Basal mechanics of Ice Stream B, West Antarctica: 2. Undrained plastic bed model." In: *Journal of Geophysical Research: Solid Earth* 105.B1, pp. 483–494.
- (2000b). "Basal mechanics of ice stream B, West Antarctica: 1. Till mechanics." In: *Journal of Geophysical Research: Solid Earth* 105.B1, pp. 463–481.
- Ullman, D. J., A. N. LeGrande, A. E. Carlson, F. S. Anslow, and J. M. Licciardi (2014). "Assessing the impact of Laurentide Ice Sheet topography on glacial climate." In: *Climate of the Past* 10.2, pp. 487–507. DOI: [10.5194/cp-10-487-2014](https://doi.org/10.5194/cp-10-487-2014). URL: <https://www.clim-past.net/10/487/2014/>.
- Ullman, David J, Anders E Carlson, Faron S Anslow, Allegra N LeGrande, and Joseph M Licciardi (2015). "Laurentide ice-sheet instability during the last deglaciation." In: *Nature Geoscience* 8.7, p. 534.
- Ullman, David J, Anders E Carlson, Steven W Hostetler, Peter U Clark, Joshua Cuzzone, Glenn A Milne, Kelsey Winsor, and Marc Caffee (2016). "Final Laurentide ice-sheet deglaciation and Holocene climate-sea level change." In: *Quaternary Science Reviews* 152, pp. 49–59.
- Valcke, S (2006). *OASIS3 user guide (prism_2-5) CERFACS technical support*. Tech. rep. TR/CMGC/o6/73, PRISM report.
- Van Meerbeeck, C. J., H. Renssen, and D. M. Roche (2009). "How did Marine Isotope Stage 3 and Last Glacial Maximum climates differ? - Perspectives from equilibrium simulations." In: *Climate of the Past* 5.1, pp. 33–51. DOI: [10.5194/cp-5-33-2009](https://doi.org/10.5194/cp-5-33-2009). URL: <https://www.clim-past.net/5/33/2009/>.
- Vettoretti, Guido and W Richard Peltier (2013). "Last Glacial Maximum ice sheet impacts on North Atlantic climate variability: The importance of the sea ice lid." In: *Geophysical Research Letters* 40.24, pp. 6378–6383.
- Voldoire, A. et al. (2013). "The CNRM-CM5.1 global climate model: description and basic evaluation." In: *Climate Dynamics* 40.9, pp. 2091–2121. ISSN: 1432-0894. DOI: [10.1007/s00382-011-1259-y](https://doi.org/10.1007/s00382-011-1259-y). URL: <https://doi.org/10.1007/s00382-011-1259-y>.
- Wang, Q., S. Danilov, D. Sidorenko, R. Timmermann, C. Wekerle, X. Wang, T. Jung, and J. Schröter (2014). "The Finite Element Sea Ice-Ocean Model (FESOM) v.1.4: formulation of an ocean general circulation model." In: *Geoscientific Model Development* 7.2, pp. 663–693. DOI: [10.5194/gmd-7-663-2014](https://doi.org/10.5194/gmd-7-663-2014). URL: <https://www.geosci-model-dev.net/7/663/2014/>.

- Wei, Wei and Gerrit Lohmann (2012). "Simulated Atlantic Multi-decadal Oscillation during the Holocene." In: *Journal of Climate* 25.20, pp. 6989–7002. DOI: [10.1175/JCLI-D-11-00667.1](https://doi.org/10.1175/JCLI-D-11-00667.1). eprint: <https://doi.org/10.1175/JCLI-D-11-00667.1>. URL: <https://doi.org/10.1175/JCLI-D-11-00667.1>.
- Wei, Wei, Gerrit Lohmann, and Mihai Dima (2012). "Distinct Modes of Internal Variability in the Global Meridional Overturning Circulation Associated with the Southern Hemisphere Westerly Winds." In: *Journal of Physical Oceanography* 42.5, pp. 785–801. DOI: [10.1175/JPO-D-11-038.1](https://doi.org/10.1175/JPO-D-11-038.1). eprint: <https://doi.org/10.1175/JPO-D-11-038.1>. URL: <https://doi.org/10.1175/JPO-D-11-038.1>.
- Wetzel, P, H Haak, J Jungclaus, and E Maier-Reimer (2010). *The Max-Planck-Institute global Ocean/Sea-Ice model MPI-OM*. Tech. rep. technical report, Max-Planck-Inst. for Meteorol., Hamburg, Germany.[Available at <http://www.mpimet.mpg.de/en/wissenschaft/modelle/mpiom.html>.]
- Whitehouse, Pippa L, Michael J Bentley, and Anne M Le Brocq (2012). "A deglacial model for Antarctica: geological constraints and glaciological modelling as a basis for a new model of Antarctic glacial isostatic adjustment." In: *Quaternary Science Reviews* 32, pp. 1–24.
- Winkelmann, R., M. A. Martin, M. Haseloff, T. Albrecht, E. Bueler, C. Khroulev, and A. Levermann (2011). "The Potsdam Parallel Ice Sheet Model (PISM-PIK) - Part 1: Model description." In: *The Cryosphere* 5.3, pp. 715–726. DOI: [10.5194/tc-5-715-2011](https://www.the-cryosphere.net/5/715/2011/). URL: <https://www.the-cryosphere.net/5/715/2011/>.
- Woillard, Geneviève M and Willem G Mook (1982). "Carbon-14 dates at Grande Pile: correlation of land and sea chronologies." In: *Science* 215.4529, pp. 159–161.
- Wood, John R, Steven L Forman, David Everton, James Pierson, and Jeaneth Gomez (2010). "Lacustrine sediments in Porter Cave, Central Indiana, USA and possible relation to Laurentide ice sheet marginal positions in the middle and late Wisconsinan." In: *Palaeogeography, Palaeoclimatology, Palaeoecology* 298.3-4, pp. 421–431.
- Yan, Qing, Huijun Wang, Ola M. Johannessen, and Zhongshi Zhang (2014). "Greenland ice sheet contribution to future global sea level rise based on CMIP5 models." In: *Advances in Atmospheric Sciences* 31.1, pp. 8–16. ISSN: 1861-9533. DOI: [10.1007/s00376-013-3002-6](https://doi.org/10.1007/s00376-013-3002-6). URL: <https://doi.org/10.1007/s00376-013-3002-6>.
- Yin, Q. Z. and Z. T. Guo (2008). "Strong summer monsoon during the cool MIS-13." In: *Climate of the Past* 4.1, pp. 29–34. DOI: [10.5194/cp-4-29-2008](https://www.clim-past.net/4/29/2008/). URL: <https://www.clim-past.net/4/29/2008/>.
- Yin, QZ, André Berger, and Michel Crucifix (2009). "Individual and combined effects of ice sheets and precession on MIS-13 climate." In: *Climate of the Past* 5.2, pp. 229–243.
- Yin, Qiuzhen, André Berger, E Driesschaert, Hugues Goosse, Marie-France Loutre, and Michel Crucifix (2008). "The Eurasian ice sheet

- reinforces the East Asian summer monsoon during the interglacial 500 000 years ago." In: *Climate of the Past* 4.2, pp. 79–90.
- Yukimoto, Seiji et al. (2012). "A new global climate model of the Meteorological Research Institute: MRI-CGCM3—model description and basic performance—." In: *Journal of the Meteorological Society of Japan. Ser. II* 90A, pp. 23–64. DOI: [10.2151/jmsj.2012-A02](https://doi.org/10.2151/jmsj.2012-A02).
- Zhang, X., G. Lohmann, G. Knorr, and X. Xu (2013). "Different ocean states and transient characteristics in Last Glacial Maximum simulations and implications for deglaciation." In: *Climate of the Past* 9.5, pp. 2319–2333. DOI: [10.5194/cp-9-2319-2013](https://doi.org/10.5194/cp-9-2319-2013). URL: <https://www.clim-past.net/9/2319/2013/>.
- Zhang, Xiao, Matthias Prange, Ute Merkel, and Michael Schulz (2014a). "Instability of the Atlantic overturning circulation during Marine Isotope Stage 3." In: *Geophysical Research Letters* 41.12, pp. 4285–4293.
- Zhang, Xu, Gerrit Lohmann, Gregor Knorr, and Conor Purcell (2014b). "Abrupt glacial climate shifts controlled by ice sheet changes." In: *Nature* 512.7514, p. 290.
- Zheng, Weipeng and Yongqiang Yu (2013). "Paleoclimate simulations of the mid-Holocene and Last Glacial Maximum by FGOALS." In: *Advances in Atmospheric Sciences* 30.3, pp. 684–698.
- Ziemen, F. A., M.-L. Kapsch, M. Klockmann, and U. Mikolajewicz (2019). "Heinrich events show two-stage climate response in transient glacial simulations." In: *Climate of the Past* 15.1, pp. 153–168. DOI: [10.5194/cp-15-153-2019](https://doi.org/10.5194/cp-15-153-2019). URL: <https://www.clim-past.net/15/153/2019/>.
- Zweck, Chris and Philippe Huybrechts (2005). "Modeling of the Northern Hemisphere ice sheets during the last glacial cycle and glaciological sensitivity." In: *Journal of Geophysical Research: Atmospheres* 110.D7. DOI: [10.1029/2004JD005489](https://doi.org/10.1029/2004JD005489). eprint: <https://agupubs.onlinelibrary.wiley.com/doi/pdf/10.1029/2004JD005489>. URL: <https://agupubs.onlinelibrary.wiley.com/doi/abs/10.1029/2004JD005489>.

